TIME-TEMPERATURE HISTORIES OF BITUMINOUS COAL PARTICLES IN A DROP-TUBE REACTOR

Jonathan P. Mathews, Patrick G. Hatcher, Semih Eser, Peter M. Walsh#, and Alan W. Scaroni
Fuel Science Program and Energy Institute, 211 CUL, The Pennsylvania State University, University Park, PA 16802
#Sandia National Laboratory, PO Box 969, Livermore, CA 94551

Keywords: drop-tube, particle size and shape.

Abstract
A device often used to simulate pulverized coal combustion conditions is the drop-tube reactor. It can adequately simulate residence times, heating rates, temperatures and flow conditions. Nevertheless, derived Arrhenius pre-exponential factors for devolatilization studies can span several orders of magnitude (1), probable due to difficulties in repeating time-temperature histories for different coals (2). CFD modeling of a simple drop-tube reactor incorporating coal particles as a second phase permitted time-temperature histories to be obtained for narrow size cuts for two bituminous vitrinites. Despite a narrow particle size distribution and the rank of the vitrinites being the same, significant differences were obtained in the time-temperature histories, among the size cut and between the vitrinite samples. Furthermore, the common and simplifying assumption of spherical particles for coal was found to underestimate the characteristic heating time by 22%, in comparison to the more reasonable "house brick" particle shape obtained from microscopic observations with video capture and computational analysis.

EXPERIMENTAL

The vitrain samples were collected from *Sigillaria* (a type of Lycopod) tree remains in the roofs of coal mines in the Upper Freeport (UF) and Lewiston-Stockton (LS) coal seams. The samples were first crushed in an adjustable plate mill to reduce the topsize to approximately 2mm, then comminuted in a Holmes 501XLS pulverizer. Particle size separation was achieved by wet sieving. For shape analysis, polished pellets were prepared using a modified ASTM method. Size and shape analyses were performed using a digital image analysis system (IMAGIST, PGT, Princeton, NJ), in conjunction with a Nikon Microphot-FXA microscope and a workstation. The particle size distributions were determined with a Malvern laser light scattering instrument.

The drop-tube reactor consists of a single zone furnace operated at a maximum temperature of 1,400 °C, and is similar to previously described units (3). The reactor core is a high-purity alumina refractory tube, positioned vertically. The preheater temperature was 830 °C, and secondary nitrogen entered the top of the preheater from two inlets. The injector is water-cooled and also has a ceramic sheath for additional thermal protection. Coal is fed by an Acrison GMC-60 feeder at a rate of 0.33 g/min and is assumed to be entrained by the primary nitrogen. The tip of the injector is positioned level with the bottom of a mullite flow-straightener. Secondary nitrogen exited the flow-straightener with the primary nitrogen. The particle residence times are determined by the particle size, shape and the temperature and fluid-flow through the reactor

Fluent™, a commercially available computational fluid dynamics (CFD) code, was used to model the gas and particulate flows within the furnace. The drop-tube was modeled in one dimension using symmetry around the centerline axis with a non-uniform grid consisting of 300 cells in length and 22 cells in radius. This grid covers the tip of the injector to the outlet of the ceramic reactor. The wall of the computational grid was arbitrarily split into eight sections and the temperature was assigned based on the average value (for that wall section) obtained experimentally using a suction pyrometer. The temperature of the wall was initially set to 50 °C above the average gas temperature for that section, this value being obtained from the difference between the reactor temperature (from the internal reactor thermocouple) and the gas temperature in the center of the hot zone of the reactor. Refinements were made to the wall temperatures until good agreement < 50 °C was obtained between the CFD and experimentally-determined temperature profile.

RESULTS

Particles were introduced into the CFD calculation as a second phase assuming perfectly spherical particles with densities of 1.4 g/cm^3. Five particles were used to span the radius of the injector. The particles fall faster than the fluid; and hence are influenced by the particle diameter (mass is proportional to the radius^3, but drag is proportional to the radius^2), and changes in mass, volume and shape (which influences drag). A very narrow size cut of vitrinite (as measured by laser light scattering) was achieved by wet sieving. The difference between the $D[_v,0.1]$ and the $D[_v,0.9]$ (the volumetric weighted particle diameters such that 10 % and 90 % of the volume of the particles is in particles of greater diameters, respectively) was 66 and 53 μm for the Upper Freeport and Lewiston-Stockton vitrinites, respectively. The mean volumetric weighted particle diameters for the 200x400 US Standard Sieve cuts were 65 and 61 μm, for the Upper Freeport and Lewiston-Stockton vitrinites, respectively. Thus, a narrow distribution of time-temperature histories should be obtained for the vitrinites. However, this was not the case. The particle temperatures and residence times for the two extreme cases; the largest particle falling close to the centerline (particle 1) and the smallest particle falling closer to the wall (particle 5), are shown in Table 1. Cold flow experiments and initial CFD modeling indicated that the coal particles would fall in a narrow stream. Some radial growth in the coal stream occurs due to the expansion of the cold primary

nitrogen. However, under rapid-heating conditions, the coal particles fell as a cloud, presumably because of the "jet release" phenomenon (4) altering the particle trajectory. To better represent the particle trajectories a slight axial velocity was imposed on the particles. Particle 5 temperatures are higher at all sampling locations due to the closer proximity of the hot reactor wall (higher local gas temperature). At the 33 cm sampling location (distance from the injector) all the particles are close to the hot zone temperature (wall temperature of 1,400 °C), however, there are significant temperature differences between particles 1 and 5 at distances closer to the injector. The maximum observed difference in temperature between particles 1 and 5 is 320 K at the 23 cm sampling location for the UF case. These differences are, however, the extreme cases; visual observation indicated that the majority of the particles fell closer to the centerline than to the outer radius of the reactor. However, it is plausible that some of the collected particles can have quite different time-temperature histories despite the initially narrow particle size distribution and a drop-tube configuration designed for uniform time-temperature histories. Changes in particle size, mass and shape also influence the drag on the particle and hence the time-temperature history. The reactor temperature profile and morphological changes occurring to the LS 200x400 cut are shown in Figure 1. Significant swelling occurs for both vitrinites (2.5 and 1.8 times the mean particle diameters for the UF and LS vitrinites, respectively). This difference in swelling and a slight difference in mass loss resulted in slightly different time-temperature histories for the two vitrinites (Table 1).

Heat transfer and particle fluid-flow calculations often assume spherical particles. This is a reasonable assumption for both cases at the 33 cm location where the particles are almost exclusively cenospheric, but is a poor assumption for the initial vitrinite sample and the subsequent chars until the 23 cm sampling location (Figure 1). The silhouette of particles from the UF 200x400 cut is shown in Figure 2. Clearly there was a range of particle shapes; however, a sphere was not a good general shape representation. From >500 particle measurements the average aspect ratios are 1.7 for both vitrinite 200x400 cuts. This indicates that for a rectangular silhouette, the breadth is the length divided by 1.7. From SEM micrographs it was determined that to a first approximation, the depth could be assumed to be equal to the breadth. Thus, a square ended rectangular brick of length a and width and breadth of $a/1.7$ is a superior general shape descriptor than a sphere for these bituminous rank vitrinites. This shape descriptor has implications for both the particle residence time and the particle temperature. With a rectangular brick shape, the particle velocity is influenced by the particle orientation in the fluid. In comparison to a sphere of the same volume, the particle falling in the equilibrium position (oriented largest face down) has a similar coefficient of drag to that of a sphere (determined from terminal velocity measurements in an oil of known viscosity using square-ended bricks and spherical playdoe particles of the same mass). In contrast, the end-on orientation has a lower coefficient of drag and hence falls at a higher terminal velocity.

The non-spherical shape of coal particles has implications for commonly employed heating models. Deviation from spherical particles is reported to be responsible for the underestimation of radiative heating rate models (for 106-125 μm particles) by as much as 50% (5). In contrast, spherical carbon particles give a reasonable correlation between observed (optical pyrometry) and calculated heating rates . Combined convective and radiative models were also found to underestimate the heating rate for the same particles. Although there are uncertainties in many of the coal-related parameters and the effects of particle dispersion within the reactor in these calculations, the shape factors may also contribute significantly to the difference. Assuming that a vitrinite particle is adequately represented by a square ended rectangular brick, then equating the diameter of a sphere (d_p), of the same volume as the brick, to the length (a) yields equation 1.

$$Vol = \frac{a^3}{1.7^2} = \pi\frac{d_p^3}{6} \qquad \text{or} \qquad d_p = 0.87a \tag{1}$$

Sphericity (ϕ_s), the ratio of the surface area of a sphere to the surface area of the particle (of the same volume), yields equation 2, and substituting for d_p in equation 2 yields ϕ_s=0.78. Incorporating this term in the commonly employed convective heating calculation yields equation 3, where Nu is the Nusselt number, λ is the thermal conductivity of the gas and T_g and T_p are the temperature of the gas and particle, respectively.

$$\phi_s = \frac{\pi d_p^2}{\left(\frac{2}{1.7^2} + \frac{4}{1.7}\right)a^2} \tag{2} \qquad \frac{dQ}{dt} = \frac{Nu\lambda}{d_p}(T_g - T_p)\pi\frac{d_p^2}{\phi_s} \tag{3}$$

The sphericity term is in essence a corrective term for non-spherical particles. Incorporation of the energy gradient terms in equation 4 yields equation 5, where C_p is the specific heat of the particle, and ρ_p is the particle density.

$$\frac{\pi d_p^3}{6}\rho_p C_p \frac{dT_p}{dt} = \frac{Nu\lambda}{d_p}(T_g - T_p)\pi\frac{d_p^2}{\phi_s} \tag{4}$$

Rearranging equation 4 yields equation 5 and defining the characteristic heating time as τ yields equation 6.

$$\frac{dT_p}{dt} = \frac{6Nu\lambda}{d_p^2\phi_s\rho_p C_p}(T_g - T_p) \qquad (5) \qquad\qquad \tau = \frac{d_p^2\phi_s\rho_p C_p}{6Nu\lambda} \qquad (6)$$

As ϕ_s=0.78 and assuming Nu=2, the τ for the rectangular block is 22% greater than for the sphere. The Nu=2 assumption is valid for spheres in quiescent gas. A more accurate comparison would incorporate the influence of the square ended rectangular block geometry on the Nusselt number. Constant sphericity values of 0.73 for pulverized coal dusts and have been reported (6-7) based on microscopic and sieve analyses. A sphericity of 0.38 is also reported for fusain fibers (6), unfortunately the coal classification was not reported. A consistent shape factor (using surface areas as determined by liquid permeability and sieve sizes) has also been reported for various size cuts (11 fractions between 16 to 325 US mesh), although particle shape was found to be rank dependent (9). Aspect ratios of 1.39 to 1.55 have been determined for Pittsburgh seam coal dusts (less than 75 μm diameter) generated within the mine and by a variety of pulverizers (10). The sphericity factor reported here is consistent with some of the early work on coals (9).

CONCLUSIONS

Significant variations were found in time-temperature histories between two narrow cuts of bituminous vitrinites in a drop-tube reactor. This was partially due to the influence of volatiles release, which alters the particle trajectory, but also to differences in mass loss and degree of swelling. The single particle shape descriptor of a sphere was significantly improved upon by using a square-ended rectangular brick. This shape can account for a 22% decrease in the characteristic heating time. The shape influences the drag and hence the particle residence-time.

REFERENCES

1. Smith, I. W., Nineteenth Symposium (Int) on Combustion, The Combustion Institute, Haifa, Israel, 1982, 1045.
2. Flaxman, R. J., and Hallett, L. H., *Fuel*, 1987, **66**, (5), 607.
3. Artos, V., and Scaroni, A. W., *Fuel*, 1993, **72**, (7), 927.
4. Grey, V. R., *Fuel*, 1988, **67**, (9), 1298.
5. Maloney, D. J., Monazam, E. R., Woodruff, S. D. and Lawson, L. O., *Combustion and Flame*, 1991, **84**, (1), 210.
6. Sakiadis, B. C., Fluid and Particle Mechanics, in Perry's Chemical Engineer's Handbook, Perry, R. G. and Green, D., 1984, McGraw, New York, Chapter 5.
7. Carman, P. C., *Trans. Inst. Chem. Eng. (London)*, 1937, **15**, 150.
8. Heywood, H., *I. Mech E.*, 1933, **125**, 383.
9. Austin, L. G., Gardner, R. P., and Walker, P. L., *Fuel*, 1963, **42**, (2), 319.
10. Li, J., Size shape and chemical characteristics of mining generated and laboratory-generated coal dusts, 1990, MS Thesis, The Pennsylvania State University.

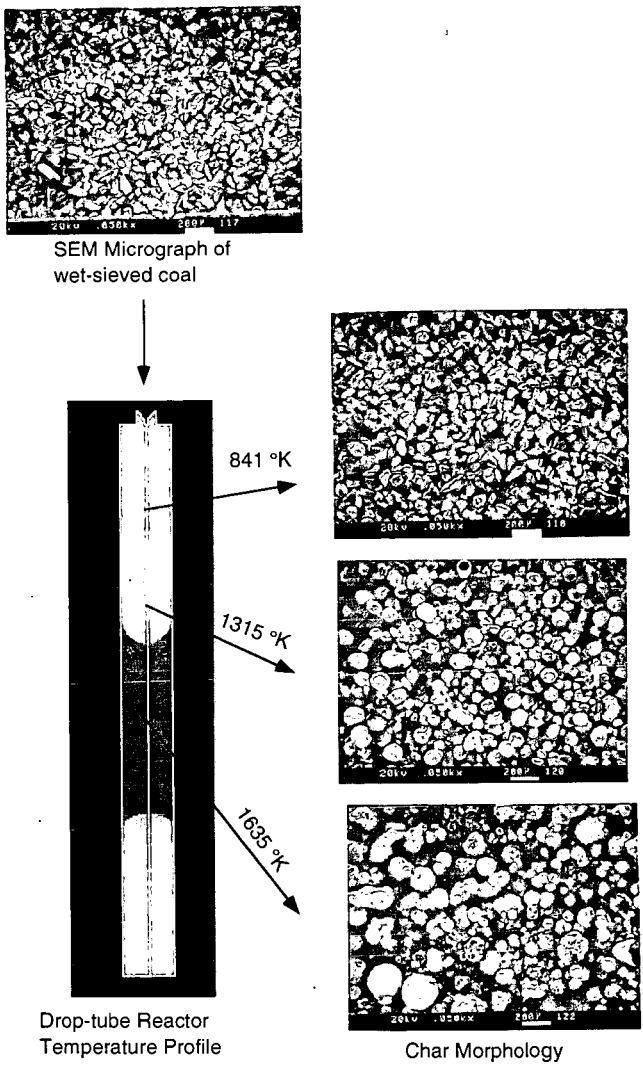

Figure 1. Fluid Temperature Profile and Char Morphology Changes for the Lewiston-Stockton Vitrinite

Table 1. Particle Residence Times and Temperatures at Various Sampling Locations

Distance from the injector / cm	Time / s			
	Particle 1(UF)	Particle 5(UF)	Particle 1(LS)	Particle 5(LS)
13	0.062	0.140	0.068	0.152
23	0.146	0.333	0.174	0.332
33	0.242	0.462	0.281	0.471
	Temperature / K			
13	645	938	726	956
23	1090	1410	1230	1400
33	1600	1640	1630	1640

Table 2. Numbered Particle Silhouette Data

No.	Diam	Circ	E/R	A/R
1	27.3	3.21	0.37	2.70
2	102.8	2.87	0.43	2.33
3	61.9	1.74	0.77	1.30
4	58.0	7.83	0.19	5.26
5	105.2	1.83	0.62	1.61
6	61.8	1.78	0.85	1.18
7	70.6	1.52	0.90	1.11
8	69.3	1.74	0.64	1.56
9	91.3	4.90	0.28	3.57
10	57.5	2.08	0.65	1.54
11	85.5	2.94	0.50	2.00
12	89.5	2.11	0.55	1.82
13	16.1	2.83	0.43	2.33
14	87.0	1.42	0.82	1.22
15	56.8	2.07	0.64	1.56

Diam is the particle diameter in μm, Circ is the circularity, E/R the elongation ratio, A/R the aspect ratio.

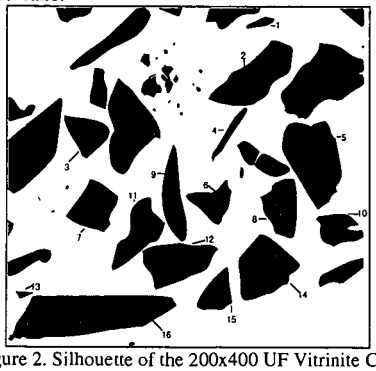

Figure 2. Silhouette of the 200x400 UF Vitrinite Cut

ALTERNATIVE SOLUTION BY ORTHOGONAL COLLOCATION IN THE REGENERATION SYSTEM

L. M. F. LONA BATISTA and R. MACIEL FILHO
Univer. Estadual de Campinas - Fac. Eng. Química - Dep. Processos Químicos .
Campinas, SP, Brazil, CEP 13081-970 - CX postal 6066, email: liliane@feq.unicamp.br

KEYWORDS: Orthogonal Collocation, Regeneration System, Modelling and Simulation

1. INTRODUCTION

Orthogonal collocation (OC) methods have been used in many chemical engineering problems such as calculation of effectiveness factors, packed bed analyses and fluid flow problems. In Finlayson (1971), the equations governing a packed bed reactor with radial temperature and concentration gradients are solved using the OC method. The method is shown to be faster and more accurate than finite difference calculations.

In this work, an industrial catalytic cracking regeneration system was simulated. The model equations form a system of non linear integro differential equations. In Maciel Filho *et al.* (1996), the Runge Kutta (RK) method and Trapezoidal Rule are used to solve the model equations, but in this present work, OC method is adopted. Generally, integrals calculation by quadrature is not made simultaneously with differential and algebraic equation, but in this work, this is the case. So, a new methodology is proposed to solve the integrals, based on an approximation of quadrature formula. The simulation results obtained through OC and RK are compared with industrial data from Petrobrás (Brazilian Oil Company).

2. PROCESS DESCRIPTION

The diagram for the catalytic cracking industrial unit is depicted in Figure 1. Deactivated catalyst flows from catalytic cracking reactor (CCR) into regeneration system, composed by fluidized bed reactor (FBR) followed by riser (R) and freeboard (FR). The fluidized bed consists on jet and bubble bed zones. The jet region is idealised as a fully mixed zone, as can be seen in Maciel *et al.* (1996). In the riser exit, the solid flow is divided in such way that part of particle goes to freeboard and part returns to tank A, with solids collected by cyclones. A certain amount of catalyst present in vase A returns to bubble bed, and the rest is transported to the cracking reactor.

3. ORTHOGONAL COLLOCATION ON REGENERATION SYSTEM SIMULATION

First, the riser and freeboard are simulated, and latter, the fluidized bed reactor. In this last reactor, the bed is splited into jet and bubbling phase (Maciel Filho *et al.*, 1996). It was assumed C, H and CO combustion. Details about kinetic parameters can be seen in Maciel *et al* (1996).

3.1 Orthogonal Collocation on Riser and Freeboard

It is assumed PFR heterogeneous model to simulate these both reactors. The model equations form a system of ordinary differential equations, which can be seen in Maciel Filho and Lona Batista (1995). When OC method is adopted, a discretized equation system is generated. The material balances are formulated for solid compounds (Carbon and Hydrogen), as well as for the four gaseous compounds i (O_2, CO, CO_2, H_2O). Thus, the following equations can be written:

gas compound i :
$$\sum_{p}^{N+2} A_{jp} C_{R_{i,p}} = \frac{\sum_{m} K'_{het_m}(x_j)\times(1-E_j)+\sum_{l} K'_{bom_l}(x_j)\times E_j}{U_{g_j}}$$

carbon balance:
$$\sum_{p}^{N+2} A_{jp} Cc_p = \frac{K'_{car,het}(x_j)\times PM_{car}\times(1-E_j)\times A_R}{Q_{s_j}}$$

hydrogen balance:
$$\sum_{p}^{N+2} A_{jp} Ch_p = \frac{K'_{hid,het}(x_j)\times PM_{hid}\times(1-E_j)A_R}{Q_{s_j}}$$

solid phase thermal balance:
$$\rho_s Cp_s v_s \left(\sum_{p}^{N+2} A_{jp} T_{s_p}\right) = \sum_{m} K'_{het_m}(x_j)\times(-\Delta H_{R,m})_j - ha_v(T_{s_j} - T_{g_j})$$

gas phase thermal balance:
$$\frac{Q_g Cp_g}{A}\left(\sum_{p}^{N+2} A_{jp} T_{g_p}\right) = ha_v(T_{s_p} - T_{g_p})fs + K'_{bom_l}(x_j)\times(-\Delta H_{R,l})_j$$

Figure 2 shows O_2 profiles along the riser, when RK and OC with 4 internal collocation points (ICP) are considered. It can be noticed an agreement in results. This behaviour is also observed in the freeboard (not shown).

3.2 Comparison between the Broyden and Newton

The algebraic equation system presented is solved using 2 different procedures. Initially, the Newton method is used to linearize the equations, that are solved by LU decomposition method, latter, the Broyden method is also adopted.

Figure 3 depicts gas temperature profile along riser length. For the OC method, it is assumed 1 and 2 ICP. Newton and Broyden methods are used to solve algebraic equations when 1 ICP is adopted. It can be concluded that Broyden and Newton method present similar accuracy, but the first one is more efficient. When it is assumed error lower than 10^{-8}, the convergence is achieved after 15 iterations to the Newton method and after 5 iterations to the Broyden method. So, Broyden method will be adopted in this work.

3.3. Orthogonal Collocation on the Fully Mixed Zone

The system of equations that models the fully mixed zone in the fluidized bed can be seen in Maciel *et al.* (1996). When OC is applied, the differential equations are discretized, and the algebraic equations remain unchanged.

gas compound i: $$\frac{F_t R}{P}(T_0 C_{0,i} - T_{FMZ} C_{FMZ,i}) = \sum_k K_{FMZ_k}$$

carbon balance: $$V_s(Cc_0 - Cc_{FMZ,j}) = K_{car,FMZ}(x_j) PM_{car}$$

hydrogen balance: $$V_s(Ch_0 - Ch_{FMZ,j}) = K_{hid,FMZ}(x_j) PM_{hid}$$

solid phase energy balance: $$\rho_s Cp_s v_s (\sum_p^{N+2} A_{jp} T_{s_p}) = \sum_m K^0_{het_m}(x_j) \times (\Delta H_{R,m})_j - h(T_{s_j} - T_{g_j}) a_v$$

gas phase energy balance: $$\frac{Q_g Cp_g}{A}(\sum_p^{N+2} A_{jp} T_{g_p}) = ha_v(T_{s_j} - T_{g_j}) fs + K^1_{hom_m}(x_j) \times (-\Delta H_{R,l})_j$$

The generated profiles from RK and OC method are divergent (Figure 4). As greater is the number of collocation point, more accurate are the results, but the same results are obtained when 4 or 5 points are used. This means that 4 points are enough.

The divergence between RK and OC method occurs due to the presence of algebraic equations. In the methodology presented in Maciel Filho and Lona Batista (1995) to solve the system of equation through RK method, the inlet condition for the second integration step represents the exit condition for the first one. Algebraic equations idealise perfectly mixed behaviour, and differential equations represent plug flow. When RK method is applied, the algebraic equations are solved in a sequential way, so it is assumed several CSTRs, and consequently a PFR behaviour. On the other hand, when OC is used, the model equations are solved simultaneously for all collocation points, so the algebraic equations always represent perfectly mixed behaviour. The inlet concentration or temperature are always assumed in x = 0. In Figure 5, the jet region is splited of into 2, 4 and 40 sections, and each of them is solved through OC method. This approach tries imitate the methodology applied in the RK method. As greater is the number of sections, closer are the profiles obtained via RK and OC. When there is division on jet phase, Cco represents the carbon concentration in the exit of previous section, similarly to the RK methodology.

3.4. Orthogonal Collocation in the Bubbling Bed

The equation system generated from heterogeneous modelling of bubbling bed can be seen in Maciel et al. (1996). When OC method is adopted the equation system become:

Gas compound i, emulsion phase

$$\sum_k K_{E_k}(x_j) = \frac{F_E R}{P}(T_{FMZ} C_{FMZ,i} - T_{D_j} C_{E,i_j}) + \frac{F_B K_{be} R T_{D_j}}{U_B P}(\sum_j^{N+2} w_j C_{B,i_j} - \sum_j^{N+2} w_j C_{E,i_j}) \qquad (1)$$

Gas compound i, bubbling bed: $$\sum_{p=1}^{N+2} A_{jp} C_{B,i_p} = -\frac{K_{be}}{U_B}(C_{B,i_j} - C_{E,i_j}) + \frac{\sum_k K'_{B_k}(x_j)}{U_B}$$

Carbon balance: $$V_s(Cc_{FMZ} - Cc_{E_j}) = K_{car,E}(x_j) PM_{car}$$

Hydrogen balance: $$V_s(Ch_{FMZ} - Ch_{E_j}) = K_{hid,E}(x_j) PM_{hid}$$

Solid phase Thermal balance: $$\rho_s Cp_s v_s (\sum_p^{N+2} A_{jp} T_{s_p}) = \sum_m K^0_{het_m}(x_j) \times (\Delta H_{R,m})_j - h(T_{s_j} - T_{g_j}) a_v$$

Gas Phase Thermal balance: $$\frac{Q_g Cp_g}{A}(\sum_p^{N+2} A_{jp} T_{g_p}) = ha_v(T_{s_j} - T_{g_j}) fs + K^1_{hom_m}(x_j) \times (-\Delta H_{R,l})_j$$

Eq. (1) in its original form is: $$\sum_k K_{E_k} = \frac{F_E R}{P}(T_{FMZ} C_{FMZ,i} - T_D C_{E,i}) + \frac{F_B K_{be} R T_D}{U_B P} \int_{h_j}^{H} (C_{B,i} - C_{E,i}) dx$$

The integral limits h_j and H must be normalised between 0 and 1 before applying quadrature formula. Initially, it was assumed that fluidized bed length is 1 m. By simplicity, it was considered

initially only one ICP. So, concentration and temperature must be calculated on x = 0.5m and x = 1 m (the inlet conditions are known).

When equations are solved at x = 0.5 m, the integral in the emulsion phase balance have limits 0 and 0.5. By quadrature formula it can be written: $\int_0^1 W(x)y(x)dx = \sum_{i=1}^{N} y_i w_i$

After changing integral limits from 0 - 0.5 to 0 - 1, another problem is found. When the calculations are made in the bed centre, it is necessary to know the concentration in bubble and emulsion phase at point x = 0.25, in order to solve the integrals by quadrature. Meanwhile, these concentrations are unknown.

So, in this work, it is developed an approach to resolve this problem. For that, it is considered that the integral of a function between 0 and r is equal to the product between r (root of Jacobi polynomial) and integral of function over limits 0 and 1. So, if it is considered W(x) = 1, we have: $\int_0^r y(x)dx = r\int_0^1 y(x)dx$ (2)

As smaller is the variation of function with the co-ordinate (x), more real is this approach. For constant functions this is really true.

It can be noticed that RK and OC method promote similar results along 1 m of bed (not shown). Figure 6 shows that carbon monoxide concentration profiles from RK and OC method are different when the simulation is made considering all length of fluidized bed. The approach expressed in equation (2), in this case, is less accurate because the bed is longer.

The bubbling bed simulation was made assuming that the bed is composed of sections of 1 m each. The results are shown in Figure 7. It can be noticed that the profiles obtained from RK and OC are more similar (this behaviour was also observed when the jet region was sectioned).

In this work, it is also proposed a second approach to calculate the integral in the internal collocation points based on the quadrature formula. It can be written that:

$$\int_0^1 y(x)dx = \sum_{i=1}^{N} y_i w_i \qquad (3)$$

If it is assumed 5 collocation points, this integral can be expressed by summation of 5 terms:

$$\int_0^1 y(x)dx = w_1 y(r_1) + w_2 y(r_2) + w_3 y(r_3) + w_4 y(r_4) + w_5 y(r_5)$$

where: r_2, r_3, r_4 are roots in the internal collocation points, $r_1 = 0$ and $r_5 = 1$.

In this second approach, it is assumed that integral between 0 and r_p may be approximate by:

$$\int_0^{r_p} y(x)dx = \sum_{i=1}^{p} y_i w_i \qquad (4)$$ where: p = collocation point and r_p = root in point p

Expression (4) is true for $r_p = 0$ and $r_p = 1$, and it represents an approximation for ICP. Table 1 shows the equation (4) applied in the integral calculation for the function f(x) = 5x (function arbitrarily chosen). It is obtained better results when r_p is close to 1.

Figure 8 shows the results using this second approach. The concentration profiles in the emulsion phase become oscillatory. This oscillation is due to inaccuracy in equation (4), mainly when integrals are calculated near root 0. So, in bubbling bed simulation it was used the first approach (equation 2), and the bed was divided in sections of 1 m each.

4. MODELLING APPLIED TO THE INDUSTRIAL SYSTEM

Operation conditions and dimensions for the regeneration system are shown in Tables 2 and 3 respectively. In order to verify if equation (2) is accurate to represent the integral when the superior limit is a ICP, a test is proposed. The bubble region is divided into sections of 1 m each. In order to facilitate the calculations, it is used only one ICP for each section. Simulations using 1, 2 or 3 ICP are made, but they indicate that there are no appreciable divergence in results (not shown), so this hypothesis does not represent limitation in this test.

In this procedure, initially, the integral in x = 0.5 is calculated according to equation 2. After solution of material and energy equations, concentration and temperature are obtained in the collocation points. The interpolation is done, and concentration and temperature in x = 0.25 are obtained. With the emulsion and bubble phase gas concentration at x = 0.5 and 0.25, the integrals may be calculated in an exact way. So, the values of integrals are compared with that obtained in the last iteration. If difference between them are greater than the allowed error, the actual integral calculation is used to determine concentration and temperature profiles.

This procedure is repeated until the difference in the integral calculation between 2 consecutive iteration does not exceed the allowed error.

By using this procedure, concentration and temperature profiles are obtained. These results are compared with that obtained when only equation (2) is used to calculate the integrals in the internal collocation points. It can be noticed that the profiles are coincident (not shown). So, the approach represented by equation 2 is adequate when the model equations are calculated for an specific length of the bubble bed. Figure 9 shows the gas compounds profiles in dry base obtained

from RK and OC methods, and Figure 10 presents the solid temperature profiles. The industrial data are also shown. Through these figures it can be noticed that the second method is more adequate to simulate the industrial regeneration system.

5. CONCLUSIONS

In this work, an alternative solution methodology based on OC, was adopted to simulate an industrial catalytic cracking regeneration system.

Concentration and temperature profiles from RK and OC method present different behaviours if there exist algebraic equation in the equation system. In the OC method, algebraic equation represents a perfectly mixed behaviour. In the methodology presented by Maciel *et al.* (1996), algebraic equations represent a sequence of perfectly mixed cells, when RK is adopted.

In the bubble bed simulation, the equation system presents integrals. When the integration is made in internal collocation points (r), it is proposed an approach at which the integral between 0 and r is equal the integral between 0 and 1 multiplied by root of Jacobi polynomial. It is observed that when this approach is used, the results are the same to that obtained if integral calculation is carried out.

Comparison with industrial data shows that RK method can predict well the concentration values, meanwhile the temperatures stay subpredicted. It can be noticed that OC is adequate in simulation of regeneration system, and the results agree with industrial data from Petrobrás. The bubble region of fluidized bed was divided in sections of 1 m each during simulation. This height can be used as an adjustable parameter of model in order to solve industrial problems.

Acknowledgements – The authors thank the industrial data provided by Petrobrás.

NOTATION

A = area of the reactor, m^2, matrix elements
a_v = interfacial area gas-solid, 1/m
C = gas molar concentration, kmol / m^3
Cc = carbon concentration, kg carb/kg catal
Ch = hydrogen concentration, kg hyd / kg cat
Cp = specific heat, kJ / kg K
E = porosity of the bed
fs = volumetric fraction of solid
H, h_j = bed height, jet height (m)
h = heat transfer coefficient kJ/K s m^2
k_{be} = buble-emulsion mass transfer coefficient
K = reaction rate group, kmol / s
K' = reaction rate group, kmol / s m^3_p
K'' = reaction rate group, kmol / m_p^3 s
P, PM = pressure, atm; molecular weight
Q = mass flow rate, kg / s
R = ideal gas constant
T = temperature, K
U = superficial velocity, m / s
ΔH = reaction heat, kJ / kmol
ρ = specific mass, kg / m^3

indices

0 = initial
B, car = bubble, carbon phase
E, D = emulsion, dense phase
FMZ, g = fully mixed zone, gas phase
het, hid, hom = heterogeneous, hydrogen, homogeneous
i, l, m = gas component, reaction *l*, *m*
R, s, t = riser, solid phase, total

REFERENCES

Finlayson, B.A., Chem. Eng. Sci., V. 26, pp. 1081-1091 (1971).

Maciel Filho R. and Lona Batista L. M. F., Modelagem Heterogênea de Regeneradores Industriais Considerando a Recirculação de Sólidos", *Anais do Iberian Latins American Conference on Computacional Methods for Engineering.* (1995)

Maciel Filho R., Lona Batista L. M. F., Mozart Fusco, *Chem. Eng. Sci.*, Vol. 51, N. 10 (1996)

TABLES AND FIGURES

Table 1: Analyses of the second approach

roots	$\int_0^r f(x)$	
	analytic results	approach (4)
$r_1 = 0$	0	0
$r_2 = 0.1127$	0.03175	0.1677
$r_3 = 0.5$	0.625	0.6438
$r_4 = 0.8873$	1.968	1.964
$r_5 = 1$	2.5	2.5

Table 2: Operation data to regeneration

Variable / case	I	II
Air flow rate (kg/s)	28.08	25.3
Catalyst flow rate (kg/s)	326.5	307.
Recirculation (kg/s)	107.8	225.
Pressure (atm)	2.88	2.65
Retificator temperature (K)	534	560
Air regeneration temperature (K)	217	202
Coke in catalyst (% weight)	0.78	0.60
H / Coke (% weight)	7.5	4.50

Table 3: Dimension of regeneration system

Section / Dimension	Length (m)	Diameter (m)
Combustor	6.71	5.18
Riser	20.09	2.74
Freeboard	8.12	7.67

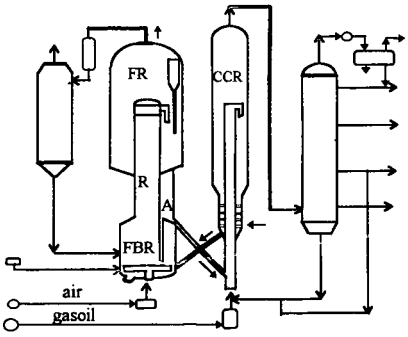

Figure 1: Diagram for a catalytic cracking industrial unit

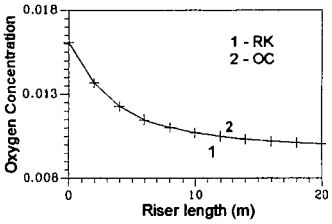

Figure 2: Oxygen Profiles

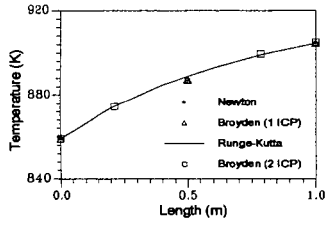

Figure 3: Gas temperature profile.

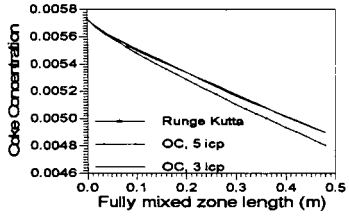

Figure 4: Carbon profiles

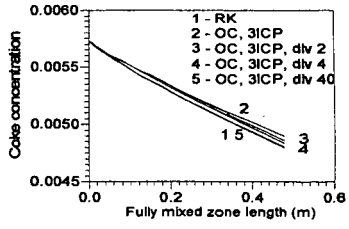

Figure 5: Carbon profiles in jets.

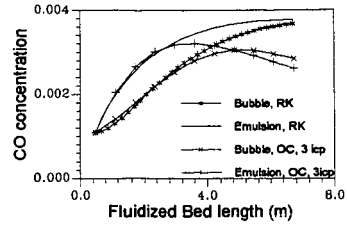

Figure 6: CO profile along bubbling bed

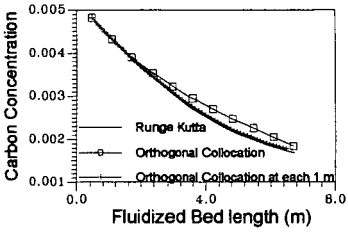

Figure 7: Carbon profile

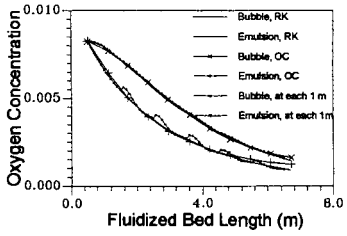

Figure 8: Oxygen profile

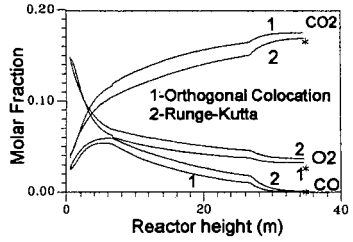

Figure 9: Gas molar fraction

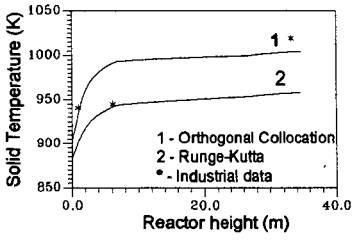

Figure 10: Solid temperature profiles

REACTOR MODELING AND PHYSICAL-CHEMICAL PROPERTIES CHARACTERIZATION IN POLYETHYLENE FLUIDIZED-BED REACTOR

Fabiano A.N. Fernandes & Liliane M.F. Lona Batista
Chemical Engineering Institute
Universidade Estadual de Campinas - UNICAMP
13081-970, Campinas - SP, BRAZIL

KEYWORDS: modeling, polyethylene, fluidized-bed reactor

INTRODUCTION

Although the fluidized-bed reactor technology for producing polyethylene has been invented on the 50s, and its commercial use has been growing since the last decade, little is still known about its behavior regarding to temperature, concentration, production and polyethylene physical-chemical properties characterization gradients inside the reactor.

In the past years, some researchers have focused their attention to the modeling of these polyethylene gas-phase processes (Choi & Ray, 1985; McAuley et al., 1994) but, even though, these models are based on strong assumptions such as a well-mixed emulsion phase, which can be easily brought down when considering low degree or no pre-polymerization. In the latter cases, heat and mass transfer resistances become significant and the polymerization rate of young particles can lead to over-heating.

In order to create a more reliable model for the fluidized-bed reactor, a steady-state model incorporating interactions between separate bubble and emulsion phases inside the reactor bed has been developed. A polymer physical-chemical characterization model has also been developed and the linkage of these two models has been studied.

MODEL DEVELOPMENT

The assumptions that have been made in the development of the model are summarized below.

- The fluidized bed comprises two phases: bubble and emulsion phases.
- The polymerization reactions occur only in the emulsion phase.
- The emulsion phase is at minimum fluidizing conditions.
- The emulsion phase is not well-mixed.
- The gas in excess of that required for maintaining the minimum fluidizing condition passes through the bed as bubble phase.
- The bubbles are spherical and of uniform size throughout the bed, reaching a maximum stable size. The bubbles travel up through the bed at a constant velocity in a plug-flow regime.
- There are a negligible radial gradient of temperature and concentration in the bed, due to the agitation produced by the up flowing gas.
- There is negligible resistance of heat and mass transfer between gas and solids in the emulsion phase.
- There is no agglomeration between polymer particles throughout the bed.
- Elutriation of fines from the bed are not considered.
- The polymer particle grows and segregates inside the reactor.
- The gas-phase is composed by ethylene, 1-butene, 1-hexene, nitrogen and hydrogen

All mass and energy balances were given in the differential form, in order to account for gas concentrations (ethylene, 1-butene, 1-hexene, hydrogen and nitrogen) and temperature axial gradients along the reactor in both phases. This means that the reagent gases are in a plug-flow regime but at different velocities for bubble and emulsion phases.

Bubble-phase material and energy balances

$$\frac{dC_{bi}}{dz} = \frac{K_{mi}}{U_b}.\left(C_{ei} - C_{bi}\right)$$

$$\frac{dT_b}{dz} = \frac{H_m}{U_b.C_{bT}.\dot{c}_{pgT}}.\left(T_b - T_e\right)$$

Emulsion-phase material and energy balances

$$\frac{dC_{ei}}{dz} = \frac{Rp'.\left(1-\varepsilon_{mf}\right)}{\varepsilon_{mf}.A.U_e} + \frac{K_{mi}.\left(C_{bi}-C_{ei}\right).\delta}{\left(1-\delta\right).\varepsilon_{mf}.U_e}$$

$$\frac{dT_e}{dz} = \frac{\left[\sum_{i=1}^{NC} c_{pgi}^{\bullet}.K_{mi}.\left(C_{bi}-C_{ei}\right)+Hm\right].\left(T_b-T_e\right).\delta}{U_e.\left(1-\delta\right).\varepsilon_{mf}.c_{pgT}^{\bullet}.C_{eT}} -$$

$$\frac{Rp'.\left(1-\varepsilon_{mf}\right).M_W.\left[-\Delta H-\left(c_{ps}-c_{pgT}\right).\left(T_e-T_{ref}\right)\right]+\pi.D.U_h.\left(T_e-T_\infty\right)}{U_e.\varepsilon_{mf}.c_{pgT}^{\bullet}.C_{eT}}$$

The new approach given by this study relies on the average weight fraction of catalyst in the polymer, which is not constant along the reactor and has been equated also in a differential form depending mainly on the polyethylene production. In this way it is possible to simulate that there is a high catalyst/polymer mass weight fraction at the top of the reactor and a low mass weight fraction at the base, what is in accordance with the fact that there exists a degree of segregation of the different polyethylene particle sizes in the fluidized-bed reactor.

Average mass weight fraction of catalyst in the polyethylene

$$\frac{d\chi}{dz} = \frac{Rp'.A.\left(1-\delta\right).\left(1-\varepsilon_{mf}\right).M_W}{\chi.q_{cat}}$$

The great advantage in having this new variable is that it allows the usage of a more complex reaction mechanism, which is summarized in Table 1. Not only that but it gives strong support to predict the growth of polyethylene particles along the fluidized-bed.

It is important to state that the mathematical resolution of the model followed the physical design of the reactor, where the gas and polymer particles flow in countercurrent, the gas is fed at the base and the catalyst at the top portion of the reactor. This design configuration implies on having contour conditions at the base and top of the reactor, what resulted in an iterative resolution of the system till all base and top contour conditions were satisfied. The final reactor model was composed of 10 differential equations, plus accessories equations for the calculation of the particle growth throughout the reactor.

The reaction mechanism used in this work is the same described by Kissin (1987), de Carvalho et al (1989) and McAuley et al (1990). In general, this mechanism is based upon the coordination copolymerization of ethylene using Ziegler-Natta catalyst with two different types of catalyst sites. Each site type is associated with different rate constants for formation, initiation, propagation and chain transfer. Only the effects of the terminal monomers were considered on the reaction rates.

Alongside to the reactor model, the method of moments (Zabisky et al, 1992) has been used to create a new mathematical model capable of predicting the physical-chemical characteristics of the polyethylene (average molecular weight, density, polydispersity, melt index, etc.) been build up along the reactor height and also to predict the polymer particle growth. The guidelines followed by Zabisky et al (1992) were adapted to the case of the coordination copolymerization reaction mechanism outlined by McAuley et al (1990) and to the dynamics along the reactor height. The model consisted of 36 differential equations corresponding to the components material balances and the life and dead polymers moments, plus accessories equations to account for calculation of polydispersity, density, comonomer incorporation in the polymer chain and others calculated characteristics.

To connect the results from the reactor model (temperature, concentration and production profiles obtained in function of the height position) with the results from the method of moments' predictions (concentration, production and quality profiles obtained in function of the time) an iterative process was created. Outputs from the reactor model served as inputs for the physical-chemical model, and vice-versa, so that adjustments on operational parameters could be done in both models, till the profiles obtained from both models matched in terms of ethylene and comonomers concentrations and production of polyethylene. The difficulty of this operation had relied on the different integration variables (time and position) of the two models, what complicates the convergence of the system to a single matching result.

RESULTS

The data that have been obtained with the reactor model have shown interesting results concerning to the temperature and concentration gradients in the reactor, specially at the catalyst feeding region, where the reaction rate is greater due to the higher temperature and to the higher influence of the catalyst in the formation and early development of young polymer particles. The case illustrated by figure 1 shows a typical temperature and concentration gradient profiles given for the production of polyethylene in a fluidized bed reactor with no prepolymerization. The data used in the models simulations are shown in table 2.

As it can be observed from figure 1, the top portion of the reactor requires special attention in order to not present hot spots or even the melting of the polymer. According to the parametric study of the system, this situation can be avoided by controlling the gas feed velocity and temperature. In terms of polyethylene production, it can be enhanced by elevating the gas feed temperature, and by decreasing the gas feed velocity. It was observed that an increase of 15K in the gas feed temperature can multiply the production of polyethylene by up to 50% (not shown), without compromising the polyethylene characteristic and integrity.

The physical-chemical model, alone, shows that the average molecular weight of the polymer increases more intensely at the beginning of the polymerization period and slows down after a while. The polydispersity follows the same increase profile. Density and comonomer incorporation on the polymer remains practically constant during the entire polymerization process (not shown).

The figure 2 shows the simulation of the polyethylene physical-chemical characteristics build up inside the fluidized bed reactor, obtained by the link of the reactor and the physical-chemical characterization models. The simulation shows that there is a highly active reaction zone in the top of the reactor, what is in accordance to the reactor model. Beneath this highly active zone, follows a less active zone responsible for the refining of the polymer characteristics.

The upper and highly reaction active zone tends to be less evident when prepolymerization of the polyethylene particles are employed (not shown).

The assumption that the polymer particles segregates inside the reactor still holds up, with fine particles being at the reactors' top and heavier particles being distributed along the reactor height.

CONCLUSION

In this work a new reactor and physical-chemical characterization models were developed and linked together to give a complete understanding of the fluidized bed reactor for polyethylene production.

The reactor model developed permits the usage of a more complex reaction mechanism and the prediction of the polymer average particle diameter and polymer/catalyst weight fraction. But more than all, it also extents the possibility of simulation of the reactor operating with low degree or no prepolymerization, case which the models based on the well-mixed emulsion phase theory are incapable to predict correctly.

The two models when linked together become very useful tool to perform a complete optimization of the fluidized bed reactor for the production of polyethylene, since it makes possible to optimize the reactor conditions looking for an enhancement on the polyethylene production rate and at the same time check how the changes on the operational conditions of the reactor influence on the grade of polymer being produced.

From the industrial point of view, these more reliable copolymerization models are capable of simulating the synthesis conditions of the polyethylene and permit the study of new copolymers previously to industrial tests. In this way, new polymer grades can be developed more easily, and existents grades can be optimized in order to produce high quality resins.

NOTATION

A	sectional area of the reactor
C_{ij}	concentration of the component j in the i phase
c_{pgj}	molar heat capacity of the gas component j
c_{ps}	mass heat capacity of the solids

D fluidized bed reactor diameter
ΔH heat of reaction
H^* molecular hydrogen
H_m heat transfer coefficient
K_{mj} mass transfer coefficient of the component *j*
M_W ethylene molecular weight
NC number of components
P(r) non-reactive polymer with chain length size *r*
q_{cat} catalyst feeding rate
R^* potential active site
$R_i(r)$ live polymer with terminal monomer *i* and chain length size *r*
Rp' polyethylene production rate
T_i temperature of the *i* phase
T_{ref} reference temperature
U_i velocity of the *i* phase
U_h wall heat transfer coefficient
X cocatalyst
z height above the distributor
δ bubble volumetric fraction in bed
ε_{mf} minimum fluidized porosity
χ catalyst/polymer average weight fraction

subscripts
1 ethylene
2 1-butene
b bubble phase
e emulsion phase
mf minimum fluidizing condition
T total (sum of all components)

ACKNOWLEDGEMENTS

The authors would like to thanks the São Paulo State Research Aid Foundation - FAPESP, for the award of a scholarship and for the financial support of this research.

REFERENCES

Choi, K.Y. & Ray, W.H. The dynamic behaviour of fluidized bed reactors for solid catalyzed gas phase olefin polymerization. *Chem.Eng.Sci.*, **40**: 2261-2279, 1985.

deCarvalho, A.B., Gloor, P.E. & Hamielec, A.E. A Kinectic Mathematical Model for Heterogeneous Ziegler-Natta Copolymerization, *Polymer*, **30**: 280, 1989.

Kissin, Y.V. *Isospecific Polymerization of Olefins with Heterogeneous Ziegler-Natta Catalysts*, Springer-Verlag, New York, 1987.

McAuley, K.B., MacGregor, J.F. & Hamielec, A.E. A kinetic model for industrial gas-phase ethylene copolymerization. *A.I.Ch.E.J.*, **36**(6): 837-850, 1990.

McAuley, K.B., Talbot, J.P. & Harris, T.J. A comparison of two-phase and well-mixed models for fluidized-bed polyethylene reactors. *Chem.Eng.Sci.*, **49**(13): 2035-2045, 1994.

Zabisky, R.C.M.; Chan, W.M.; Gloor, P.E. & Hamielec, A.E. A kinetic model for olefin polymerization in high-pressure tubular reactors: a review and update. *Polymer*, **33**: 2243-2262, 1992.

TABLES AND FIGURES

Table 1. Reaction Mechanism and Kinetic Parameters

Reaction			Catalitic Site 1	Catalitic Site 2
formation [s^{-1}]	$R^* \xrightarrow{kf} R_0$	kf	1	1
initiation	$R_0 + C_i \xrightarrow{ki} R_i(1)$	ki_1	1	1
[$L.mol^{-1}.s^{-1}$]		ki_2	0.14	0.14
	$H^* + C_i \xrightarrow{khi} R_i(1)$	kh_1	1	1
		kh_2	0.1	0.1
	$H^* + X \xrightarrow{khr} R_X(1)$	kh_r	20	20
propagation	$R_i(r) + C_k \xrightarrow{kpik} R_k(r+1)$	kp_{11}	85	85

[L.mol^{-1}.s^{-1}]		kp_{12}	2	15
		kp_{21}	64	64
		kp_{22}	1.5	6.2
chain transfer	$R_i(r) + C_k \xrightarrow{kfmik} P(r) + R_k(l)$	kf_{11}	0.0021	0.0021
[L.mol^{-1}.s^{-1}]		kf_{12}	0.006	0.11
		kf_{21}	0.0021	0.001
		kf_{22}	0.006	0.11
	$R_i(r) + H_2 \xrightarrow{kfh_i} P(r) + H^*$	kfh_1	0.088	0.37
		kfh_2	0.088	0.37
	$R_i(r) + X \xrightarrow{kfr_i} R_X(l) + P(r)$	kfr_1	0.024	0.12
		kfr_2	0.048	0.24
	$R_i(r) \xrightarrow{kfs_i} P(r) + H^*$	kfs_1	0.0001	0.0001
		kfs_2	0.0001	0.0001
deactivation [s^{-1}]	$R_i(r) \xrightarrow{kds} P(r) + R_D$	kds	0.0001	0.0001

Table 2. Operational conditions and reactor data used in the simulations

Ethylene feed rate	0.50 mol/L	1-Butene feed rate	0.20 mol/L
Hydrogen feed rate	0.05 mol/L	Inert feed rate	0.00 mol/L
Catalyst feed rate	0.20 g/s	Cocatalyst feed rate	0.01 mol/L
Gas feed temperature	316 K	Room temperature	340 K
Catalyst density	2.38 g/cm^3	Catalyst diameter	0.05 mm
Activation energy	37620 J/mol	ΔH	-3829 J/g
Reactor diameter	396 cm	Reactor height	1097 cm
δ	0.214	ε_{mf}	0.50
U_{mf}	7.0 cm/s	U_e	34.8 cm/s
U_b	114.0 cm/s	Bubble diameter	15 cm

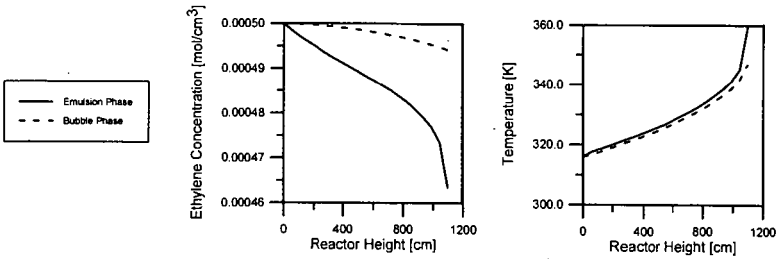

Figure 1. Ethylene concentration and temperature gradients for the production of polyethylene in a fluidized bed reactor with no prepolymerization. Simulation data from table 2.

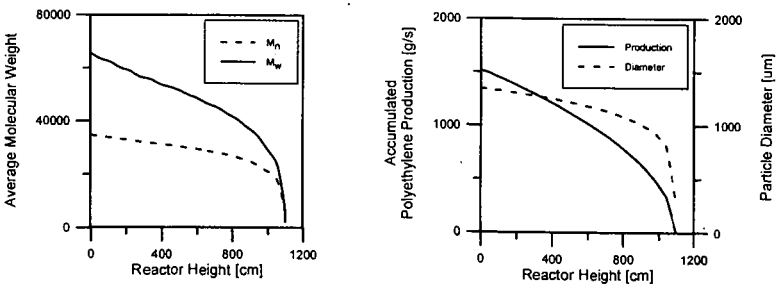

Figure 2. Average molecular weight (M_n and M_w), accumulated polyethylene production and particle diameter build up profiles inside the fluidized bed reactor. Simulation data from table 2.

MODELING OF METHYLCYCLOHEXANE TRANSFORMATION OVER A USHY ZEOLITE

Henrique S. Cerqueira, Patrick Magnoux, Dominique Martin and Michel Guisnet, Université de Poitiers, Fac. Sci. Fond. Et Appliquées, UMR CNRS 6503, 40, avenue du Recteur pineau, 86022 Poitiers Cedex, FRANCE

Key words: USHY zeolite, modeling, methylcyclohexane

ABSTRACT

A kinetic model with functions of deactivation by coke has been developed for the transformation of methylcyclohexane (isomerization, cracking, hydrogen transfer and coking) in a fixed bed reactor at 450°C over a USHY zeolite. A good fitting is obtained showing that the function of deactivation by coke depends on contact time.

INTRODUCTION

Although naphthenes are important constituents of feedstocks and products of FCC (fluid catalytic cracking) little work has been reported in the literature [1,2]. This study concerns the transformation of methylcyclohexane over an USHY zeolite in a fixed bed reactor at 450°C.

From the effect of contact time the following reaction scheme was proposed to explain the formation of various products over the fresh catalyst.

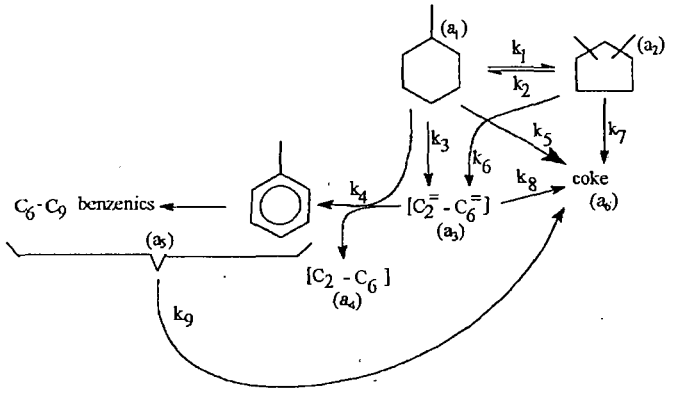

Methylcyclohexane (a_1) is isomerized into dimethylcyclopentanes (a_2). C_2-C_6 alkenes (a_3) are formed from double cracking of a_1 and a_2 followed by oligomerisation cracking steps. Methylcyclohexane is also transformed into toluene through hydrogen transfer towards a_3 with formation of C_2-C_6 alkanes (a_4), three moles of a_3 being transformed per mole of a_1. Toluene undergoes disproportionation with formation of benzene, xylenes and trimethylbenzenes. Coke results mainly from C_7 products (which are not observed) of the simple cracking of a_1 and a_2 but is also formed from a_3 and from aromatics (a_5).

A kinetic model with deactivation functions was developed allowing the complete description of the transformation of methylcyclohexane.

MATERIALS AND METHODS

The USHY zeolite ($Na_{0.4}H_{34.5}Al_{34.9}Si_{157.1}O_{384}$, 17.8 extra framework aluminium) resulted from calcination under air flow, at 500°C for 12 h of an ultrastable NH_4 zeolite (CBV 500 from PQ). Methylcyclohexane transformation was carried out in a fixed bed reactor at 450°C p/V_z = 0.9 bar, $p_{methylcyclohexane}$ = 0.1 bar at various contact times. Reaction products were analyzed on-line by gas chromatography with a 50 m fused silica capillary column Plot Al_2O_3/KCl.

The mathematical model has been previously described [3]. From the reaction scheme, assuming elementary steps, a plug flow behaviour uniform porosity and quasi-steady-state, the following equations may be written:

$$\frac{\partial a_1}{\partial Z} = \frac{P}{WHSV \cdot R \cdot T \cdot \sum_{i=1}^{5} a_i} \cdot \left[k_2 \cdot a_2 \cdot \phi_1 - \left(k_1 \cdot \phi_2 + k_3 \cdot \phi_3 + k_4 \cdot a_3 \cdot \phi_3 + k_5 \cdot \phi_{coke}\right) \cdot a_1\right] \quad (1)$$

$$\frac{\partial a_2}{\partial Z} = \frac{P}{WHSV \cdot R \cdot T \cdot \sum_{i=1}^{5} a_i} \cdot \left[k_1 \cdot a_1 \cdot \phi_2 - \left(k_6 \cdot \phi_3 + k_2 \cdot \phi_1 + k_7 \cdot \phi_{coke}\right) \cdot a_2\right] \quad (2)$$

$$\frac{\partial a_3}{\partial Z} = \frac{P}{WHSV \cdot R \cdot T \cdot \sum_{i=1}^{5} a_i} \cdot \left[\left(\nu_1 \cdot k_3 \cdot a_1 + \nu_2 \cdot k_6 \cdot a_2\right) \cdot \phi_3 - \left(3 \cdot k_4 \cdot a_1 \cdot \phi_3 + k_8 \cdot \phi_{coke}\right) \cdot a_3\right] \quad (3)$$

$$\frac{\partial a_4}{\partial Z} = \frac{P}{WHSV \cdot R \cdot T \cdot \sum_{i=1}^{5} a_i} \cdot \left(3 \cdot k_4 \cdot a_1 \cdot a_3 \cdot \phi_4\right) \quad (4)$$

$$\frac{\partial a_5}{\partial Z} = \frac{P}{WHSV \cdot R \cdot T \cdot \sum_{i=1}^{5} a_i} \cdot \left[\left(k_4 \cdot a_1 \cdot a_3 \cdot \phi_4\right) - k_9 \cdot a_5 \cdot \phi_{coke}\right] \quad (5)$$

$$\frac{\partial a_6}{\partial Z} = \frac{P}{WHSV \cdot R \cdot T \cdot \sum_{i=1}^{5} a_i} \cdot \left(\nu_3 \cdot k_5 \cdot a_1 + \nu_4 \cdot k_7 \cdot a_2 + \nu_5 \cdot k_8 \cdot a_3 + \nu_6 \cdot k_9 \cdot a_5\right) \cdot \phi_{coke} \quad (6)$$

$$\frac{\partial a_7}{\partial t} = \frac{P}{R \cdot T \cdot \sum_{i=1}^{5} a_i} \cdot \left(\nu_3 \cdot k_5 \cdot a_1 + \nu_4 \cdot k_7 \cdot a_2 + \nu_5 \cdot k_8 \cdot a_3 + \nu_6 \cdot k_9 \cdot a_5\right) \cdot \phi_{coke} \quad (7)$$

Where, a_i is the concentration of the a_i species [mols of lump i / g gas], $a_7 = C_c$ is the coke content on catalyst [wt%], k_i is the kinetic constant for the reaction I, t is the time-on-stream, Z is the dimensionless axial position, $\nu_1 = \nu_2$ is the ratio between the molecular weight of methylcyclohexane and olefins, $\nu_3 = \nu_4$ is the molecular weight of methylcyclohexane, ν_5 is the molecular weight of olefins, ν_6 is the molecular weight of aromatics, ϕ_i is the deactivation function for reactions leading to the correspondent a_i specie and ϕ_{coke} is the deactivation function for reactions leading to coke.

The mathematical solution was performed by finite difference discretization of the reactor with respect to the axial position. For a given set of kinetic constants and deactivation parameters, the system solution was obtained by backward finite differences formula with variable step, implemented in the DASSL code [4,5]. The initial condition is that the reactor is full of nitrogen. Although numerical convergence for a relative tolerance of 10-7 was obtained only for 120 discretization elements, satisfactory results are obtained for 10 discretization elements.

RESULTS AND DISCUSSION

Deactivation Functions

The deactivation functions may be related to the true deactivating agent, i.e., coke itself [6,7]. One parameter functions (eq. 8) which provide results very similar to those obtained with multiparameter functions [8] were chosen for all the reaction steps except for coke formation. However as coke may alter the product distribution, the deactivation parameter (α) should depend on the step.

It is generally found that at short time-on-stream, which corresponds to the formation of the first coke molecules, coke formation itself is not deactivated. Deactivation becomes very pronounced when the coke molecules attain a size comparable to that of zeolite cages because the access of the coke-maker molecules becomes difficult. In order to consider this particular mode of deactivation the deactivation function given in equation 9 was used for all reactions leading to coke.

The limit coke content (C_{lim}) above which the coke affects its formation was obtained form the change in coke content as a function of time-on-stream. Many values were considered for the *A* constant, a value of 180 being finally found to be appropriate.

$$\phi_i = \exp\left(-\alpha_i \cdot C_c\right) \quad (8)$$

$$\phi_{coke} = \frac{1}{\exp\left[A \cdot \left(C_c - C_{lim}\right)\right] + 1} \quad (9)$$

Parameter Estimation

Different approaches were tested to improve the convergence of a maximum likelihood method [9]. Sequential parameter estimation, centering [10], model reformulation, using only either initial or iso-coke data and also trial and error change of initial values. Experimental error estimation was made with five replicates for one time-on-stream of 30 min and a WHSV (weight hourly space velocity) of 62.

Firstly, relations between the deactivation parameters (α) were established. To achieve this goal the residual activities as a function of coke on catalyst should be determined for all the reaction steps, the initial activities (at zero coke content) being estimated by extrapolation of the curves giving the product yield vs. time-on-stream. The following relations between parameters were obtained.

$$\alpha_1 = \alpha_2 = \alpha \quad (10) \qquad \alpha_3 = 1.6 \cdot \alpha \quad (11) \qquad \alpha_4 = \alpha_5 = 1.8 \cdot \alpha \quad (12)$$

Good fitting is obtained for each contact time but the value of α seems to depend on contact time, which indicates that the location of coke, hence its deactivating effect changes with this parameter (α). Indeed when coke molecules are located near the pore mouth, their blockage effect is more significant than when they are homogeneously distributed in the crystallite [11].

The values of α which give the best results increase with contact time form 3 (WHSV = 500) to 12 (WHSV = 62), i.e. the longer the contact time, the less homogeneous the coke distribution in the zeolite crystallites. With these values of α a good agreement is found between experimental results and model curves (figs. 1 to 3). The objective likelihood function presented a relative reduction of 25%.

The kinetic constant values are presented in Table 1. For isomerization of methylcyclohexane the k_1/k_2 ratio is determined from thermodynamic data [12].

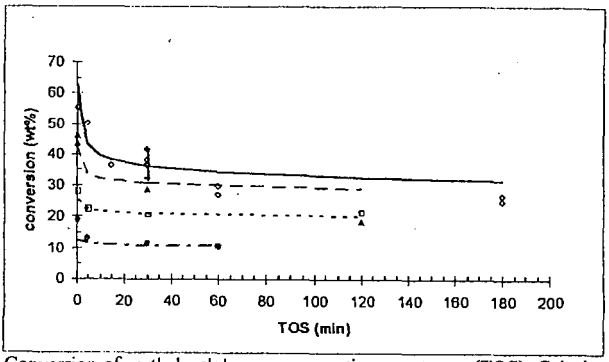

Figure 1: Conversion of methylcyclohexane versus time-on-stream (TOS). Calculated curves and experimental data for 4 different contact times.

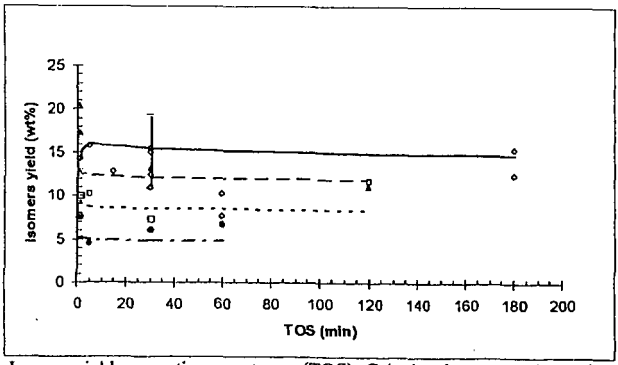

Figure 2: Isomers yield versus time-on-stream (TOS). Calculated curves and experimental data for 4 different contact times.

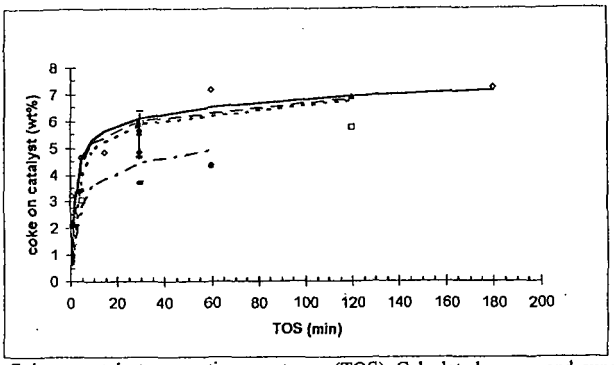

Figure 3: Coke on catalyst versus time-on-stream (TOS). Calculated curves and experimental data for 4 different contact times.

Table 1 : Kinetic constants

kinetic constant	value	kinetic constant	value
k_1 [(g cat/cm^3)$^{-1}$·h^{-1}]	8.5×10^4	k_6 [(g cat/cm^3)$^{-1}$·h^{-1}]	1.7×10^5
k_2 [(g cat/cm^3)$^{-1}$·h^{-1}]	$0.417 \cdot k_1$	k_7 [(g cat/cm^3)$^{-1}$·h^{-1}]	3.5×10^4
k_3 [(g cat/cm^3)$^{-1}$ h^{-1}]	7.0×10^4	k_8 [(g cat/cm^3)$^{-1}$·h^{-1}]	8.5×10^3
k_4 [(g cat/cm^3)$^{-1}$·(g/mol)·h^{-1}]	3.3×10^9	k_9 [(g cat/cm^3)$^{-1}$·h^{-1}]	5.7×10^3
k_5 [(g cat/cm^3)$^{-1}$·h^{-1}]	2.0×10^3		

CONCLUSIONS

The reaction scheme of methylcyclohexane transformation over a USHY zeolite was established. A kinetic model was developed to represent the change versus time-on-stream of the product yields. A good fitting is obtained showing that the function of deactivation by coke depends on contact time and then on the coke location inside the zeolite.

ACKNOWLEDGEMENTS

The support of CAPES foundation (Brazilian government), FCC S.A. and UMR CNRS 6503 is gratefully acknowledged.

REFERENCES

[1] Lin, L., Gnep, N. S. and Guisnet, M., Am. Chem. Soc. Div. Petro. Chem., Miami meeting, September 10-15, 687-693 (1989).
[2] Corma, A., Mocholi, F., Orchilles, V., Koermer, G. S. and Madon, R. J., Appl. Catalysis A: General, 67, 307-324 (1991).
[3] Cerqueira, H. S., Falabella S-Aguiar, E. and Biscaia Jr., E. C., Appl. Catalysis A: General, 164, 1-2 (1997).
[4] Petzold, L. R., "DASSL code", version 1989, Computing and Mathematics Research Division, Lawrence Livermore National Laboratory, L316, PO Box 808, Livermore, California, USA.
[5] Brenan, K. E., Campbell, S. L. and Petzold, L. R., "Numerical Solution of Initial Value Problems in Differential-Algebraic Equations", Elsevier Sc. Publishing Co., Inc., New York (1989).
[6] Froment, G. and Bischoff, K. B., Chem. Eng. Sci., 16(3) 189-201 (1961).
[7] Froment, G. and Bischoff, K. B., Chem. Eng. Sci., 17(4) 105-114 (1962).
[8] Cerqueira, H. S., Falabella S-Aguiar, E. and Biscaia Jr., E. C., Studies in Surface Science Catalysts, catalyst deactivation 1997, 303-310, Elsevier Science B.V. (1997).
[9] Pinto, J. C., "Estima code", version 1997, Chemical Engineering Program, COPPE/UFRJ, CP 68502, CEP 21945-970, Rio de Janeiro, Brazil.
[10] Watts, D. G., The Can. Journal of Chem. Eng., 74, August, 701-710 (1994).
[11] Doka Nassionou, G. A., Magnoux, P. and Guisnet, M., Microporous and Mesoporous Materials, (1998) in press.
[12] Stull, D. R., Westrun Jr., E. F. and Sinke, G. C., "The Chemical Thermodynamics of Organic Compounds", John Wiley and Sons, Inc. (1969).

INVESTIGATION OF THERMOLYSIS PATHWAYS FOR DIARYLMETHANE MODEL COMPOUNDS UNDER RESTRICTED DIFFUSION

A. C. Buchanan, III* and Phillip F. Britt

Chemical and Analytical Sciences Division
Oak Ridge National Laboratory
1 Bethel Valley Road
P. O. Box 2008
Oak Ridge, Tennessee 37831-6197

Submitted For Publication in ACS, Division of Fuel Chemistry, Preprints

* To whom correspondence should be addressed
phone: (423) 576-2168
fax: (423) 576-5235
e-mail: buchananac@ornl.gov

This research was sponsored by the Division of Chemical Sciences, Office of Basic Energy Sciences, U.S. Department of Energy, under contract No. DE-AC05-96OR22464 with Oak Ridge National Laboratory, managed by Lockheed Martin Energy Research, Corp.

INVESTIGATION OF THERMOLYSIS PATHWAYS FOR DIARYLMETHANE MODEL COMPOUNDS UNDER RESTRICTED DIFFUSION

A. C. Buchanan, III and Phillip F. Britt

Chemical & Analytical Sciences Division
Oak Ridge National Laboratory
1 Bethel Valley Road
P.O. Box 2008, MS-6197
Oak Ridge, Tennessee 37831-6197

Keywords: Model compounds, pyrolysis, restricted diffusion, diphenylmethane

ABSTRACT

Diarylmethane linkages are important structural units in coals and Kraft lignins that contain only strong carbon-carbon bonds. Studies of the thermolysis of the model compound, diphenylmethane, in fluid phases have demonstrated an important retrograde cyclization pathway that forms the polycyclic aromatic hydrocarbon, fluorene, as a major product. We have now prepared a silica-immobilized form of diphenylmethane ($\equiv SiOC_6H_4CH_2C_6H_5$; $\equiv$DPM) to investigate the influence of restricted mass transport on this retrogressive pathway. Initial studies at 425-450 °C indicate that at high surface coverages, the cyclization pathway remains the dominant thermolysis pathway. In addition, restricted diffusion leads to the production of significant quantities of triphenylmethanes (ca. 8-10 %) generated by a competing radical displacement pathway involving diphenylmethyl radicals. The impact of lower $\equiv$DPM surface coverages and the structure of neighboring spacer molecules on the retrogressive pathways is under investigation.

INTRODUCTION

The thermal decomposition of diarylmethane structures has drawn considerable attention as they are models for related linkages present in coals and Kraft lignin.[1-12] These linkages are important due to their refractory nature, which makes it difficult to cleave them except at high temperatures. For example, diphenylmethane (DPM) is typically reported to be thermally stable at 400-430 °C even in the presence of a hydrogen donor solvent such as tetralin.[8,9] Petrocelli and Klein reported that thermolysis of DPM in biphenyl solvent at 1.8-6.2 MPa (nitrogen) and 550-600 °C gave benzene, toluene, and fluorene as major products, as shown below, with fluorene yields of ca. 25-30 % and material balances of 81-85 %.[10]

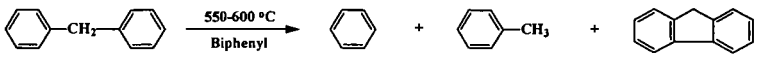

The main products are consistent with an earlier report of Sweeting and Wilshire, who examined the thermolysis of DPM at 700 °C in the vapor phase under short contact time, flow conditions.[11] However, Suzuki, et. al. have reported that thermolysis of liquid DPM in the absence of solvent, catalyst, or hydrogen atmosphere can occur slowly at temperatures as low as 425 °C to produce benzene and toluene at a rate of about 1 % h^{-1} (formation of fluorene was not reported).[12]

In our research, we have been exploring the effects of restricted mass transport on thermolysis reactions of model compounds for related structural units in fossil and renewable energy resources.[13] Restricted mass transport, which can be important in the thermochemical processing of macromolecular energy resources, has been simulated through the use of model compounds that are covalently linked to a silica surface through a thermally robust Si-O-C_{aryl} linkage. This research has uncovered examples where product selectivities and reaction rates

are significantly altered compared with corresponding fluid phase models. In particular, retrogressive rearrangement and cyclization pathways can be promoted under restricted mass transport conditions. In this paper, we report our first investigations of the thermolysis of a silica-immobilized diphenylmethane, indicated by ≈DPM, to examine the nature of the cyclization pathway under diffusional constraints.

Experimental

The DPM model compound was attached to the silica surface through both a *para*- and *meta*- linkage. The precursor phenol, *p*-$HOC_6H_4CH_2C_6H_5$, was commercially available. Purification involved elution from a silica gel column with benzene, followed by multiple recrystallizations from hot benzene:hexane (1:4) to give the desired phenol in 99.9 % purity by GC. The isomeric phenol, *m*-$HOC_6H_4CH_2C_6H_5$, was synthesized by the reaction of benzene with *m*-$HOC_6H_4CH_2OH$ in the presence of $AlCl_3$. Following addition of water and then additional benzene, the benzene layer was separated, washed with saturated NaCl solution, dried over Na_2SO_4, filtered, and the solvent removed on a rotovap. Distillation under vacuum (135-140°C at 0.25 torr) gave the desired phenol with a purity of 99.6 % by GC.

Chemical attachment of the precursor phenol to the surface of a nonporous silica (Cabosil M-5; 200 $m^2\ g^{-1}$; ca. 1.5 mmol SiOH g^{-1}) was accomplished as described below for the *p*-DPM isomer. *p*-$HOC_6H_4CH_2C_6H_5$ (6.085 g; 33.0 mmol) was dissolved in dry benzene (distilled from $LiAlH_4$) and added to a benzene slurry of silica (9.57 g; 14.4 mmol SiOH) that had been dried at 200°C for 4 h in an oven. Following stirring and benzene removal on a rotovap, the solid was sealed in a pyrex tube evacuated to 4 x 10^{-6} torr. The attachment reaction was conducted in a fluidized sand bath at 200°C for 1 h. Unattached phenol was removed by temperature-ramped sublimation under dynamic vacuum (250-375°C; 1 h; 0.02 torr). Surface coverage analysis was accomplished by dissolution of the solid (ca. 200 mg) in 30 mL of 1 N NaOH overnight. 4-Phenylphenol was added as an internal standard. The solution was neutralized by the addition of HCl, and extracted thoroughly with CH_2Cl_2. The solution was dried over $MgSO_4$, filtered, the solvent removed on a rotovap, and the resulting material silylated with *N,O*-bis-(trimethylsilyl)trifluoroacetamide (BSTFA) in pyridine (2.5 M). The corresponding trimethylsilyl ether derivative was analyzed by GC (HP 5890) on a J&W Scientific 30 m x 0.25 mm i.d. (0.25 μm film thickness) methyl silicone column with flame ionization detection. GC analysis gave a surface coverage of 0.43 mmol g^{-1} for the *para*- isomer (purity of 99.8 %), and a surface coverage of 0.29 mmol g^{-1} for the *meta*-isomer (purity of 98.2%).

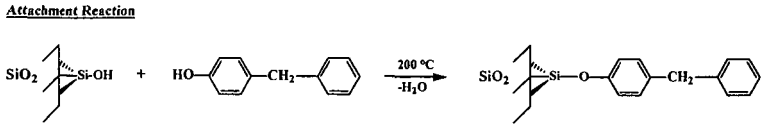

Thermolyses were conducted in sealed, evacuated (2 x 10^{-6} torr) T-shaped pyrex tubes in a temperature controlled furnace. Volatile products were collected as they were produced in a liquid nitrogen cold trap, and subsequently analyzed by GC and GC-MS with the use of internal calibration standards. Surface-attached products were similarly analyzed after digestion of the silica in aqueous base, and silylation of the resulting phenols to the corresponding trimethylsilyl ethers as described above for the surface coverage analysis.

Results and Discussion

Our initial studies of the thermolysis of the *para*-isomer of silica-immobilized diphenylmethane (≈*p*-DPM, 0.43 mmol g^{-1}) indicate that a slow reaction occurs at 425°C (conversion rate of ca. 1.2 % h^{-1}). The principal products are shown in the scheme below, and the selectivities are insensitive to the extent of ≈*p*-DPM conversion over the range

studied (1.8 - 18.0 %). Numerous higher molecular weight products can be detected in the GC trace, particularly at higher conversions. As expected, mass balances which are good (ca. 98% at low conversions) become progressively poorer at the higher conversions (ca. 87 % at 18 % conversion).

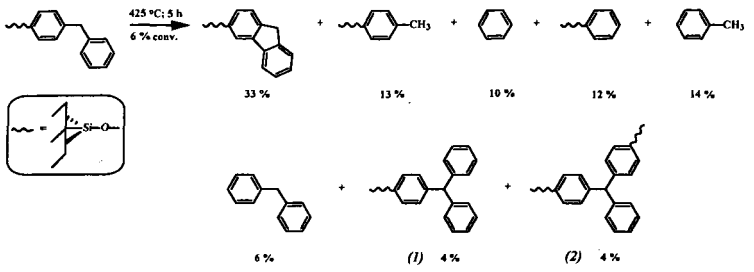

The major reaction path observed for ≈*p*-DPM is cyclization-dehydrogenation to form silica-immobilized fluorene, which is formed in a slightly higher yield (33 mol %) than reported in the liquid phase.[10] This is accompanied by hydrogenolysis of ≈*p*-DPM to form benzene and toluene products (both gas-phase and surface-attached), which is induced by hydrogen atoms released from the cyclization step. This suggests that the dominant reaction chemistry observed in fluid-phase studies of DPM can similarly occur under restricted mass transport conditions. Hydrogen atoms are also found to induce cleavage of the ≡SiO-$PhCH_2Ph$ bond which produces the $PhCH_2Ph$ product. Diphenylmethyl radicals, ≈PhCH•Ph, are thought to be the key intermediates in the cyclization to form fluorene, which are principally generated through hydrogen transfer propagation steps with gas-phase and surface-immobilized benzyl radicals. The initiation step for this radical chain process is not currently known, but a molecular disproportionation step seems most likely.[1,2] The efficiency of this radical chain pathway should be sensitive to the ≈*p*-DPM surface coverage as well as the structure of neighboring molecules on the surface, which is under current investigation. The formation of unexpectedly significant amounts of triphenylmethane products **1** and **2** (totaling 8 mol % of the products) is also consistent with the formation of diphenylmethyl radical intermediates, that undergo an aromatic substitution reaction on a neighboring molecule of $\approx PhCH_2Ph$ in competition with cyclization. This process appears

$$\approx PhCH\bullet Ph + \approx PhCH_2Ph \rightarrow \approx PhCH(Ph)Ph + \approx PhCH_2\bullet$$

to be promoted compared with fluid phases as a result of the restricted mass transport. Reduced rates for radical termination on the surface as well as the close proximity of the species at high surface coverages contribute to the emergence of this pathway.

To see if the orientation of the DPM molecule on the surface would impact the pyrolysis rate and product selectivities, we have prepared the *meta-* isomer of surface-attached DPM, ≈*m*-DPM. As we observed previously for other molecules, the *meta-* surface linkage leads to a lower saturated surface coverage (0.29 mmol g^{-1}) compared with the *para-* linkage (0.43 mmol g^{-1}) due to less efficient packing on the surface. Initial thermolyses indicate a slightly lower thermolysis rate for ≈*m*-DPM (ca. 0.7 % h^{-1}) at 425 °C, but the principal products shown below are quite similar. Cyclization occurring through the benzylic radical, ≈*m*-PhCH•Ph, can lead to two possible isomeric fluorene products, and the two isomers **3** and **4** are detected in comparable yields. The identification of **4** has been confirmed with an authentic sample of the corresponding 2-hydroxyfluorene (the product formed after detaching **4** from the silica surface) that was independently synthesized as described previously.[13a] The combined yield of fluorene formation, 23 mol %, is somewhat less than the yield observed for the *para-* isomer. The origin of this effect remains under investigation. The radical displacement chemistry that formed the triphenylmethanes, **1** and **2**, in the thermolysis of ≈*p*-DPM occurs with similar effectiveness for the *meta-* isomer and results in significant yields of triphenylmethanes **5** and **6**.

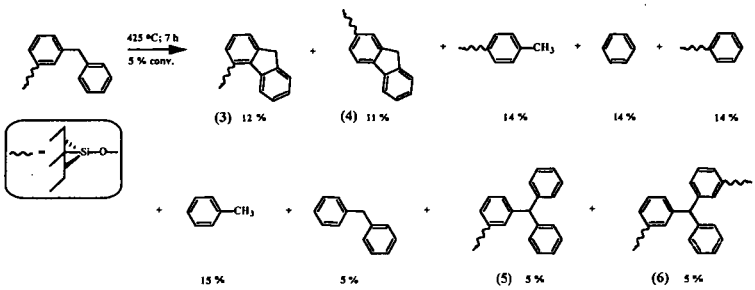

CONCLUSIONS

Thermolysis of diphenylmethane under restricted mass transport conditions has been found to occur slowly at 425°C by an apparent radical chain process cycling through diphenylmethyl radicals. At high surface coverages, these free-radical intermediates undergo competitive cyclization to form the polycyclic aromatic hydrocarbon, fluorene (major), and radical displacement on another diphenylmethane molecule to form triphenylmethanes (minor). The selectivity for these two pathways is 4.1 for the *para-* isomer of DPM and 2.3 for the *meta-* isomer indicating some sensitivity to orientation of DPM molecules on the surface. The hydrogen liberated from these processes results, as expected, in the unselective hydrocracking of DPM to form benzene and toluene products, and both material and hydrogen balances are good at the low conversions investigated. Future studies will examine the effect of surface coverage on the pyrolysis rates and product selectivities, and will explore the impact of a co-attached hydroaromatic spacer molecule such as tetralin.

ACKNOWLEDGMENTS

The authors express appreciation to K. B. Thomas for technical support. This research was sponsored by the Division of Chemical Sciences, Office of Basic Energy Sciences, U.S. Department of Energy, under contract No. DE-AC05-96OR22464 with Oak Ridge National Laboratory, managed by Lockheed Martin Energy Research, Corp.

REFERENCES

1. Poutsma, M. L. *Energy & Fuels* **1990**, *4*, 113, and references therein.
2. Murata, S.; Nakamura, M.; Miura, M.; Nomura, M. *Energy & Fuels* **1995**, *9*, 849.
3. Futamura, S.; Koyanagi, S.; Kamiya, Y. *Fuel* **1988**, *67*, 1436.
4. (a) McMillen, D. F.; Malhotra, R.; Chang, S.-J. *Fuel* **1987**, *66*, 1611. (b) Malhotra, R.; McMillen, D. F. *Energy & Fuels* **1990**, *4*, 184.
5. Autrey, T.; Alborn, E. A.; Franz, J. A.; Camaioni, D. M. *Energy & Fuels* **1995**, *9*, 420.
6. Mitchell, S. C.; Lafferty, C. J.; Garcia, R.; Snape, C. E.; Buchanan, III, A. C.; Britt, P. F.; Klavetter, E. *Energy & Fuels* **1993**, *7*, 331.
7. Shi, B.; Ji, Y.; Guthrie, R. D.; Davis, B. H. *Energy & Fuels* **1994**, *8*, 1268.
8. McMillen, D. F.; Ogier, W. C.; Ross, D. S. *J. Org. Chem.* **1981**, *46*, 3322.
9. Benjamin, B. M.; Raaen V. F.; Maupin, P. H.; Brown, L. L.; Collins, C. J. *Fuel* **1978**, *57*, 269.
10. Petrocelli, F. P.; Klein, M. T. *Macromolecules* **1984**, *17*, 161.
11. Sweeting, J. W.; Wilshire, J. F. K. *Aust. J. Chem.* **1962**, *15*, 89.
12. Suzuki, T.; Yamada, H.; Sears, P. L.; Watanabe, Y. *Energy & Fuels* **1989**, *3*, 707.
13. (a) Buchanan, III, A. C.; Britt, P. F.; Thomas, K. B.; Biggs, C. A. *J. Am. Chem. Soc.* **1996**, *118*, 2182. (b) Buchanan, III, A. C.; Britt, P. F.; Thomas, K. B. *Energy & Fuels* **1998**, in press. (c) Buchanan, III, A. C.; Biggs, C. A. *J. Org. Chem.* **1989**, *54*, 517. (d) Britt, P. F.; Buchanan, III, A. C. *J. Org. Chem.* **1991**, *56*, 6132. (e) Britt, P. F.; Buchanan, III, A. C.; Malcolm, E. A.; Biggs, C. A. *J. Anal. Appl. Pyrolysis* **1993**, *25*, 407. (f) Buchanan, III, A. C.; Britt, P. F.; Biggs, C. A. *Energy Fuels* **1990**, *4*, 415.

PREDICTING THE LIFE OF SKIRT SUPPORTS IN PRESSURIZED REACTORS UNDER CYCLIC CONDITIONS

Marcos Sugaya
Petrobras S.A., Cenpes
Rio de Janeiro 21910-900, Brazil

Colin McGreavy
The University of Leeds, Chem. Eng. Dept.
Leeds LS2 9JT, UK

KEYWORDS: pressure vessel, skirt support, thermal stresses

ABSTRACT

A common problem with skirt support is the occurrence of cracks originating at the outer boundaries of the welded junction. In order to understand the background on this, a study of the changes in temperatures and stress profiles has been undertaken by placing strain gages and thermocouples near the attachment region of an existing delayed coking reactor. Stresses arising from the differential thermal expansion, junction momentum and other contributions have been examined in terms of the Weil-Murphy analysis of the problem to provide a basis for validating models of stress failure.

INTRODUCTION

Mechanical designs of reactors are usually based on steady-state operating conditions and ignore stresses which arise during process transients, such as in emergencies or at start-up and shut-down. For continuous processes this is not a major problem because transients occur only infrequently. In the case of batch operations, however, transients are a normal part of the production cycle and so the effect need to be examined in more detail.

In particular, welded skirt supports of the type commonly used in vertical pressurized reactors are often subject to fatigue failure. The cycling causes abnormal transient thermal stresses in the vessel near these joints which tend to progressively weaken the structure. It is therefore important to look into ways in which this deterioration in the structural integrity can be mitigated by looking at the effect of transient changes occurring during batch operations particularly in terms of how the frequency and magnitude of the changes can be accommodated to ensure safer designs and how this might have to be reflected in operating policies which will maximize equipment life.

DIFFERENTIAL STRESS ANALYSIS

The main stress components at the skirt junction can be calculated using beam on elastic foundation theory (1) applied to a three-cylinder junction, as suggested by Weil and Murphy (2).

To assess fatigue, the stresses of major concern are those arising in the outer skirt region, since the weld is much more susceptible to this kind of failure than the vessel plates as has been verified in studies of the origins of cracks occurring in operational units. All the evidence suggests that the outer surface of the attachment weld is the starting point.

During the normal operation of the drums, heat flows from the hot vessel walls to the skirt attachment. When the reactor is cooled, the flux is in the opposite direction. The calculation of thermal stresses (which are the major components) requires thermal gradients to be estimated in the skirt, shell and conic sections. The largest gradients occur near the junction because the flow of heat to or from the skirt is by conduction through, although radiation and convection between the conic and skirt sections are important if there is no insulation. Heat accumulates as a result of the axial heat flow and causes the magnitude of the gradients to decrease away from the region.

In this study, thermocouples were placed close to the weld at the skirt, shell and conic sections and are spaced at short intervals (Figure 1). At low heat flux, the temperature differences between neighboring points are similar but because the gradients are estimated by finite difference approximation, the numerical estimate is subject to noise (Figure 2). Mean gradients for the shell, skirt and conic sections can be calculated using the temperature readings over wider intervals. It can be seen that this represents the average behavior fairly well (Figure 2) and effectively filters out the noise. Consistency in the results can be verified by comparing these

values with those estimated for adjacent thermocouples then computing an average gradient (for example, calculating the average gradient at the shell both with (NE1-NE5)/4 and (NE2-NE5)/3.

RESULTS AND DISCUSSION

During the cooling operation, the reactor full of coke is quenched with water. Figures 3-6 present the temperature change at four angular positions. Before switching the reactor (10.47 h), heat flows axially from the shell to the skirt and cone (Figures 7-10). This is consistent with the assumption of a main flow channel located centrally inside the vessel. The furnace effluents flow up through this channel to the top of the coke bed where the hot liquid accumulates. The coke deposited around the walls of the shell and conic sections acts as an insulating layer, limiting heat flow to the axial direction. As the drum fills up, the highest wall temperatures gradually move upwards. The lower part of the wall gradually cools down because heat is lost through the external insulation, but the temperatures are maintained at somewhat lower levels by axial and radial heat transfer. The temperature at the inlet nozzle is 490 C with the wall temperatures gradually falling from 390-435 C (a few hours after the drum starts to fill) to 300-325 C (before the next switch).

The temperatures in the lower left quadrant before the switch are somewhat higher than in the other positions, which are fairly uniform (Figures 3-6). This suggests that the main channel is located off-center and close to this quadrant. However, during cooling, the upper right quadrant cools faster. Had the channel being located closer to the lower left, it would have cooled faster, since quench water could be expected to spread radially from the central channel towards the walls. The most difficult zone to cool is the first quadrant, only being active after 9.6 hours. This means that this region behaves as if no cooling has taken place.

In Figures 3-6 it can also be seen that the switch and the steam stripping stages (both the 'small', 5 t/h, initiated immediately after the switch and the 'large', 15 t/h, initiated at ~ 11.85 h) do not seem to contribute to cooling of the reactor walls, since the temperatures remain unchanged during these operations. The heat transfer between the steam and the coke is poor, since convective heat transfer coefficients are known to be much smaller than boiling coefficients. It is also difficult for the steam to flow through the parts of the coke bed closer to the vessel walls. Strictly, an enthalpy balance on the steam during the stripping cycle is necessary to clarify this point but the top temperature is not accessible. The temperature of the gasoil quench remains constant during steaming, which suggests that only the central portions of the coke bed are exchanging heat.

It should also be noted that the production of lighter fractions due to thermal cracking is still significant even a long time after the switch has been made. The steam mixes with the vapors resulting only in a small temperature drop at the top. This requires estimating the oily fractions recovered from the blowdown system in order to compare the relative flow rates of hydrocarbons and steam at the top.

Increasing the pressure in the drum during the stripping operation would be beneficial to make it possible to penetrate deeper into the coke bed and so reduce the partial pressure in the zones closer to the walls. This increases the removal of hydrocarbons and cools the coke bed.

The important features contained in Figures 3-6 relate to the differences in the local curves, not the trend suggested by the general rate of change in temperature reflected in the different quadrants. Thus, the local spatial gradients in NW do not change much with time and the average value of temperature changes little. On the other hand, there is a significant change in average local temperature in SW ~200 C but little change in the local temperature differences, so the local gradient remains more or less constant. In the case of NE and SE, the local gradients are larger during part of the transient because of increases in local temperature differences. It is clear that the rate of change of temperature with time is not therefore in itself an indicator of significant changes in temperature gradient and by implication the local stress.

The calculated stresses are all very small (Figure 11 shows the longitudinal stresses at the outer skirt as an example) and far from the yield limit (~ 210 MPa). This is to be expected considering the modest thermal gradients observed. In the third quadrant the forces are slightly lower and decline faster than at other positions. On the other hand, in the first quadrant there is change from tension to compression at a certain point, which is important in fatigue assessment if fast quench rates results tend to exacerbate this. Generally, no residual forces seem to remain as the vessel is cooled down, apart from those due to the weight of coke and water.

As water evaporates, the pressure rises and if care is not taken, it can result in activation of the safety valve, causing a shut-down. A delay occurs in the response of the pressure to the water flow rate and the pressure sometimes rises, even after the water flow rate has been reduced, and requires careful attention to ensure it does not cause problems.

One strategy used is to close the top valve a little in order to increase the pressure in the vessel. This practice has originated in a plant where the delayed coking units tend to be a

As water evaporates, the pressure rises and if care is not taken, it can result in activation of the safety valve, causing a shut-down. A delay occurs in the response of the pressure to the water flow rate and the pressure sometimes rises, even after the water flow rate has been reduced, and requires careful attention to ensure it does not cause problems.

One strategy used is to close the top valve a little in order to increase the pressure in the vessel. This practice has originated in a plant where the delayed coking units tend to be a production bottleneck. Experience has shown that restraining the top valves promotes radial flow of water through the coke bed, which accelerates cooling.

Successive runs show that parts which appear to be difficult to cool change randomly, indicating that the main channel is deviating from the center. Before the cooling stage, heat flows towards the junction at the shell and away from the junction at the skirt and conic sections. This is followed by heat flow in the opposite direction in the shell and skirt immediately after the cooling phase. The gradients in the conic section are initially positive then decrease soon after the start of the cooling cycle. Sometimes they are negative or increase again after a short drop.

The skirt and cone generally have more similar temperatures. The slower cooling rates and the gradients which develop in the conic section are caused by competition between the heat removed from the wall to the coke bed and heat supplied by the skirt attachment through the welded joint, as well as by radiation and convection. The form of the weld can also cause the heat which is retained in the skirt to move into the conic section which would explain why the shell cools faster than the conic section.

Figures 12-20 show that for rapid preheating (sometimes the cycle is delayed and requires heating the drum at a fast rate), variations of 1.6 C/min are obtained, which compare with the 1.6-1.8 C/min reported by Lieberman for a fast warm-up operation where one third of the vapors from the full drum are by-passed to the empty one (3). The high temperature gradients result in higher thermal stresses than those found in any of the cooling runs analyzed, but are still less than the yield limit.

CONCLUSIONS

The results indicate that the stresses that define the life of the skirt attachment weld on a fatigue basis are mainly established during warm-up or perhaps shortly after switching on. The inversion of stresses observed during the cooling operation at the outer region is mild and does not seem to be significant as far as fatigue assessment is concerned.

Switching to a cold drum should be avoided if at all possible. The results reported here suggest that this event could give rise to significant stresses in the coke drum, higher than for any other case and probably above the yield limit. To assemble useful information, it is necessary to have access to a suitable model since collection of experimental data on an extended experimental program is not feasible.

The results illustrate the importance of operational practices. Policies designed to increase the life of the skirt attachment weld should focus on warm-up and switch conditions or factors that could reduce the available time for warm-up (such as a delay in cutting the coke or an excessively slow cooling operation). Design should ensure sufficient drum capacity.

REFERENCES

1. Hetenyi M. Beams on Elastic Foundations 1946.
2. Weil N. A.; Murphy J. J. Journal of Engineering for Industry 1960, Feb., 1.
3. Lieberman N. P. Oil & Gas Journal 1983, Aug.29, 39.

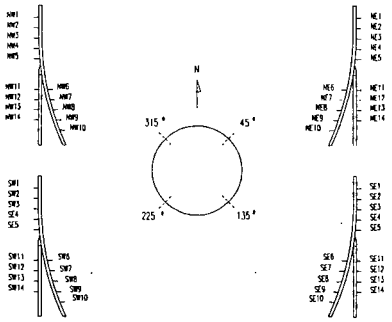

Figure 1 Location of thermocouples at the shell-skirt junction.

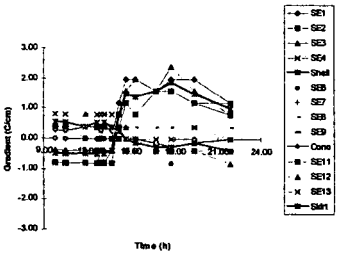

Figure 2 Typical axial temperature gradients. Positive values indicate heat flowing from the junction, dark lines represent average values.

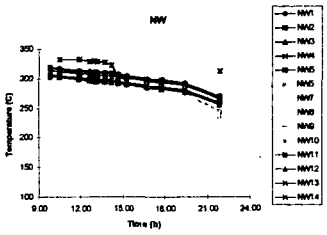

Figure 3 Skin temperatures at NW.

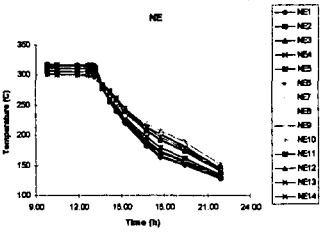

Figure 4 Skin temperatures at NE.

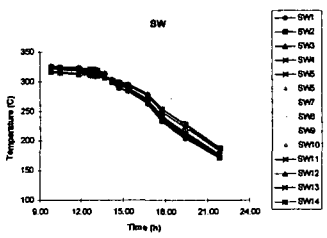

Figure 5 Skin temperatures at SW.

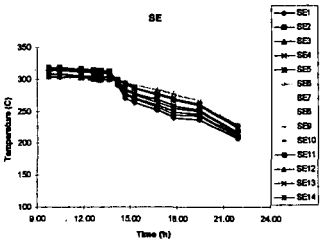

Figure 6 Skin temperatures at SE.

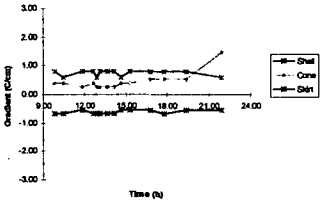

Figure 7 Axial gradients at NW.

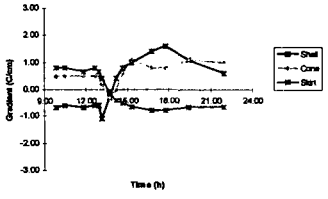

Figure 8 Axial gradients at NE.

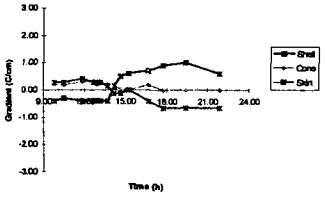

Figure 9 Axial gradients at SW.

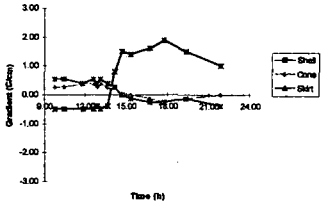

Figure 10 Axial gradients at SE.

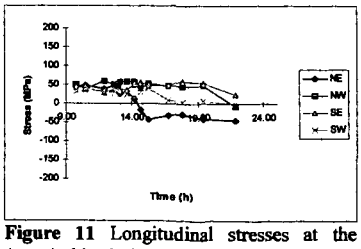

Figure 11 Longitudinal stresses at the (outer) skirt during cooling.

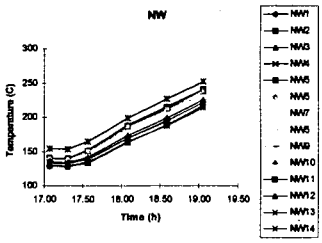

Figure 12 Temperatures at NW.

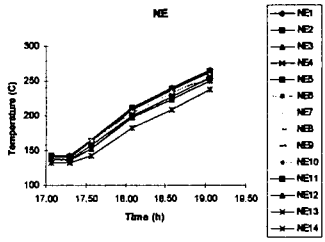

Figure 13 Temperatures at NE.

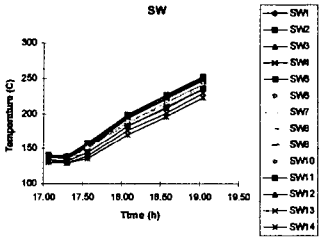

Figure 14 Temperatures at SW.

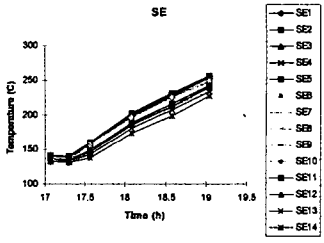

Figure 15 Temperatures at SE.

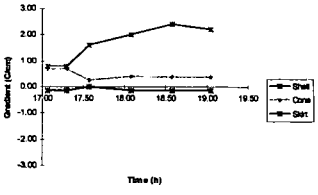

Figure 16 Axial gradients at NW.

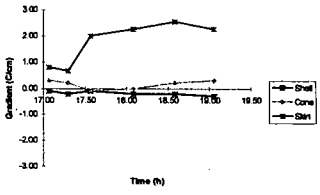

Figure 17 Axial gradients at NE.

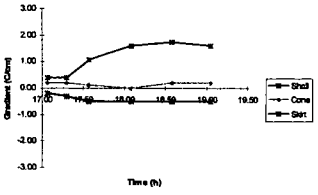

Figure 18 Axial gradients at SW.

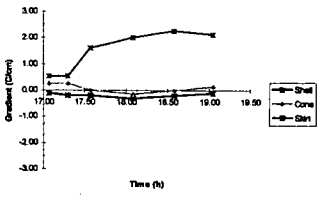

Figure 19 Axial gradients at SE.

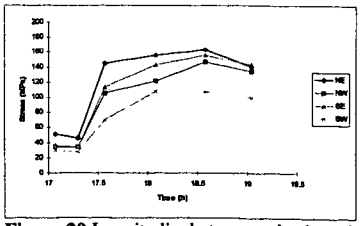

Figure 20 Longitudinal stress at the (outer) skirt during a fast pre-heating operation.

COST EFFECTIVE EVALUATION TECHNIQUES FOR FCC ATOMIZING NOZZLES

Edson José Joaquim de Souza
Aurélio Medina Dubois
Petrobras Rod. Br 476, Km 143
São Mateus do Sul-PR
83900-000 Brazil

KEYWORDS: FCC NOZZLES; NOZZLES EVALUATION; FCC FEEDING IMPROVEMENT

INTRODUCTION

The improvement of gasoline yields and quality on FCC plants has been a must on the field of oil industry research and development over the last several years. The high inlet processing volumes make any improvement either in conversion or product quality result in very high levels of financial savings. There is an important relationship between the oil feeding quality and the oil-catalyst interaction which leads to such better yield and quality upgrade[2].
The complete uniform mixing of catalyst and oil has become a challenging target for FCC plant engineers and designers around the world. Besides the usage of heavier input oil makes such a mixing even more important. The oil-catalyst contact, vaporisation and residence times in the riser environment are all involved with inlet oil spray pattern. Some of the most important figures on feeding quality such as the droplet diameter, mass flow distribution on spray and momentum depend on the FCC atomisation nozzle. This paper discusses some on plant, cost-effective evaluation techniques, which may be applied by FCC plant engineers in order to choose a good feeding tip for their needs. High-speed photography, mass distribution measurements and other simple but effective evaluation procedures are discussed. Also a nozzle case study is shown, whose evaluation was carried out by such a set of techniques under several conditions.

FCC FEEDING NOZZLES

There are many commercial feeding nozzles types available on FCC technology world-wide. However about a dozen of such a models have been mostly used on plants lately. Some devices have registered marks and they are protected under patents.
The most used nozzle atomizer type is the twin-fluid atomizer. Those devices use a high velocity atomizing fluid, which impinges on a liquid traverse flow. The high relative velocity between the two fluids causes a very rapid deformation of the liquid film, the sheet break up, the formation of ligaments, drops and droplets.
In order to select a good tip for any specific need a FCC engineer may carry out an evaluation plan. The feeding oil physical and chemical properties, the atomizing steam availability, the pumping power and other operating conditions must be considered.
An effective evaluation plan must focus on the main known features of a good tip. As a matter of fact a good nozzle must fulfil a set of features as follows: Small droplet diameter under a narrow distribution[3]; uniform flow rate on spray; symmetrical flat shaped spray; stability; easy manufacturing and maintenance; life-span; turndown and performance.

EVALUATION PLAN

A challenging target in testing FCC nozzles on test rigs is the safe scale up and down process and the usage of test fluids instead of oil and steam. The usage of actual fluids on test rigs is difficult and even dangerous, due to the hazardous oil properties. Besides the test cost may increase considerable so a good choice is to replace oil by water and steam by compressed air.
Another well-used method is the tip scale up and down process to avoid the high mass flow rates used by the full-scale nozzle. Both methods may be used under strict theory rules otherwise the results from test rig fail. Above all there are some important

parameters and dimensionless numbers must be checked.

	Liquid	Gas
Density (ρ_L)	ρ_L	ρ_G
Viscosity(ν)	ν_L	ν_G
Surface tension(σ)	σ	
Relative velocity ($U_r=U_G-U_L$)	U_L	U_G
Reynolds Number (Re)	$R_e = \rho_L.U_L.d_0.\nu^{-1}$	
Weber Number (We)	$W_e = \rho_L U_r^2.d_0\sigma^{-1}$	
Initial jet diameter d_0		

On twin fluid atomizer theory the most important parameter is the Weber number[1]. The feeding oil and atomizing steam under their operating conditions must have the above parameters as close as possible to the testing fluids, i.e. air and water at ambient temperature[4]. Also tips scale up and down cannot properly succeed without such a set of parameters relationship. Furthermore scale down process using mass flow ratio by a factor over say, four times are not recommended as well. Fortunately FCC feedstock and steam have atomizing parameters quite similar to water and air at test rig conditions.

SOME EVALUATION TECHNIQUES

Some of the most effective measurement techniques for FCC atomizers are related to the oil spray pattern analysis. There are many quantitative and qualitative methods that may vary in cost, applicability and reliability. This paper discusses some cost effective "on plant" techniques that may be used by FCC plant engineers. They are: the nozzle test rig and apparatus; droplet sizing by high-speed photography; mass flow rate distribution and pressure profile measurement.

NOZZLE TEST RIG

A simple but effective test rig can be built up beside any utility facility on a FCC plant. All need utilities can be easily found such as water and compressed air. The rig flow capacity may be designed to test full-scale nozzles or scaled down model tips. Measurements of water and air flow rates can be easily achieved by conventional flow meters.

DROPLET SIZING

One of the most famous droplet sizing technique is the laser scattering. Some good overall advantages are:
-It is a non-intrusive method so the spray pattern is not disturbed [1].
-There is a fast, quantitative result such as the droplet distribution and mean diameters (SMD, the Sauter Mean Diameter, for instance).
Some few, but not less important disadvantages are:
-Scattering light devices are not suitable for dense sprays [1] (FCC nozzles produces typically dense sprays, even using a scale down model).
-The scattering light principle considers a droplet a globular shaped body. This is not true because the surrounding areas downstream the tip contains ligaments with typically non-globular shape.
-It demands investments on lab-like test rigs, equipment and high qualified technical staff.

HIGH-SPEED PHOTOGRAPHY

An alternative droplet sizing technique is the high-speed photography. It is not a quantitative method but it can give us a good idea about the spray pattern and droplet size (comparison). The high cost and difficult to use old spark flashes are not effective anymore. Nowadays a high-speed photographic system can be built up using only almost conventional devices (fig. 1). A simple set was successfully used to carry out tests on a group of FCC nozzles.
The camera does not need to have high speed shutter capabilities[5]. As matter of fact

even special high-speed shutters are enable to "stop" the spray image because the droplets velocity stream. The shutter is kept open while the trigger is pressed (on the "B" setting). The photo is taken in the darkness and the exposition time is the flash duration. An EG&G high-speed flash may produce a lightning as fast as 1/50,000 of a second. The speed film such as ISO 400 B&W is satisfactory (fig.2). Some conventional amateur electronic flash may be also used but the light is not powerful enough for quality photos.

MASS FLOW RATE DISTRIBUTION

A flat shaped spray may produce several mass flow rate patterns even with the same droplet mean diameter. Basically one of the oil/catalyst mixing goals is to inject the feedstock where the catalyst is and so a uniform mass flow distribution is required. Some commercial nozzles have good droplet mean diameter but poor mass flow distribution. Using a simple cell box device the mass flow distribution measurement can be carried out (fig 3). Also a distribution histogram of the collected water is shown. Many nozzles release much flow at the spray centre producing a non-ideal pattern(fig. 4).

STATIC PRESSURE DOWNSTREAM THE SPRAY

The pressure profile downstream the feeding nozzle used to be negligible in the early days of FCC feeding development. However low pressure zones downstream the atomization chamber may induce dangerous backward catalyst flow (inside Riser). The catalyst may impinge on the nozzle top at high velocity by means of backward stream. Sometimes the erosion is so hard that whatever the tip material is it may last only few hours. The pressure profile along the nozzle chamber and in the first feet downstream the top may vary under different operating conditions. A good nozzle should keep positive pressure on its turndown range. Using mercury U gauges such a pressure can be easily measured.
The pressure profile (example on fig.5) on tips is strongly dependent on geometry and pressure drops. Sometimes the chamber geometry, liquid injection angle, and mass flow liquid/gas ratio result in different pressure levels.

CASE STUDY

The set of techniques shown on this paper was successfully applied on a group of nine up to date FCC nozzles. The main target was to carry out a comparison study between the Petrobras UltraMist^{R} FCC nozzle and other commercial tips. All evaluation techniques discussed on this paper were successfully applied. Although the droplet sizing by high-speed photos results qualitative analysis, some good points and bad points were highlighted. Such a nozzle has got a good and uniform mass flow distribution, small droplet mean diameter and stability. Other commercial nozzles achieve good standard features as well. However there are some conflicting features they should be managed, such as droplet diameter and pressure profile.

REFERENCES

1) Yule, A.J. et al, 1996,"Atomizer and spray technology", notes in support of the 10th UMIST short course, University of Manchester.
2) Wrench, R.E. et al, "FCC Hardware Options for the Modern Cat Cracker", AIChE Symposium Series.
3) Sapre, A.V. et al, " Design Methods for FCC Feed Atomization", AIChE Symposium Series, no 291, vol.88
4) Simmons, H.C., Harding C.F., 1981,"Some Effects of Using Water as a Test Fluid in Fuel Nozzle Spray Diagnostics", transactions of the ASME,Vol. 103, Jan/81.
5) Winters, L.M.,1996, "High Speed Flash Photograpy for Amateur Photographers"; North Carolina Shool of Mathemetics Science.

FIGURES

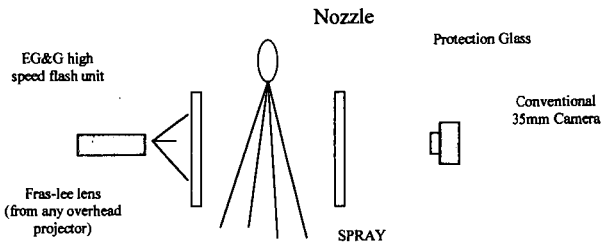

fig1. High-speed photography system-Schematic of apparatus

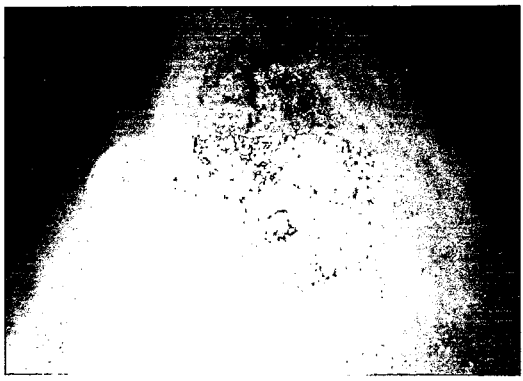

Fig.2 High speed photography (liquid flow rate=3230 Kg/h; air flow rate 100 Nm^3/h)

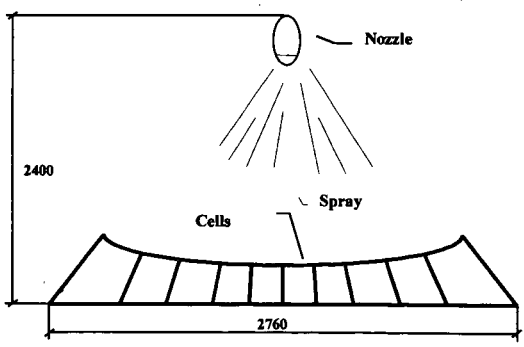

Fig.3 Cell box for flat spray flow distribution

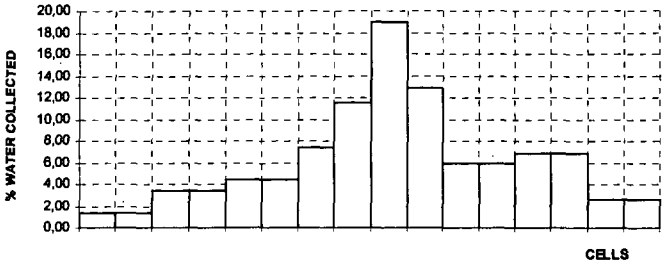

Fig.4 Mass flow rate on the spray-Histogram from the cell box

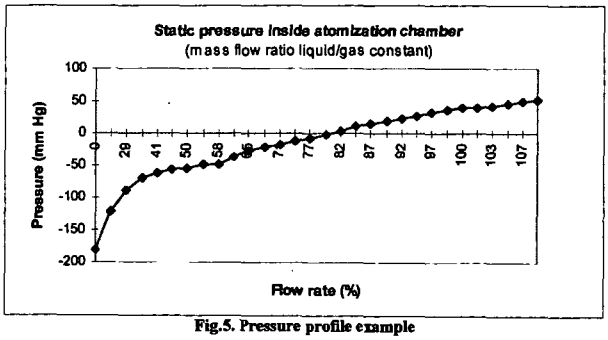

Fig.5. Pressure profile example

ULTRASONIC CHARACTERIZATIONS OF SLURRIES IN BUBBLE COLUMN REACTORS

Y. Soong*, A. G. Blackwell, F. W. Harke, E. P. Ladner, and M. F. Zarochak, U.S. Department of Energy, Federal Energy Technology Center, P.O. Box 10940, Pittsburgh, PA 15236, U.S.A.

Key words: ultrasound, solid holdup, bubble columns

INTRODUCTION

For the optimum design and operation of gas-liquid-solid three-phase reactors, the degree of dispersion of the solid (catalyst) in the reactor must be understood and controlled. Recently, a method involving the measurement of ultrasound transmission has been reported in a slurry-phase stirred-tank reactor which offers the possibility of using the ultrasonic technique to measure solid holdup in a three-phase slurry reactor (1-3). The ultrasonic transmission uses measurements of the velocity and attenuation of the sound wave which travels directly through the slurry sample. When an acoustic wave strikes the boundary between two different media (liquid and solid) and the acoustic impedances of the two media are different, some acoustic energy will be reflected, absorbed, and some will be transmitted. The reflected wave travels back through the incident medium (liquid) at the same velocity. The transmitted wave continues to move through the new medium (solid) at the sound velocity of the new medium. When the velocity of sound in a liquid is significantly different from that in a solid, a time shift (a velocity change) 9n the sound wave can be detected when solid particles are present relative to that for the pure liquid. The amplitude of the sound wave is also reduced when a solid particle is present since the wave is partially scattered and absorbed. Therefore, a change in amplitude of the sound wave can also be detected when solid particles are present relative to that for the pure liquid. Okamura et al. (1) and Soong et al., (2-4) used a continuous stirred-tank reactor to correlate the solid holdup to the relative time shift $[(t_a-t_b)/t_o]$. Furthermore, the application of the measurement of ultrasound transmission for gas holdup (5-7) and for gas holdup as well as low concentration of solid (up to 1 wt. %) under limited superficial gas velocities (up to 3 cm/s) in a slurry-bubble-column reactor has been reported (8,9). This leads to the initial study of using the ultrasonic technique for the measurement of solid holdup in a three-phase gas-liquid-solid bubble column reactor over a wide range of superficial gas velocities and solid holdup.

EXPERIMENTAL

A schematic representation of the bubble-column-reactor in which the ultrasonic investigation was conducted is shown in Figure 1. The transparent acrylic bubble-column-reactor has an internal diameter of 8.89 cm and a height of 290 cm. The column has six different axial locations for data collection. The ultrasonic signals are transmitted at 33 cm above the bottom of the gas distributor, which is a perforated-plate gas distributor with 15 x 1 mm diameter holes, along the center of the bubble-column-reactor. Experiments were conducted in batch-mode operation (stationary liquid-water and continuous flow of gas-nitrogen). Nitrogen bubbles were introduced through the gas distributor plate located at the bottom of the reactor. The nitrogen flow was controlled electronically to a maximum of 12 cm/s through a mass-flow controller. Glass beads from Cataphote, Inc., (10-37 μm in diameter with density of 2.46 g/cm^3) were used as the solid in the slurry. The solid holdup (solid weight/total slurry weight) was varied from 5 to 30 wt. % for each nitrogen flow in the reactor. To evaluate the accuracy of the ultrasonic technique for solid holdup measurement, an independent slurry sampling device was installed. The measurement was conducted by inserting a stainless steel tubing (0.775 cm. I.D.) horizontally into the center of the column at 0.635 cm above the path of the ultrasonic transmission. For each sampling, a 10 cm^3 of slurries sample was collected and analyzed for solid holdup characterization. The ultrasonic transmitter/receiver and the solid sampling device are positioned such that both means are measuring approximately the same hydrodynamic phenomena as shown enlarged areas in Figure 1. The detailed information of the ultrasonic unit has been reported elsewhere (2-4). Data were obtained with longitudinal waves at a frequency of 1 MHz using lithium niobate transducers. Both the transmitter and receiver were mounted directly inside the reactor wall at 33 cm above the gas distributor.

RESULTS & DISCUSSION

Figure 2 illustrates the effects of the superficial gas velocity (SGV) on the transit time [an arbitrary first distinct zero crossing time in the ultrasonic signal; the details have been described elsewhere (2)] and on the gas holdup in the reactor. The average gas holdup was determined by visual observations of the expanded bed height versus the static bed height. During this process, we have visually identified the various flow regimes since our bubble column is transparent. Basically, three flow regimes were identified in the bubble column. The homogeneous flow regime was observed when the SGV is 2.4 cm/sec or less. The average gas holdup in this regime was found to increase linearly from 0.015 at a gas velocity of 0.26 cm/sec to 0.093 at a SGV of 2.4 cm/sec. A transition flow regime exists between the SGV of 2.4 and 4 cm./sec. A slug flow regime is established when the velocity is 4 cm/sec or higher. The average gas holdup increased from 0.1 to 0.148 when the flow regimes changed from transition to slug flow. The transit time does not have an apparent correlation with the SGVs. It was approximately 72 μs at all SGVs and all flow regimes. Because what we measured was the signal that not transmitted through the nitrogen. Chang et al. (5) also reported that the amplitude of the transmitted sound pulses depends significantly on the number of bubbles; however, the transit time does not change with the void fraction. Uchida et al. (8) also measured the gas holdup in a bubble column for a gas-liquid system through determining the variation in transit time ratios. More recently, Warsito et al. (9) reported the measurement of gas holdup in a bubble column using the ultrasonic method. A change in transit time of 0.09 μs as the gas holdup increased from 0.05 to 0.1 was reported from their system. In current study, we did not observe such a change in transit time as the gas holdup increased from 0.05 to 0.1 in our system. The discrepancy may be due to different experimental setup or other factors. The small variation in transit time in this study is probably due to the experimental errors rather than the effect of nitrogen flow.

Figure 3 shows the change in the amplitude ratio of the transmitted ultrasonic signals A/A_o and the local gas holdup in the reactor as a function of the SGV. A and A_o are the amplitudes of the transmitted signals with and without the presence of nitrogen, respectively. Figure 3 suggests that the amplitude ratio is approximately an inverse exponential function of the SGV when the column is operated in the homogeneous flow regime (SGV of 2.4 cm/sec or less). No discernible relationship between A/A_o and SGV could be found when the latter is higher than 2.4 cm/sec, i.e., while the column is operating in transition or slug flow regimes. When a large nitrogen bubble (slug) passes across the ultrasonic transmitted path, the transmitted signal will be reduced significantly. The transmitted signal will regain some amplitude immediately after the slug has passed through the transmitted path. Therefore, a large scatter of the A/A_o ratio is observed at SGV of 2.4 cm/sec or higher. These phenomena could be observed while the column was operated in the transition or slug flow regimes. Chang et al. (5) measured void fractions up to 20% in bubbly air-water two phase flow using an ultrasonic transmission technique. Their results also showed that the A/A_o ratio has exponential relationship with the void fraction and a function dependent on the bubble diameter. The effect of air bubble diameters on A/A_o ratio was found to be significant where A/A_o decreased with increasing bubble size. Bensler et al.(6) also conducted the measurement of interfacial area in bubbly flows in air-water systems by means of an ultrasonic technique. Their observations suggest that the A/A_o ratio has an exponential relationship with the interfacial area and the scattering cross section, which depends on the bubble radius (a) and the wave number (k) of the ultrasonic wave surrounding the bubble. Our observations of A/A_o in the nitrogen/water system are in qualitative agreement with those reported by Chang et al. (5) and Bensler et al.(6).

Figure 4 shows the effect of gas velocity (SGV) on amplitude ratio (A/A_o), transit time, and average gas holdup in three-phase systems (30 wt. % of glass bead/nitrogen/water) in the bubble column reactor. A and A_o are the transmitted signals with and without the presence of solids, respectively. The similar flow regimes' patterns were also observed in the three-phase system (Figure 4) as those in a two-phase system (Figures 2 and 3). The fluctuation patterns of the A/A_o along with different flow regimes in Figure 4 are similar to that in Figure 3. Unlike the constant transit time observed in Figure 2 for a two-phase system, the transit time in a three-phase system is related to the flow regimes operated and the presence of solids. The transit times were 70.56 and 70.52 μs, respectively, for superficial gas velocities of 0.537 and 1.611 cm/sec when the column is operated in the homogeneous flow regime. In the transition flow regime, the transit time increased from 70.8 to 70.88 μs as the SGV changed from 0.537 to 12.05 cm/sec suggests that there was variation in the concentration of solids in the ultrasonic path. For example, partial sedimentation occurred when the SGV was 2 cm/sec or less. Thus the concentration of solids

should be high under these conditions. The detected constant transit time of approximately 70.88 μs in the slug flow regime suggests that there is a complete suspension of solids when the SGV is 4 cm/sec or higher. Kölbel and Realek (10) indicate that sedimentation will occur when the bubble column is operated under 2 cm/sec or less and the complete suspension of the solid will be established when the column is operated at 4 cm/sec or higher. Our ultrasonic observations are in good agreement with this finding.

Figure 5 illustrates the effects of solid holdup on the transit time measured at 33.65 cm above the gas distributor in the glass beads/nitrogen/water system at different SGVs. In this experiment, the SGV was systematically varied at any given initial solid holdup of 5, 10, 20, and 30 wt. % in the bubble column reactor. In general, the transit time varies with the variation of the superficial gas velocity for the SGV of 4 cm/sec or less at any given initial constant solid holdup loading in the reactor. The transit time was relative constant when the SGV is 4 cm/sec or higher. The transit times are around 71.96, 71.6, 71.12 and 70.88 μs for the solid holdup of 5, 10, 20, and 30 wt. % respectively, when the SGV is 4 cm/sec or higher. Therefore, the transit time can be utilized to determine the solid holdup when the column is operated in a complete suspension mode. The fluctuation of the transit time when the SGVs is 4 cm/sec or less may attribute to the both partial sedimentation and other factors which is under investigation

The fractional change of transit time [□ $t/t_o=(t_a-t_b)/t_o$] can be calculated on each individual transit time in Figure 5. From the fractional change of transit time, the solid holdup can be determined from the previous calibrated curve obtained from a stirred tank reactor [Figure 11. in (2)]. The determined solids holdup from these procedures and the solid holdup determined by the direct sampling are illustrated in Figure 6. The solid holdup measurements by the ultrasonic technique compared reasonably will with results obtained by the direct sampling techniques. Some discrepancies observed between these two techniques are probably due to the nature of these techniques. The ultrasonic technique measures the average solid holdup in the ultrasound path while direct sampling determines the collected local solid holdup.

CONCLUSIONS

An ultrasonic transmission technique has been developed to measure solid holdup in a gas-liquid-solid bubble column reactor. The results presented in this study show that the transit time of an ultrasonic signal is influenced by the variation of solid holdup and the operating conditions in the bubble column. The transit time can be correlated to the solid holdup. The variation of nitrogen flow has little influence on the observed transit time within the two-phase flow conditions studied. The ultrasonic technique is potentially applicable for solid holdup measurements in slurry-bubble-column reactors.

REFERENCES

1. Okamura, S., Uchida, S., Katsumata, T., Iida, K., *Chem. Eng. Sci.*, **1989**, 44, 196.
2. Soong, Y., Blackwell, A. G., Schehl, R. R., Zarochak, M. F., Rayne, J. A., *Chem. Eng. Com.*, **1995**, 138, 213.
3. Soong, Y., Gamwo, I. K., Blackwell, A. G., Schehl, R. R., Zarochak, M. F., *Chem. Eng. J.*, **1995**, 60, 161.
4. Soong, Y., Gamwo, I. K., Blackwell, A. B., Harke, F. W., Schehl, R. R., Zarochak, M. F., *Ind. Eng. Chem. Res.*, **1996**, 35, 1807.
5. Chang, J. S., Ichikawa, Y., Irons, G. A., Morala, E. C., Wan, P. T., Measuring Techniques in Gas Liquid Two-Phase Flows, Delhaye, J. M. and Cognet, G., Eds, Springer-Verlag: New York, **1984**, p319.
6. Bensler, H. P., Delhaye, J. M., Favreau, C., *Proc. ANS Natl. Heat Transfer Conf.*, **1987**, 240.
7. Soong, Y., Gamwo, I. K., Blackwell, A. B., Harke, F. W., Schehl, R. R., Zarochak, M. F., *Chem. Eng. Comm.*, **1997**, 158, 181.
8. Uchida, S., Okamura, S., Katsumata, T., *Can. J. of Chem. Eng.*, **1989**, 67, 166.
9. Warsito, A., Maezawa, A., Uchida, S., Okamura, S., *Can. J. of Chem. Eng.*, **1995**, 73, 734.
10. Kölbel, H., Ralek, M., *Catal. Rev-Sci. Eng.*, **1980**, 21, 225.

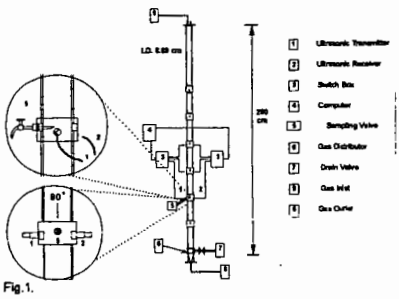

Fig.1.

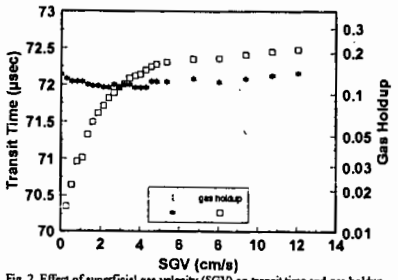

Fig. 2. Effect of superficial gas velocity (SGV) on transit time and gas holdup in nitrogen-water system.

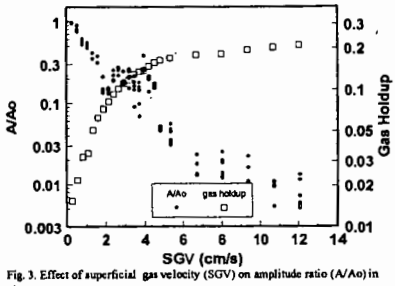

Fig. 3. Effect of superficial gas velocity (SGV) on amplitude ratio (A/Ao) in nitrogen-water system.

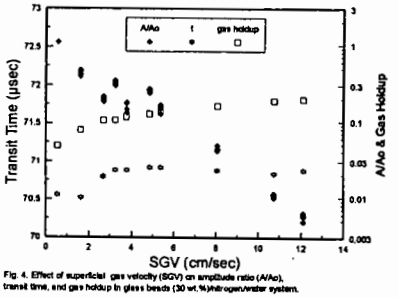

Fig. 4. Effect of superficial gas velocity (SGV) on amplitude ratio (A/Ao), transit time, and gas holdup in glass beads (30 wt.%)/nitrogen/water system.

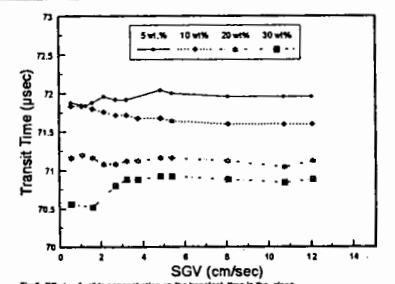

Fig 5. Effects of solids concentration on the transient time in the glass beads/nitrogen/water system.

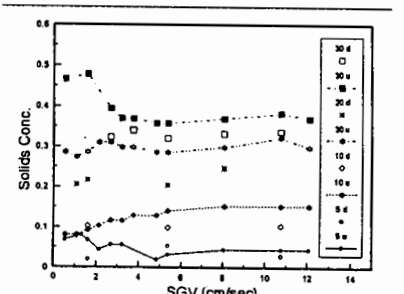

Fig 6. Solid Conc. determined by ultrasonic and direct sampling.

Selection of Optimized Vessel Geometries for Coiled Stirred Tank Reactors

S. M. C. Peixoto and J. R. Nunhez *
Faculdade de Engenharia Química – UNICAMP
Departamento de Processos Químicos
Cidade Universitária Zeferino Vaz
Cx Postal 6066 – Campinas – SP –Brazil – 13090-010

Keywords

Heat transfer in stirred tanks; computational fluid dynamics, helical coils, reactor design.

Abstract

Stirred Tank Reactors are extensively used in chemical industries. It is common to use either jackets or internal coils when the reaction inside these reactors is highly exothermic. Both arrangements have positive influence and drawbacks in controling the bulk temperature.

The design of coiled vessels today follows very much the geometry by Oldshue and Gretton [4] which has been criticized since it affects the flow. Street and McGreavy [6, 5] and Nunhez and McGreavy [3, 7, 2] indicated that if coils are placed in the same height of the impeller blades, internal flow circulation is restricted, even though there is an excellente local heat transfer in the impeller region.

This work aims to show by simulating the momentum, mass and energy equations inside the reactor, that there is great gain in performance if small alterations in the internals location are made. The idea is to simulate the flow for both the experimental apparatus cited above and some proposed geometries to indicate how internal flow can be improved. Preliminary simulations have already shown that there is great gain by avoiding to place any coil at the impeller height.

1 Introduction

It is common to use either jackets or internal coils when the reaction inside stirred tank reactors is highly exothermic. Both arrangements have positive influence and drawbacks in controling the bulk temperature and they should be weighed carefully before deciding which arrangement should be chosen in any design. Reactor performance is greatly affected by the location of the internals and reactor mode of operation. Coiled vessels are even more affected because the coils drag the flow circulation. Important design parameters are coil helix and tube radius, as well as the number and location of coils. All these factors have an influence on the final flow and heat transfer inside the tank.

For laminar flows, when jacketed vessels are employed, there is a maximum of temperature inside the vessel at the centers of the recirculation zones of the secondary flow, since heat transfer in stirred tanks in these circumstances are dominated by the secondary flow. If coils are used, the temperature peak is not necessarily anymore at the center of the recirculation

The primary concern of this research is to show that there are mechanical limitations for flow circulation and heat transfer in the geometry suggested by Oldshue and Gretton [4]. Even though this computational work is only for laminar flow, the results for the flow can be extended to turbulent conditions because similar flow patterns are present for both laminar and turbulent conditions. The same mechanical limitations which are present for laminar flow are also present for turbulent flow. Therefore, studying the fluid circulation inside the coiled tank laminar flow will be of benefit for both flow regimes.

2 Modeling and simulation

The problem under investigation is three dimensional and can be for both Newtonian and non-Newtonian flow. For a preliminary investigation however, it will be considered a two-dimensional axi-symmetric model, even though the radial, axial and angular velocities will be determined on a two-dimensional grid, making this a pseudo tree-dimensional model.

The critical part and weakest link of the axi-symmetric model is the application of the boundary conditions for the impeller blades in order to give a reasonable representation of the blades effect. The approach used by Kuncewics [1] was adopted. This approach was followed by Nunhez and McGreavy [3, 7] and results show it gives a good representation for the flow patterns and serves as a basis for geometry selection which can be further refined at a later stage by a three dimensional model.

The governing equations for the axi-symmetric model are:

2.1 Momentum balance

radial

$$\rho\left(u_r\frac{\partial u_r}{\partial r}-\frac{{u_\theta}^2}{r}+u_z\frac{\partial u_r}{\partial z}\right)=\frac{1}{r}\frac{\partial}{\partial r}(r\sigma_{rr})-\frac{1}{r}\sigma_{\theta\theta}+\frac{\partial\sigma_{rz}}{\partial z} \tag{1}$$

angular

$$\rho\left(u_r\frac{\partial u_\theta}{\partial r}+\frac{u_r u_\theta}{r}+u_z\frac{\partial u_\theta}{\partial z}\right)=\frac{1}{r^2}\frac{\partial}{\partial r}(r^2\sigma_{r\theta})+\frac{\partial\sigma_{z\theta}}{\partial z} \tag{2}$$

axial

$$\rho\left(u_r\frac{\partial u_z}{\partial r}+u_z\frac{\partial u_z}{\partial z}\right)=\frac{1}{r}\frac{\partial}{\partial r}(r\sigma_{rz})+\frac{\partial\sigma_{zz}}{\partial z} \tag{3}$$

2.2 Mass conservation

$$\frac{1}{r}\frac{\partial}{\partial r}(\rho r u_r)+\frac{\partial}{\partial z}(\rho u_z)=0 \tag{4}$$

2.3 Energy conservation

$$\rho C_p\left(u_r\frac{\partial T}{\partial r}+u_z\frac{\partial T}{\partial z}\right)=\frac{1}{r}\frac{\partial}{\partial r}\left(k_l r\frac{\partial T}{\partial r}\right)+\frac{\partial}{\partial z}\left(k_l\frac{\partial T}{\partial z}\right)+\Delta H \tag{5}$$

The stress tensors are:

$$\sigma_{rr}=-p+2\mu\frac{\partial u_r}{\partial r} \tag{6}$$

$$\sigma_{\theta\theta}=-p+2\mu\frac{u_r}{\partial r} \tag{7}$$

The equations are solved numerically by the finite volume method and the simulations are performed using the CFX-4 package by AEA which has been successfully used for many flow problems. The boundary conditions are the same used by Street and McGreavy [6, 2] and Nunhez and McGreavy [3, 7].

3 Preliminary results and discussion

Preliminary results have already been obtained and show that there is great gain in modifying coils position inside the vessel and show it is benefitial to avoid placing any coil at the impeller height. This happens because if there are coils at this height, the average flow velocity is reduced when the fluid which leaves the impeller encounter the coils and, as a consequence of the velocity being reduced, there is a tendency of fluid stagnation between the coils and wall of the vessel. Figure 1 shows the velocity vector plot for an axial section of the reactor [1] for the experimental arrangement suggested by Oldshue and Gretton. As already commented, there is a limitation in the fluid circulation because the flow which is generated by the impeller encounters the coils which are present at the impeller blades height. As a consequence, those two coils drag the flow in the intire tank which, of course, impaire the flow in the tank. Figure 2 shows an arrangement having no coils at the impeller blades height. It is apparent from the figure that fluid circulation is greatly improved if the coils at the impeller region are removed. It is specially true for the circulation between the coils and the wall. The two figures are for the same angular velocity of the impeller of 30rpm.

In the actual stage, heat transfer and a non-Newtonian model have been introduced into the model. Reaction is considered as a source of heat in the bulk which has to be removed by either a jacket and/or coils. Several arrangements are being analysed to demonstrate how computational fluid dynamics can be used as a tool for reactor design.

At a later stage, a three dimensional and a turbulent model is aimed to be considered.

References

[1] C. Kuncewicz. Three-dimensional model of laminar liquid flow for paddle impellers and flat-blade turbines. *Chem. Eng. Sci.*, 47(15/16):3959–3967, 1992.

[2] J. R. Nunhez. *The Influence of geometric factors on the optimum design of stirred tank reactors.* PhD thesis, The University of Leeds, 1994. in preparation.

[3] J. R. Nunhez and C. McGreavy. A comparison of the heat transfer in helical coils and jacketed stirred tank reactors. *Brazilian Journal of Chemical Engineering*, 12(1), 1995.

[4] J. Y. Oldshue and A. T. Gretton. helical coil heat transfer in mixing vessels. *Chem. Eng. Progress*, 50(12):615 –621, 1954.

[5] D. A. Street. *Computational Modelling of Stirred Reaction Vessels.* PhD thesis, The University of Leeds, 1991.

[6] D. A. Street and C. McGreavy. A model of the heat transfer in internally cooled reaction vessels. In E. A. Foumeny and P. J. Heggs, editors, *Heat Exchange Engineering*, volume 2, pages 279–302. Ellis Horwood Ltd., 1991.

[7] G. Tatterson, editor. *Industrial Mixing Technology: Chemical and Biological Applications. Title of the Chapter: The Influence of Geometric Factors on The Optimum Design of Stirred Tank Reactors*, volume 89 of *AIChE Symposium Series.* AIChE, 1994.

[8] V. Uhl and Gray. *Mixing: theory and practice*, volume I. Academic Press, London, 1966.

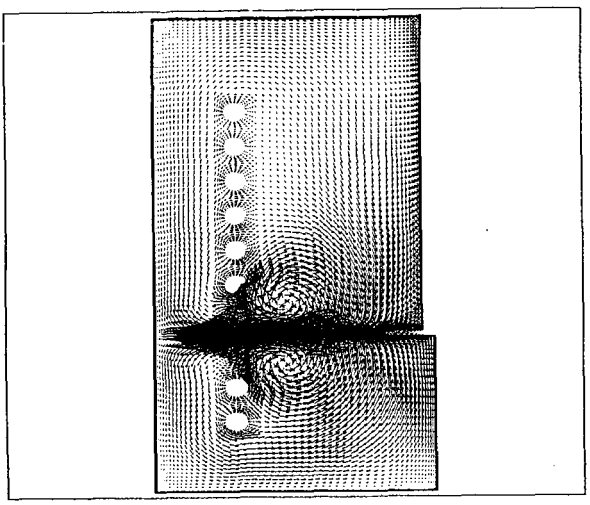

Figure 1: Experimental coiled arrangement by Oldshue and Gretton

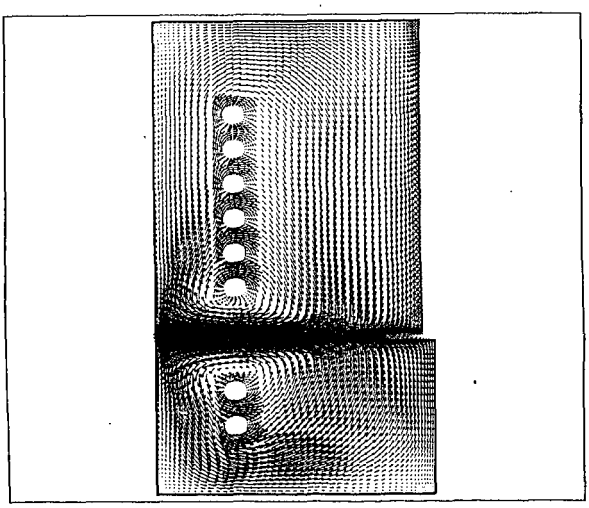

Figure 2: Alternative arrangement having no coils at the impeller height

THE CHARACTERIZATION OF RESIDUAL HYDROCARBON FRACTIONS WITH MODEL COMPOUNDS RETAINING THE ESSENTIAL INFORMATION

Giulia Bozzano, Mario Dente
Politecnico di Milano, CIIC Department, Piazza L. Da Vinci, 32, 20133 Milan, Italy - email: Mario.Dente@polimi.it

Marcos Sugaya
Petrobras S.A., Cenpes, Ilha do Fundao QD7, Rio de Janeiro 21910-900, Brazil

Colin McGreavy
The University of Leeds, Chemical Engineering Department, Leeds LS2 9JT, UK

KEYWORDS: Heavy residues characterization, model compounds, lumping

ABSTRACT

A characterization method for heavy residues is proposed. It has been specifically studied for the characterization of high molecular weight mixtures, with the aim of modeling thermal conversion processes such as thermal cracking, Eureka, visbreaking and delayed coking.
Only essential commonly available information is necessary. Extensive data based on the use of the Boduszynski-Altgelt methodology based on short-path molecular distillation (DISTACT), sequential elution fractionation technique (SEF) and vapor phase osmometry analyses (VPO), are surprisingly well reproduced. The results also match ^{1}H and ^{13}C NMR analyses. The proposed model is a valuable tool when complex and lengthy analyses are unavailable as is usually the case.

INTRODUCTION

The use of model compounds and mechanistic kinetic schemes has significantly improved the quality of product characterization when modeling the pyrolysis of high molecular weight mixtures.

Good characterization of the feed is crucial if reliable predictions of yield and quality of products based on mechanistic models are required. The availability of suitable data for heavy fractions is often a problem. In general, only a single density and average molecular weight (or kinematic viscosity) together with the initial boiling point range are available, while the whole distribution of these properties is actually required.

The higher the boiling point of a hydrocarbon fraction, the more difficult its characterization becomes. While the composition of naphthas can be determined, middle distillates can only be described in terms of their constituent groups and for heavy fractions the situation is far more complicated.

Since petroleum products are usually specified by their distillation properties, the boiling range often becomes more important than the actual molecular composition. Thermal cracking limits the cut points in commercial atmospheric and vacuum distillations to 350 and 540 C, respectively. In the laboratory, the use of high-vacuum short-path 'molecular' distillation (DISTACT) allows atmospheric equivalent boiling points (AEBP) of 700 C to be obtained.

Researchers often rely on solubility relations to characterize streams. These are arbitrary in the sense that the results depend on the solvents chosen, the temperatures, contact time, the relative quantities used in the treatment and on the agitation conditions, which results in obvious difficulties when comparing results of different scientists.

Distillation followed by a sequential elution fractionation (SEF) has been proposed by Boduszynski (1). This constitutes a better alternative because it avoids the problems derived from the strictly operational and therefore vague definition of asphaltenes, maltenes and resins (2).

Dente and Bozzano recently developed a global kinetic mechanism for visbreaking and delayed coking. A basic point of their activity has been the definition of model compounds in order to reduce the extremely large number of reactions and involved components in a sufficiently representative kinetic scheme. Using a combination of statistical methods, model compounds have been defined which give a good representation of the dominant phenomena involved.

Starting from the resulting distribution curves of the boiling point, kinematic viscosity or molecular weight, specific gravity and sulfur content, reactants and products can be lumped into a discrete number of pseudocomponents having fixed or varying properties. Alternatively, they can be represented as a mixture of model compounds (3).

METHOD

The feed (atmospheric and vacuum distillation residues) has been characterized by Dente and Bozzano (4) as a mixture of paraffinic, naphthenic and aromatic model compound. The relative amounts can be derived from the above mentioned macroscopic properties.

Once the total amounts of the three different classes of components have been estimated, it is possible to deduce the relative amounts of the pseudocomponents in the class. In fact, a careful elaboration of the data published in the literature (see, for instance, ref. 5), has shown that the statistical distribution of the single pseudocomponents with n_c carbon atoms (in every class) takes the form:

$$\frac{df}{dn_c} = k \exp\left[-k\left(n_c - n_{c\min}\right)\right] \qquad \textbf{Equation 1}$$

where k is obtained from the average number of carbon atoms of the distribution

$$k = \frac{1}{n_{c\,med} - n_{c\min}} \qquad \textbf{Equation 2}$$

where:

- f = fraction of the single component on the total of the class
- $n_{c,med}$ = average number of carbon atoms of the class
- $n_{c,min}$ = minimum number of carbon atoms of the class
- the index k depends on the class (paraffins, "aromatics", etc.) of components involved

The lumping rule typically groups 5 by 5 carbon atoms, from the minimum number to 58 carbon atoms; above this the splitting rule is 10 by 10 carbon atoms. For more than 98 carbon atoms an equivalent pseudocomponent is assumed to be representative of all the rest. A similar grouping rule can also be applied to the pyrolysis products. Of course, more complicated intrinsic rules are implied for multiple ring components (such as condensed rings polyaromatics and so on). The model compound characteristics can be summarized as follows:

- PAREQ - paraffin with 20% of methylation (i.e. 20% of carbon atoms is in a methyl group). The methylation degree has been deduced by assuming a prevalent polyisoprenoid structure for i-paraffins and a relative amount of n-paraffins into equivalent paraffinic pseudocomponent of about 20%.
- ARO0 - polyaromatic sheet with 50% of methylation at the boundaries and a single alkyl side chain with 20% of methylation. A distribution of all such possibilities includes a proportionality assumption between the molar fractions and the number of aromatic atoms in the molecules. The side chain size of this distribution is averaged and a single average aromatic molecule results which is defined solely by the number of carbon atoms. NMR data of some residues satisfactorily confirm the assumed methylation degree on the aromatic sheet boundary (typically in the range of 0.4-0.5). A direct proportionality between carbon atoms number and aromatic rings in the molecule is present.
- NAFTO0 - a polynaphthenic sheet with 50% of methylation at the boundaries and a single alkyl side chain with 20% of methylation. As in the case of aromatics, an internal distribution into the molecules is assumed. Contrary to the case of aromatic components, the major probabilities are in favor of structures with few rings and long side chains (as is possible to deduce from the API Research Project 60 where naphthenes contained in vacuum gasoil fractions extracted by chromatography are reported). There is, in consequence, an inverse proportionality between number of C atoms and number of rings in the molecule.

The relative amounts of paraffins, aromatics and naphthenes can be estimated from other feed properties and if the carbon distribution for each of the ARO0, NAFTO0 and PAREQ classes is known, the feed is completely characterized. The average number of carbon atoms of each compound class can be calculated to satisfy the global molecular weight and H/C relation. The minimum number of carbon atoms is calculated from the initial boiling point of the feed (Equation 3). For a given number of carbon atoms, the aromatic molecules will boil at higher temperatures than the paraffins, since their specific gravity is higher.

$$MW_{AEBP>500F} = 140 + 3.40x10^{-7}\frac{AEBP^3}{SPGR^{2.5}}$$

$$MW_{AEBP<500F} = MW_{AEBP>500F}\left[1 - 1.4x10^{-4}(600 - AEBP)\right] \qquad \textbf{Equation 3}$$

Partial volumes at 20 C can be calculated using the group contribution method of Hirsch (6). These have been adjusted to 15.5 C with the Rackett equation modified by Yamada and Gunn (7). The additive methods of Schroeder (8) and Le Bas (9), which give surprisingly good values for the molal volume of small hydrocarbon molecules at saturation temperature, show strong discrepancies when compared with the method of Hirsch, which has been developed for heavy fractions.

Dente and Bozzano (4) have pointed out the importance of performing corrections for sulfur before appropriate estimates of the content of paraffins, naphthenes and aromatics (and the H/C ratio) are possible. An equivalent hydrocarbon density is defined as

$$\rho_{eq} = \rho - 0.0066(S\%) \qquad \textbf{Equation 4}$$

RESULTS AND DISCUSSION

The predictions of the procedure are compared with experimental data (available only up to C_{17}) and (calculated) results from the API Research Project 44 (1972) (Figure 1). The agreement is good with the PAREQ curve fitting the data for paraffins fairly well and the ARO0 curve located somewhere between the paraffins and the pure aromatics compounds (the ARO0 compounds are alkyl substituted aromatics). The aromatic curve in Figure 1 results from applying the methodology described above for purely aromatic structures. In this case, the agreement can be seen to be also good.

In Figure 2, a comparison is made with experimental data for Kern River petroleum (2), which is a highly biodegraded crude. As can be seen, its constituents can be considered to be a mixture of paraffinic, naphthenic and aromatic model compounds up to 700 C, which is the current experimental limit. This figure also implies that fractions up to 400 C are mainly paraffinic.

The corresponding molecular weight distribution matches the experimental data of Boduszynski (10) remarkably well, as can be seen in figure 3. The actual matching can be even better than that presented here, since the molecular weight for the last fraction has been measured with vapor pressure osmometry (VPO) using two different solvents. While the results differ, the true MW for this fraction is probably lower than the value measured with the most efficient solvent shown in Figure 3.

Figure 4 presents the molecular weight distribution obtained for an atmospheric residue of an Arabian Heavy crude. The agreement between calculated and experimental results is also good.

Since equation 3 has been developed using a series of petroleum distillations, including Kern River and Arabian Heavy crudes (11,12), the agreement in AEBPs is implicitly good.

Table 1 provides a comparison in terms of some functional groups determined from ^1H and ^{13}C NMR analyses applied to a vacuum residue of Baiano petroleum (a light paraffinic crude).

CONCLUSIONS

The methodology described here gives a fairly good characterization of boiling points and molecular weights for residual fractions based on initial boiling point, sulfur content, average specific gravity and molecular weight (or kinematic viscosity).

The feed characterization predicted reproduces the results of NMR and VPO-DISTACT analyses and seems to constitute a viable route for investigating the composition of residual fractions. An important application would be in the modeling of typical resid upgrade processes such as visbreaking and delayed coking (13). In this case, a good definition of residence times for the liquid phase, where the most reactive components are concentrated is necessary.

Since the maximum temperature in these processes is around 500 C, fractions boiling above this will remain mainly in the liquid phase and precise definition of the true boiling point is not required.

Nevertheless, the molecular weight distribution (number of carbon atoms) is of great importance because it affects flash calculations, solubility relations (for precipitation of precursors in coking) and defines the system reaction state and residence time.

REFERENCES

1. Boduszynski M. M. Energy & Fuels 1987, 1, 2.
2. Altgelt K. H.; Boduszynski M. M. Comp. and Analysis of Heavy Petroleum Frac. 1994.
3. Astarita G.; Ocone R. Chemical Engineering Science 1992, 47, 2135.
4. Bozzano G. Tesi di dottorato in ingegneria chimica 1994, Politecnico di Milano.
5. Ali M. F.; Hasan M.; Bukhari A.; Saleem M. Oil & Gas Journal 1985, Aug.12, 71.
6. Hirsch E. Analytical Chemistry 1970, 42, 1326.
7. Yamada T.; Gunn R. D. J. Chem. Eng. Data 1973, 18, 234.
8. Partington J. An Adv. Treat. on Phys. Chem., V. 1, Fund. Princ.: The Prop. of Gases 1949.
9. Le Bas G. The Molecular Volumes of Liquid Chemical Compounds 1915.
10. Boduszynski M M. Energy & Fuels 1988, 2, 597.
11. Altgelt, K. H.; Boduszynski, M. M. Energy & Fuels 1992, 6, 68.
12. Altgelt, K. H.; Boduszynski, M. M. Energy & Fuels 1992, 6, 72.
13. Dente M.; Bozzano G.; Bussani G. Computers & Chem. Eng. 1997, 21, 1125.

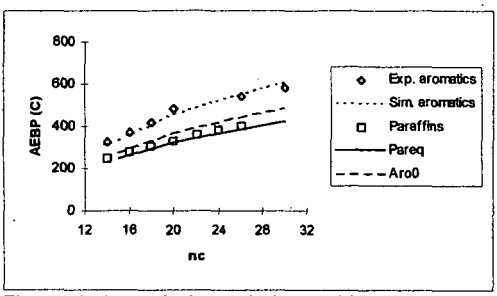

Figure 1 Atmospheric equivalent boiling points as a function of the number of carbon atoms for the model compounds of Dente and Bozzano (1994).

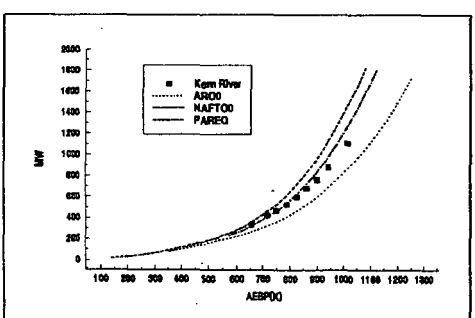

Figure 2 MW vs. AEBP representation of PAREQ/ARO0/NAFTO0 model compounds.

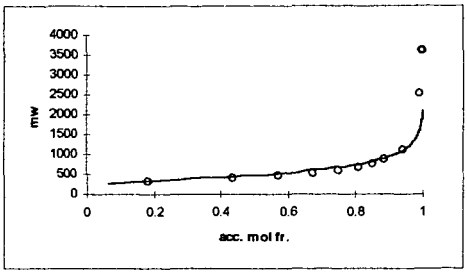

Figure 3 Molecular weight distribution for Kern River residue.

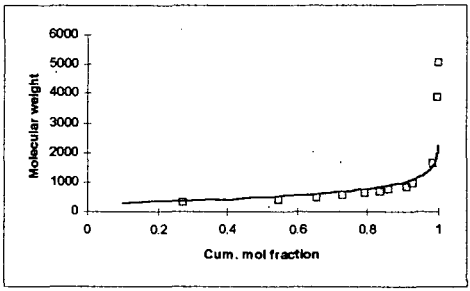

Figure 4 Molecular weight distribution for atmospheric residue of Arabian Heavy crude.

Table 1 Results for VR Baiano.

	Model	NMR data
H/C	1.89	1.80
C_{ar}	11.1	15.4
$C_{Ar,H}$	4.0	4.3
$C_{Ar,CH3}$	3.1	4.0
avg. size of side chains	22.2	26.5
C_{sat}	88.9	84.6
$(H/C)_{sat}$	2.05	2.02

CONTINUOUS-DISTRIBUTION KINETIC MODEL FOR MACROMOLECULAR CONVERSION: ASPHALTENE AND POLYMER

Yoichi Kodera, Yoshiki Sato, Tohru Kamo
National Inst. for Resources & Environment, AIST
16-3 Onogawa, Tsukuba, Ibaraki, 305-8569, Japan

KEYWORDS: continuous-distribution kinetics, asphaltene, polymer

ABSTRACT

One of the important purposes of macromolecular processing is to lower its molecular weight in cases of heavy oil processing or of feedstock recycling of plastic wastes. Molecular-weight distributions (MWDs) of macromolecular feedstocks and the reaction products at the early stage of conversion continuously span wide ranges of molecular weights. Continuous-distribution analysis is a convenient method to evaluate macromolecular conversion based on time-dependent changes of MWDs of reaction mixtures, which are readily monitored by HPLC-GPC. Kinetic models of macromolecular conversion are derived from simplified reaction schemes to interpret experimental results giving kinetic parameters, rate of conversion and activation energy. The kinetic modeling is useful to the evaluation of reaction conditions of processing regarding rate of conversion. In this presentation, kinetic models are proposed to interpret asphaltene hydrocracking and polymer degradation of polyolefin and phenolic (resole) resin. Details of experimental results will be discussed in the presentation.

INTRODUCTION

We have been studied asphaltene hydrocracking to improve heavy oil processing [1]. The similar experimental strategy is effective on phenolic resin degradation using tetralin or co-processed polystyrene acting as a hydrogen donor [2]. Kinetic models by continuous-distribution kinetics have been proposed In this presentation. Rate of reaction is defined as a rate of increase or decrease of molar concentration of chemical species. For macromolecules, the rate are given by moment method using time-dependent changes of MWDs. Mathematical model using continuous-distribution kinetics expresses macromolecular conversion by simplified schemes at the point of MW-lowering and is useful for evaluation of the reaction conditions.

Many kinetic models have been proposed based on lumping or continuous function of measurable properties. Rice-Herzfeld and the derived mechanism are quite useful for the kinetic analysis for petroleum processing. Recently, a general kinetic model for polymer degradation based on continuous-distribution kinetics using simplified schemes of radical mechanism was reported [3,4]. This model is illustrating kinetics of polymer (especially, polyolefin) degradation and polymerization based on reversible radical-chain reaction. However, reaction mechanism is sometimes different in the reaction of each substrate due to the nature of chemical structures. The major difference of kinetic models for each substrate are derived from the amounts of hydrocarbon chains which undergo β-scission promoting radical chain reaction. Such chain reaction have a minor role in the macromolecular conversion such as asphaltene hydrocracking and phenolic resin degradation. The absence of the radical chain reaction at thermal treatment is a general property of thermoset plastics.

We propose kinetic models for different types of macromolecular feedstocks, i.e., phenolic resin (resole resin) with aromatic matrix, polyolefins with linear main chains of hydrocarbons, and asphaltene with fused aromatics linked by hydrocarbon chains and hydrocarbon side-chains attached to the aromatic rings. For modeling such reactions, physical issues such as diffusion and vaporization sometimes have the significant effect in an individual reactor system. As a first step, we build general kinetic models regarding chemistry of macromolecules.

KINETIC MODEL

Continuous-distribution kinetics consists of two technique. One is simplified notation of reaction schemes and another is moment method for converting MWDs of GPC chromatograms into amounts of moments (e. g., first moment means molar concentration). In the simplified schemes, some lumped groups of chemical species are chosen to examine the changes of amounts of moments in the function of time. A lumped group is a group of compounds which behave in the similar manner chemically and those compounds should be analytically distinguished from the other groups. For example, asphaltene from Arabian Light consists of

two types of chemical moieties, fused aromatics and hydrocarbon chains attached to the fused rings. Asphaltene hydrocracking gives asphaltene component with the lower MWs and aliphatic hydrocarbon as the major products. What we want to examine is the quantity of asphaltene component. Then, asphaltene and aliphatic hydrocarbons are the two chemical species to be described in the reaction schemes. For polyolefin degradation, chain-scission occurs along the main chain to give monomer, dimer, trimer, and oligomers. Any polymer gives oligomers via random chain-scission and some polymers gives some specific products (monomer, dimer, and trimer) in high yields by specific chain-scission following to random-chain scission. Phenolic resin degradation gives only random chain-scission products. Phenols are given by the results of the random chain-scission not the reaction via β-scission or chain-end scission as found in polyolefin degradation.

General notation. Rice-Herzfeld and related mechanism gave the following steps as the major radical reactions of hydrocarbons in petroleum processing. In continuous-distribution kinetics, each reaction is described as follows:

1. initiation (radical formation) of polymer P(x) with an arbitrary MW of x.

$$P(x) \longrightarrow R(x') + R(x-x')$$

This step always gives end-radical, which has a radical center at the chain-end. The other path to form radical is radical-promoted intermolecular hydrogen-abstraction below.

2. termination (radical stabilization)

radical coupling $R(x) + R(x+x') \longrightarrow P(x-x')$

disproportionation $R(x) + R(x') \longrightarrow S(x+x')$: initial addition to form activated complex

$S(x+x') \longrightarrow P(x) + Q(x')$: paraffin (P) and olefin (Q) formation

Initiation and termination step have negligible contribution to the increase of molar concentration because the major contribution is given by β-scission and intermolecular hydrogen-abstraction, which are the main route of radical chain reaction increasing molar concentration of the products. This concept (Long Chain Assumption) is valid only for polyolefin degradation and aliphatic components in asphaltene hydrocracking and not valid for phenolic and asphaltene components.

3. intramolecular hydrogen-abstraction by Rice-Kossiakoff mechanism (this is called as back-biting reaction in polymer chemistry)

$Re(x) \longrightarrow Rs(x)$: formation of specific radical Rs with a radical center near chain-end from chain-end radical Re.

$Rs(x) \longrightarrow Ps(x_S) + Q(x-x_S)$ or $Qs(x_S) + P(x-x_S)$: formation of paraffin and olefin, one of them is a specific product.

This step is important step for the formation of specific products. End-radical is unstable to abstract a hydrogen at around fifth carbon via cyclic transition state. The resulting radical then undergo β-scission to give specific products, dimer or trimer.

4. Intermolecular hydrogen-abstraction

$$R(x) + P(x') \longrightarrow S(x+x')$$

$$S(x+x') \longrightarrow P(x) + Rr(x')$$

Radical also promotes intermolecular hydrogen-abstraction. This gives mostly random radical Rr(x), where radical center randomly distributes along a main chain. β-Scission of random radical gives the corresponding olefin and chain-end radical of random MWs.

5. Radical addition to olefins

$$R(x) + Q(x') \longrightarrow R(x+x')$$

When olefin are abundant in a reaction, radical addition is important. Some researchers report the importance of addition in liquid phase compared with that in vapor phase [5]. Using this scheme, it is possible to describe simple kinetics of polymerization [3].

Catalytic reaction involves some different mechanisms such as alkyl-group transfer and cyclization of olefin to form aromatics. These have no big change in MWs. However, one may describe lumped groups in schemes when the chemical species plays important role in the chemical or physical properties one interested in at the processing.

Asphaltene hydrocracking. In asphaltene hydrocracking, the conversion is evaluated at the point that decreasing rate of asphaltene component A(x). The simplified schemes shown in Schemes (A, B, C) are for the evaluation under the experimental conditions with no coking and enough supply of hydrogen[1]. Random bond-scission is assumed for the cleavage of linkages between fused-ring units (Scheme (A)), the side-chain cleavage from a fused ring (Scheme (B)), and bond-scission of aliphatic hydrocarbons (Scheme (C)) because of the possible random-distribution features of MWDs of fused-rings and linkages. Each component A(x) and P(x) separate by precipitation with hexane and is analyzed by GPC.

$$A(x) \underset{k_A}{\overset{k_a}{\rightleftharpoons}} A(x') + A(x-x') \quad (A)$$

$$A(x) \underset{k_B}{\overset{k_b}{\rightleftharpoons}} P(x') + A(x-x') \quad (B)$$

$$P(x) \underset{k_R}{\overset{k_r}{\rightleftharpoons}} P(x') + P(x-x') \quad (C)$$

Polyolefin degradation is expressed as Scheme (C) due to the absence of A(x) and phenolic resin degradation is expressed as scheme (A) because of the negligible contribution of hydrocarbon linkage to the overall degradation. The detailed kinetic model for polyolefin degradation was reported in ref. [3], where reversible radical mechanism is considered.

Phenolic resin degradation. Presence of a hydrogen donor in phenolic resin degradation is the essential factor to proceed the degradation. One may need to know the effect of hydrogen source. The schemes including radicals are required to describe the interaction between radical intermediates and hydrogen source. Phenolic resin degradation is described as follows:

$$A(x) \underset{k_R}{\overset{k_r}{\rightleftharpoons}} R(x') \quad (D)$$

$$R(x) + A(x') \underset{k_A}{\overset{k_a}{\rightleftharpoons}} R(x+x') \quad (E)$$

where phenolic resin is A(x) and radical is R(x).
Scheme (D) expresses radical formation (k_r) and stabilization (k_R). Radical formation is given by Scheme (F) and stabilization is a simplified scheme of the bimolecular reactions of a radical with a hydrogen donor such as tetralin T in Schemes (G) and (H) under the assumption of quasi-stationary state of radical [3].

$$A(x) \longrightarrow R(x') + R(x-x') \quad (F)$$

$$R(x) + T(x_t) \rightleftharpoons S(x+x_t) \quad (G)$$

$$S(x+x_t) \longrightarrow A(x) + N(x_n) \quad (H)$$

Another radical formation is radical-promoted intermoleculer hydrogen-abstraction, which have no contribution to the increase of concentration of radical and it is a competitive reaction to radical addition to aromatic rings. It is a determining factor to characterize phenolic resin degradation from polyolefin degradation that the resulting radical given by the hydrogen-abstraction is not expected to proceed radical chain reaction giving olefin and another radical due to the aromatic structure.

Schemes (D) and (E) gives integro-differential equations (1) and (2) according to continuous-distribution kinetics.

$$\partial a/\partial t = - k_r\, a(x) + k_R\, r(x) - k_a\, a(x) \int_0^\infty r(x')\, dx' + k_A \int_x^\infty r(x')\, \Omega(x,x')\, dx' \quad (1)$$

$$\partial r/\partial t = k_r\, a(x) - k_R\, r(x) - k_a\, r(x) \int_0^\infty a(x')\, dx' + k_a \int_0^\infty a(x')\, r(x-x')\, dx' + k_A \int_x^\infty r(x')\, \Omega(x,x')\, dx' - k_A\, r(x) \quad (2)$$

Applying the moment operation (McCoy [6], McCoy and Wang [7]), $\int_x^\infty [\,]\, x^n\, dx$, to the integro-differential equations (1) and (2) yield

$$da^{(n)}/dt = - k_r\, a^{(n)} + k_R\, r^{(n)} - k_a\, a^{(n)}\, r^{(0)} + k_A\, Z_{n0}\, r^{(n)} \quad (3)$$

$$dr^{(n)}/dt = k_r\, a^{(n)} - k_R\, r^{(n)} + k_a \left[\sum_{j=0}^{n} \binom{n}{j} a^{(j)}\, r^{(n-j)} - a^{(0)}\, r^{(n)}\right] + k_A\, r^{(n)}\, (Z_{n0} + 1) \quad (4)$$

where $Z_{n0} = 1$, 1/2, or 1/3 for $n = 0$, 1, or 2.
Zeroth moments (n=0) are governed by the differential equations (5) and (6),

$$da^{(0)}/dt = - k_r\, a^{(0)} + k_R\, r^{(0)} - k_a\, a^{(0)}\, r^{(0)} + k_A\, r^{(0)} \quad (5)$$

$$dr^{(0)}/dt = k_r\, a^{(0)} - k_R\, r^{(0)} \quad (6)$$

Applying quasi-stationary state assumption (QSSA) of radical $dr^{(0)}/dt \approx 0$ to equation (6) gives

$$r^{(0)} = (k_r / k_R)\, a^{(0)} \tag{7}$$

Then,

$$da^{(0)}/dt = (k_A - k_a\, a^{(0)})\, (k_r / k_R)\, a^{(0)} \tag{8}$$

Integration of equation (5) with the initial condition $a^{(0)}(t=0) = a_o^{(0)}$ gives

$$a^{(0)} = \exp[(k_A\, k_r / k_R)\, t] \,/\, \{1/a_o^{(0)} + (k_a/k_A)\, [\exp[(k_A\, k_r / k_R)\, t] - 1]\} \tag{9}$$

$$a^{(0)}(t \to \infty) = k_A/k_a$$

First moments (n=1) are given as follows:

$$da^{(1)}/dt = -\, k_r\, a^{(1)} + k_R\, r^{(1)} - k_a\, a^{(1)}\, r^{(0)} + (k_A/2)\, r^{(1)} \tag{10}$$

$$dr^{(1)}/dt = k_r\, a^{(1)} - k_R\, r^{(1)} + k_a\, a^{(1)}\, r^{(0)} - (k_A/2)\, r^{(1)} \tag{11}$$

The summation of first moments for polymer and radical gives

$$d[a^{(1)} + r^{(1)}]/dt = 0 \tag{12}$$

confirming the conservation of reactant polymer mass.

This is a kinetic model for resole resin in solution. Phenolic resin is its cured form with filler and other additives. Solubility of phenolic resin provide the interesting physical issues to the modeling, which will be examined in the near future.

EXPERIMENTAL TREATMENTS FOR THE KINETICS

Sample preparation. Macromolecular substrates for kinetic analysis has to have a smooth distribution of MWDs because of the overlap of reaction products with the original peaks. Typically, an original resole resin contains some low MW components, which are easily removed by reprecipitation with THF and hexane. After resole resin was dissolved with THF, hexane was added with stirring. Low MW components in THF/hexane were readily removed by decantation. The residual solvent was evaporated under reduced pressure to give resole resin to be used in experiments (Fig. 1). The similar pretreatment is required in some polymers such as polystyrene.

Analysis. HPLC-GPC is a major apparatus to determine MWDs of reaction mixtures in this kinetics. Light scattering measurement or GC are alternative methods depending on the properties of substrates. MWDs thus obtained are converted into the corresponding amounts of moments. Mass of chemical species versus retention time of a chromatogram is calculated to give moments defined as equation (13).

$$m^{(n)} = \int_0^\infty x^n\, m(x)\, dx \tag{13}$$

where m(x) is molar concentration of component m in the MW range of [x, x + dx]. In GPC chromatogram using a refractive index detector have coordinates of mass concentration as intensity and retention time giving MWs. Different types of chemical species gives different intensity even if they have the same mass concentration whereas the similar chemical species of the same mass concentration gives the same peak area. For example, polystyrene samples of different MWs gives the same peak area if they are the same concentration whereas 1 g/L polystyrene and 1 g/L polyethylene give different peak area depending their refractive index. In product analysis of asphaltene hydrocracking, separate analysis is required for asphaltene components and aliphatic hydrocarbons. Asphaltene is defined as a hexane(or heptane)-insoluble component and, actually, the most parts of chemical species which have asphaltene structure do not dissolve in reaction mixtures after precipitation with hexane or heptane. Asphaltene components are analyzed by using the precipitation. MWDs of another products (aliphatic hydrocarbons) are obtained by subtracting MWDs of asphaltene components from MWDs of reaction mixtures.

Careful treatment is required to evaluate experimental results of macromolecular conversion by comparing them with a kinetic model. Some MW-standards such as asphaltene and phenolic resin are not available. Especially, it is impossible to obtain absolute MWs of asphaltene even by light scattering method due to its color. Then, molar concentration of a substrate does not change linearly with time despite to linear relation of kinetic discussion. However, we can still get the reaction rate, i.e. slope of the line, at the very early periods of the conversion and can compare the rates at different reaction conditions.

CONCLUSION

Kinetic models by continuous-distribution kinetics for asphaltene hydrocraking, phenolic resin degradation, olefin degradation were discussed. The kinetic treatment using time-dependent changes of MWDs of reaction mixtures provide a convenient method to evaluate macromolecular conversion. Depending the nature of a macromolecule, reaction schemes should be selected carefully.

REFERENCES

[1] Y. Kodera, et al., Preprints of International Conference on Refinery Processes, AIChE Spring Meeting, New Orleans, March 1998, p. 321. In preparation for submission.

[2] Sato, Y., Kodera, Y., Kamo, Y., Matsumoto, T., 7th EPF Symposium on Polymeric Materials, European Polymer Federation/Polish Chemical Society, Poland, Sept. 21, 1998. (scheduled).

[3] Kodera, Y., McCoy, B. J., *AIChE J.*, 1997, 43, 3205.

[4] Kodera, Y., Cha, W. S., McCoy, B. J., *Prep. Div. Fuel Chem., ACS*, 1997, 42, 1003.

[5] Wu, G. Katsumura, Y., Matsuura, C., Ishigure, K., Kubo, J., *Ind. Eng. Chem. Res.*, 1996, 35, 4747.

[6] McCoy, B. J., *AIChE J.*, 1993, 39, 1827.

[7] McCoy, B. J., Wang, M., *Chem. Eng. Science*, 1994, 49, 3773.

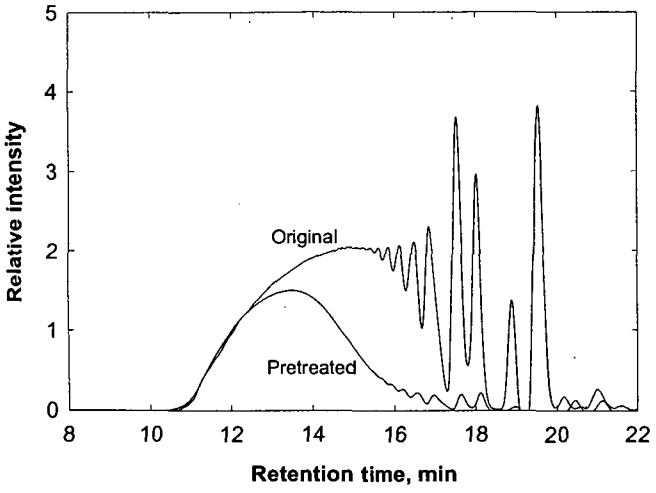

Figure 1.- **RI chromatogram of resole resin before and after pretreatment**
GPC analysis was performed with a HPLC (Shimadzu LC-9A pump, RID-6A RI detector) using Polymer Laboratories GPC columns (50x7.5 mm-guard column and two 300x7.5 mm columns of 3μm-Mixed E) at 40 °C. THF was used as an eluent at flow rate of 1.0 mL/min.

HYDRODESULFURIZATION OF A VACUUM GAS OIL IN A SLURRY BED AND IN A TRICKLE-BED REACTOR: A COMPARATIVE STUDY

C.G. Yiokari and C.G. Vayenas
Department of Chemical Engineering
University of Patras
26500 Rio, Patra Greece

KEYWORDS: Trickle-Bed Reactors, Hydrodesulfurization, Wetting Efficiency

INTRODUCTION

Partial wetting of catalyst pellets is an important characteristic of trickle-bed reactors (Satterfield, 1975; Herskowitz and Smith, 1983; Gianetto and Specchia, 1992). Two kinds of wetting must be considered for porous catalysts, internal wetting, defined as the ratio between the wetted pellet volume and the total pellet volume and external effective wetting that is the fraction of the external area of the pellet effectively wetted. Many investigations have dealt mostly with external wetting efficiency by tracer (Mills and Dudukovic, 1981) and reaction (Herskowitz et. al., 1979; Ring and Missen, 1989; Morita and Smith, 1978) methods and by computational simulations (Ring and Missen, 1986; Yentekakis and Vayenas, 1987). Total internal wetting of the catalyst pellets is normally assumed due to capillary effects.

With the exception of few studies aiming at the determination of catalyst wetting under industrial reaction conditions (Ruecker and Akgerman, 1987; Ring and Missen, 1989; Al-Dahhan and Dudukovic, 1995), reaction methods used have determined wetting efficiencies at low pressures and temperatures (Herskowitz et al., 1979; Morita and Smith, 1978).

In this investigation effective catalyst wetting was estimated for a trickle-bed reactor for the HDS of a vacuum gas oil at high pressure (60atm) and temperatures (280-330°C). The wetting efficiencies were accounted for by expressing the global rate in terms of an overall effectiveness factor, which is a function of internal and external wetting efficiencies, internal diffusion and intrinsic kinetics. External mass and heat transfer limitations were negligible. The modified Thiele modulus proposed by Dudukovic was used and intrinsic kinetics were determined by batch experiments.

EXPERIMENTAL

The 15%MoO_3-4.5%NiO/γ-Al_2O_3 catalyst was prepared by incipient wetness co-impregnation of 1/16" γ-Al_2O_3 extrudates with the appropriate solutions. The catalyst was calcined at 110°C overnight and at 500°C for 5h. The presulfidation of the catalyst was accomplished by exposure to a H_2S/H_2 mixture at 360°C, preceded and followed by a 1h He purge. The presulfation time was adjusted accordingly so that the total amount of H_2S passed over the catalyst contained approximately 6 times more sulfur than the stoichiometric amount needed for the sulfidation of the Mo, Ni oxides. The feedstock used was a vacuum distillate obtained from the refinery of LPC Hellas with a total sulfur content of 0.45% wt. The density of the lube oil was 0.86 g/ml at 20°C, the kinematic viscosity at 40 and 100°C was 39 and 6.14cSt respectively giving a viscosity index of 103. The sulfur content of the feed and product oils were determined by an ASOMA sulfur analyzer (200T-series) based on X-ray fluorescence analysis.

The HDS of the vacuum gas oil was carried out in both a stirred batch autoclave and a concurrent downflow trickle-bed reactor. The batch autoclave had a volume of 300ml and the catalyst to oil mass ratio was equal to 1/10. The reactor operating time was counted from the moment the temperature of the reactor reached the desired value and the pressure was fixed at 880psi (≈60atm). A more detailed description of the setup and performance of the batch reactor is given elsewhere (Yiokari et al., 1997). The trickle-bed reactor was a stainless steel tube of 15mm i.d. and 300mm length arranged inside a heater. The 15ml catalyst bed was placed at the bottom of the reactor while the rest of the tube was filled with γ-Al_2O_3 extrudates. The flow rates of the gases were controlled by mass flowmeters and controllers. The viscous liquid feed, which was placed in a piston, was driven into the reactor by pumping distilled water into the other side of the piston with the help of a common HPLC pump. The reactants, both liquid and gas, were mixed and heated before entering the reactor at 150°C. The reactor effluent flowed into a stainless steel cylinder acting as a gas-liquid separator. The liquid product flowed continuously into a sample tank with the help of a solenoid valve whereas the scrubbed gas product flowed into the vent. Control for the pressure and temperature of the catalyst bed were provided. All results were obtained under steady state conditions which were reached approximately 4h after the reaction conditions were applied. According to the work of Fukushima and Kusaka (1977a,b) regarding the boundaries of hydrodynamic flow regions, the range of Reynolds numbers experimentally covered in this work belonged to the trickle flow region ($1\times10^{-4}<Re_L<1.5\times10^{-3}$).

RESULTS

Hydrodesulfurization Kinetics: One of the most important set of reactions that take place during the hydrotreatment of residual oils is the hydrodesulfurization (HDS) of its various sulfur compounds. Since there is a great number of different sulfur compounds in industrial feedstocks, the actual mechanism of the HDS reaction is quite complex. Kinetic studies have shown that the HDS of an industrial feedstock could be described satisfactorily if it is considered as a mixture of two sulfur containing pseudocompounds, which differ considerably in HDS reactivity (Schuit and Gates, 1973). The first pseudocompound represents a reactive group that consists of thionaphthenes, mercaptans and sulfides (S_1), while the second hypothetical compound consist of the less reactive thiophenoaromatics (S_2). Each pseudocompound is assumed to react at a rate proportional to its sulfur concentration. Therefore the HDS reactions can be written simply,

$$S_1 + H_2 \xrightarrow{r_1} \text{products} \qquad \text{and} \qquad S_2 + H_2 \xrightarrow{r_2} \text{products} \tag{1}$$

Gel permeation chromatography of the gas oil (Varotsis and Pasadakis, 1997) used in this investigation determined 40% of sulfur pertaining to the less reactive thiophenoaromatics (S_2). Hence the remaining 60% of the gas oil total sulfur content was assumed to be the more reactive pseudocomponent S_1. The two straight lines illustrated in Figure 1 indicate first order reaction of each sulfur containing pseudocomponent adding up to the curve fitting the data. This type of kinetic behavior can be mistaken for second order reaction kinetics. The distinction between the two parallel first order reactions and one second order reaction was made according to the procedure proposed by Wei and Hung (1974) for sulfur conversions above 97%.

Schuit and Gates (1973) reported that the kinetics regarding hydrogen are dependent on catalyst composition and on the nature of the feedstock. Hence the effect of hydrogen partial pressure on the HDS reaction was investigated. Figure 2 shows that sulfur conversion practically remains constant for hydrogen partial pressures over 20atm, independent of total gas flow rate. Thus the experiments performed in this study were in the region of zero-order kinetics regarding hydrogen.

Assumptions: The absence of external mass and heat transfer limitations was verified in the batch autoclave by choosing the appropriate stirring speed and in the trickle-bed reactor by confirming that the sulfur conversion remained constant when the volume of the catalyst bed and liquid flow rate where both doubled (constant LHSV). The 1/16" diameter pellets assured no internal mass and heat transfer by performing batch experiments with pellets of different sizes. First-order isothermal, irreversible reactions with respect to the reactants in the liquid are considered and the gaseous H_2 is present in great excess so the liquid is always saturated with gas. The catalyst pellets are completely wetted in the batch autoclave. Under these conditions the rate constants derived from the batch autoclave are assumed to be intrinsic rate constants.

Batch Reactor Performance: In the case of the batch reactor, one has:

$$\frac{dC_{S,i}}{dt} = \left(\frac{v_{cat}}{v_{liq} + v_{cat}}\right) \cdot r_i \tag{2}$$

where r_i is the reaction rate and $C_{S,i}$ the concentration of the sulfur-containing pseudocomponent i and v_{cat} and v_{liq} are the volume of the catalyst bed and the extra liquid in the batch autoclave respectively. For first order reaction regarding the sulfur component and zero order reaction regarding H_2, one has:

$$r_i = k_{B,i} \cdot C_{S,i} \tag{3}$$

where $k_{B,i}$ is the rate constant of the sulfur containing pseudocomponent i. Substituting equation (3) in equation (2) and integrating, one obtains:

$$C_{S,i} = C_{S0,i} \cdot \exp\left(-\frac{k_{B,i}}{ELHSV}\right) \tag{4}$$

where ELHSV is an equivalent liquid hourly space velocity and can be defined for the batch autoclave as:

$$ELHSV^{-1} = \left(\frac{v_{cat}}{v_{liq} + v_{cat}}\right) \cdot t \tag{5}$$

Therefore the total sulfur concentration is:

$$C_S = C_{S,1} + C_{S,2} \Leftrightarrow \frac{C_S}{C_{S0}} = \alpha_1 \cdot \exp\left(-\frac{k_{B,1}}{ELHSV}\right) + \alpha_2 \cdot \exp\left(-\frac{k_{B,2}}{ELHSV}\right) \tag{6}$$

where α_1 and α_2 express the percentage of the pseudocompounds S_1 and S_2 and depend on the feedstock used. In this study α_1 and α_2 are 0.6 and 0.4 respectively as discussed above.

Trickle-bed Reactor Performance: Considering a differential volume element across the reactor, one has:

$$F \cdot C_{S0,i} \cdot dx_S = r_i \cdot dV \tag{7}$$

where F is the liquid flow rate, x_S is the sulfur conversion and V is the volume of the catalyst bed. Considering first order reaction regarding the sulfur component and zero order reaction regarding H_2 we substitute equation (3) in equation (7) to obtain:

$$C_{S,i} = C_{S0,i} \cdot \exp\left(-\frac{k_{T,i}}{LHSV}\right) \quad (8)$$

where LHSV is the liquid hourly space velocity and is defined for the trickle-bed reactor as:

$$LHSV^{-1} = \frac{V}{F} \quad (9)$$

and $k_{T,i}$, i=1,2, are the apparent first order kinetic constants for trickle-bed operation. Therefore the total sulfur concentration for the trickle-bed reactor is:

$$C_S = C_{S,1} + C_{S,2} \Leftrightarrow \frac{C_S}{C_{S0}} = \alpha_1 \cdot \exp\left(-\frac{k_{T,1}}{LHSV}\right) + \alpha_2 \cdot \exp\left(-\frac{k_{T,2}}{LHSV}\right) \quad (10)$$

Figures 3 and 4 illustrate the kinetic behavior of the batch and trickle-bed reactors, for the four temperatures studied, respectively. As expected sulfur concentration decreases with increasing $LHSV^{-1}$ and temperature. The total gas flow rate for the trickle-bed reactor is equal to 200ml/min. The removal of sulfur from the vacuum gas oil is greater in the batch reactor for given reaction conditions. The values of the rate constants derived for both the batch autoclave and the trickle-bed reactor are summarized in Table 1. The rate constants of group S_1 are 5-35 times greater than those of group S_2 depending on the reaction temperature. It is important to note that the ratios $k_{T,1}/k_{B,1}$ and $k_{T,2}/k_{B,2}$ remain practically constant with temperature and that the latter is larger since it corresponds to the slower reaction.

DISCUSSION

In the absence of mass transfer effects one would expect that the rate constants derived from equation (10), $k_{B,i}$, would be equal to the ones derived from equation (6), $k_{T,i}$, but this is not the case (Table 1). The essential difference of the two reactors is illustrated in Figure 5, where one can see that the rate of the HDS reactions is affected only by the partial wetting of the catalyst in the case of the trickle-bed reactor since other factors which affect it are the same (hydrogen excess, feed, etc.) and internal and external mass and heat transport limitations are negligible.

For a non ideal trickle-bed reactor, equation (10) can be written again by substituting $k_{T,i}$ with $(k_{B,i} \cdot \eta_{T,i})$, as:

$$\frac{C_S}{C_{S0}} = \alpha_1 \cdot \exp\left(-\frac{k_{B,1} \cdot \eta_{T,1}}{LHSV}\right) + \alpha_2 \cdot \exp\left(-\frac{k_{B,2} \cdot \eta_{T,2}}{LHSV}\right) \quad (11)$$

where $\eta_{T,i}$, i=1,2 are overall catalyst effectiveness factors for trickle-bed reactor for reactions (1). Therefore $k_{T,i}/k_{B,i}$ is equal to $\eta_{T,i}$ (i = 1,2).

For particles of irregular shape and in two-phase systems, it has been established by Aris (1957) that the effectiveness factor can be approximated by:

$$\eta_i = \frac{\tanh\Phi_i}{\Phi_i} \quad (12)$$

where

$$\Phi_i = \frac{V_p}{S}\sqrt{\frac{k_{B,i}}{D_{eff,i}}} \quad (13)$$

V_p is the catalyst volume, S is the catalyst external surface and $D_{eff,i}$ is the diffusivity of pseudocomponent i. Diffusivities of the sulfur-containing pseudocompounds were calculated using the Wilke-Chang correlation with Vs_1=80.8 cm^3/mole and Vs_2=190 cm^3/mole (Reid et al., 1977). Effective diffusivities were computed assuming a porosity/tortuosity factor of 0.1 (Yitzhaki and Aharoni, 1977). The dynamic viscosity of the lube oil at a given temperature was calculated by multiplying the kinematic viscosity with the density of the lube oil at that temperature. The variances of density and dynamic viscosity with temperature were calculated with the Watson-Gamson and Guzman-Andrade equations respectively.

To account for the partial external wetting of the catalyst particles one can use the modified Thiele modulus for trickle-bed reactors proposed by Dudukovic (1977). This modulus is based on the effective wetted external area, S_{eff}, and wetted internal volume of the pellet, $V_{p,eff}$, and can be written as:

$$\Phi_{T,i} = \frac{V_{p,eff}}{S_{eff}} \cdot \sqrt{\frac{k_{B,i}}{D_{eff,i}}} \Rightarrow \Phi_{T,i} = \frac{f_{int}}{f_{ext}} \cdot \Phi_i \quad (14)$$

where f_{int} and f_{ext} are the internal and external wetting efficiencies respectively, defined as:

$$f_{int} = \frac{V_{p,eff}}{V_p} \qquad \text{and} \qquad f_{ext} = \frac{S_{eff}}{S_p} \quad (15)$$

From the values of the overall catalyst effectiveness factors $\eta_{T,i}$ (Table 1) and equation (12) the Thiele modulus of the trickle-bed reactor, $\Phi_{T,i}$, (Table 2) is calculated. Using equation (13) we compute Φ_i (Table 2). Therefore from equation (14) the ratio f_{int}/f_{ext} is calculated and is summarized for the four temperatures studied and for the two sulfur pseudocomponents in Table 2. Total internal wetting of the catalysts pellets is normally assumed due to capillary effects, hence f_{int} could be considered unity and the external wetting efficiencies are estimated and presented in

Table 2. The computed values of the external wetting efficiencies slightly decrease with decreasing temperature. It is reassuring that similar values are extracted from both pseudocompounds for the proceding analysis. The mean values are 0.45 and 0.39 for pseudocomponents S_1 and S_2 respectively. These values of wetting efficiency are somehow smaller than the ones usually reported in the past (Satterield, 1975; Gianetto and Specchia, 1992). This could be related to the low liquid flow rates used in the present investigation.

CONCLUSIONS

The HDS kinetics of an industrial feedstock were studied in the temperature range of 280-330°C in both a stirred batch autoclave and a trickle-bed reactor. The feed was considered as a mixture of two sulfur containing groups each reacting according to first order kinetics regarding their sulfur content. Reaction kinetics for hydrogen were zero order in the region of the present investigation.

The rate constants derived from the trickle-bed reactor are smaller than the ones obtained from the batch autoclave. The latter must correspond to intrinsic kinetic constants since internal and external mass and heat limitations were absent and total catalyst wetting was attained. The ratio of the rate constants extracted from the batch autoclave and trickle-bed experiments can be used to estimate the effectiveness factors during trickle-bed operation and thus also estimate the wetting efficiency under reaction conditions.

REFERENCES

Al-Dahhan, M.H. and Dudukovic, M.P., 1995, *Chem. Eng. Sci.* **50**, 2377.
Aris, R., 1957, *Chem. Eng. Sci.* **6**, 262.
Dudukovic, M.P., 1977, *A.I.Ch.E. J.* **23**, 940.
Fukushima, S., and Kusaka, K., 1977, *J. Chem. Eng. Jpn.* **10**, 461.
Fukushima, S., and Kusaka, K., 1977, *J. Chem. Eng. Jpn.* **10**, 468.
Gianetto, A., and Specchia V., 1992, *Chem. Eng. Sci.* **47**, 3197.
Herskowitz, M., Carbonell, R.G., and Smith, J.M., 1979, *A.I.Ch.E. J.* **25**, 272.
Herskowitz, M., and Smith, J.M., 1983, *A.I.Ch.E. J.* **29**, 1.
Llano, J.J., Rosal, R., Sastre, H., and Diez, F.V., 1997, *Ind. Eng. Chem. Res.* **36**, 2616.
Mills, P.L. and Dudukovic, M.P., 1981, *A.I.Ch.E. J.*, **27**, 893.
Morita, S., and Smith J.M., 1983, *Ind. Eng. Chem. Fundam.* **17**, 113.
Reid, R.C., Prausnitz, J.M. and Sherwood, T.K., 1977, *The Properties of Gases and Liquids*, 3rd edn. McGraw-Hill, New York.
Ring, Z.E., and Missen, R.W., 1986, *Can. J. Chem. Eng.* **64**, 117.
Ring, Z.E., and Missen, R.W., 1989, *A.I.Ch.E. J.* **35**, 1820.
Ruecker C.M., and Akgerman, A., 1987, *Ind. Eng. Chem. Res.* **26**, 164.
Satterfield, C.N., 1975, *A.I.Ch.E. J.* **21**, 209.
Schuit, G.C.A. and Gates, B.C., 1973, *A.I.Ch.E. J.* **19**, 417.
Varotsis, N., and Pasadakis, N., 1997, *Ind. Eng. Chem. Res.* **36**, 5519.
Wei, J., and Hung, C.W., 1980, *Ind. Eng. Chem. Process Des. Dev.* **19**, 197.
Yentekakis, I.V. and Vayenas, C.G., 1987, *Chem. Eng. Sci.* **42**, 1323.
Yiokari, C., Morphi, S, Siokou, A., Satra, F., Bebelis, S., Vayenas C.G., Karavassilis C., and Deligiorgis G.,1997, Proceedings of the 1st International Symposium/6th European Workshop "Hydrotreating and hydrocracking of Oil fractions", Oostende, Belgium.
Yitzhaki, D., and Aharoni, C., 1977, *A.I.Ch.E. J.* **23**, 342.

TABLE 1- Kinetic rate constants for batch autoclave and trickle-bed reactor.

	Batch Reactor		Trickle-bed Reactor			
Temperature, °C	$k_{B,1}$, h^{-1}	$k_{B,2}$, h^{-1}	$k_{T,1}$, h^{-1}	$k_{T,2}$, h^{-1}	$\eta_1 = k_{T,1} / k_{B,1}$	$\eta_2 = k_{T,2} / k_{B,2}$
330	23.50	1.43	3.52	0.74	0.150	0.517
315	12.50	0.59	1.88	0.33	0.150	0.559
300	9.00	0.25	1.50	0.15	0.167	0.600
280	1.93	0.21	0.52	0.12	0.269	0.571

TABLE 2- Thiele modulii calculated from equations (12) and (13).

Temperature, °C	Φ_1 (eq. 13)	Φ_2 (eq. 13)	$\Phi_{T,1}$ (eq. 12)	$\Phi_{T,2}$ (eq. 12)	$f_{int,1}/f_{ext,1} = \Phi_{T,1}/\Phi_1$	$f_{int,2}/f_{ext,2} = \Phi_{T,2}/\Phi_2$	$f_{ext,1}$	$f_{ext,2}$
330	3.79	0.94	6.67	1.84	1.76	1.87	0.57	0.54
315	2.84	0.66	6.67	1.67	2.35	2.53	0.43	0.40
300	2.66	0.47	5.99	1.51	2.25	3.21	0.44	0.31
280	1.41	0.50	3.71	1.62	2.63	3.24	0.38	0.31

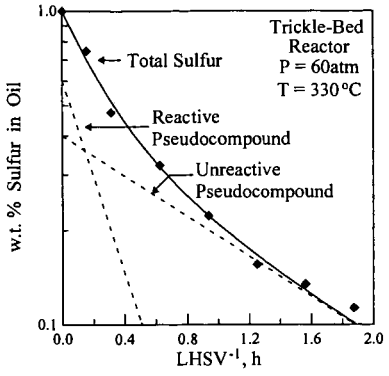

FIGURE 1 - Effect of inverse LHSV on sulfur content of vacuum gas oil and kinetic analysis.

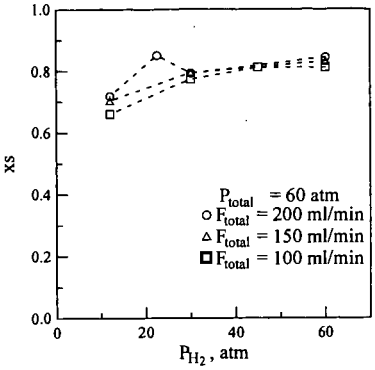

FIGURE 2 - Dependence of sulfur conversion on hydrogen partial pressure. Trickle bed reactor.

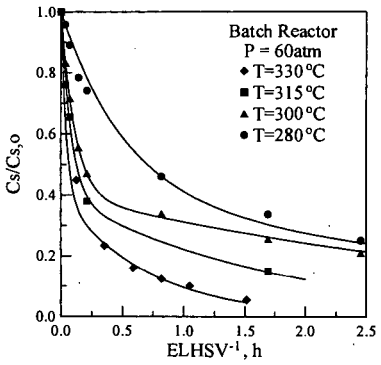

FIGURE 3 - Dependence of sulfur content on the inverse equivalent liquid hourly space velocity and temperature (Batch Reactor).

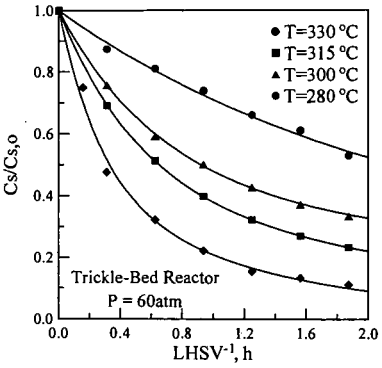

FIGURE 4 - Dependence of sulfur content on the inverse liquid hourly space velocity and temperature (Trickle-Bed Reactor).

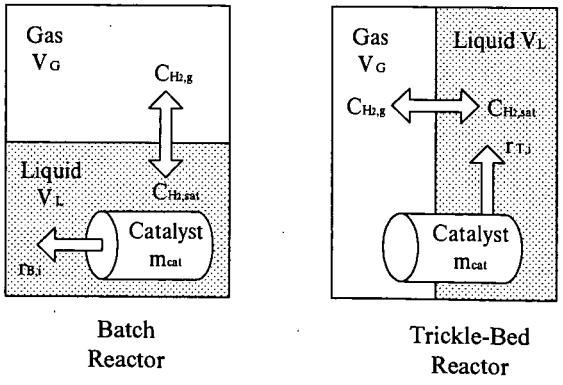

FIGURE 5 - Schematic representation of the particle environment in the batch autoclave and the trickle-bed reactors.

REACTION CHARACTERISTICS AND MECHANISM OF RESIDUUM HYDROCRACKING

Chaohe Yang, Hai Zheng, Feng Du, Chunming Xu, State Key Laboratory of Heavy Oil Processing, University of Petroleum,Dongying City, Shandong Province, China, 257062

Key words: residuum, hydrocracking, reaction mechanism

ABSTRACT

The Gudao vacuum residuum (GDVR) was hydrocracked in a 100 mL autoclave with crushed commercial Ni-Mo Catalyst within a temperature range of 390-420°C. The characteristics of series reaction remains obviously in the residuum hydrocracking. The relationship of coke yield and conversion for catalytic hydrocracking is different from thermal cracking and non-catalytic hydrocracking. The presence of catalyst and hydrogen can significantly inhibit the coking reaction, but simultaneously decreases the cracking rate to a certain extent. The apparent activation energy of residuum catalytic hydrocracking is close to that for thermal cracking, It can be derived that rate limiting step of the residuum catalytic hydrocracking is essentially thermal activation.

INTRODUCTION

The residuum hydrocracking is a very complex reaction system because the feed and product contain innumerable compounds and various reactions occur simultaneously. So it is difficult to study kinetics for every component in this system. Catalytic hydrocracking is more complicate than the non-catalytic hydrocracking. In residuum hydrocracking there often exist three phases of gaseous, liquid, and solid. The catalytic reactions occur on the surface of catalyst and the thermal reactions take place in the interspace of catalyst particles. The reactions not only occur in the liquid phase, but also happen in gaseous phase. Residuum thermal cracking is a free radical chain reaction, but there are different views for the mechanism of heavy oil catalytic hydrocracking due to the various feed, catalysts, and method used by different investigators.

Through the comparison of the chemical analogies of visbreaking, hydro-thermal cracking, catalytic cracking and catalytic hydrocracking, Le Page[1-2] found that the driving force of the conversion reactions is essentially thermal activation in the temperature range applied. The catalyst, the hydrogen present, and the sophistication of the various techniques are merely expediences, which basically participate in limiting, indeed controlling, the condensation side reactions involving the heavy resin and asphaltene molecules.

De Jong [3] (1994) investigated the hydroconversion of heavy vacuum gas oil in a trickle-bed reactor at about 450°C and moderate hydrogen pressure (30atm). He found that the cracking reactions are hardly affected by the presence of the metal active component of the catalyst and thought the cracking reactions are not acid-catalyzed but mainly thermally induced under the prevailing conditions. Through the studies of atmospheric residuum [4] , it is observed that catalytic cracking and thermal cracking take place simultaneously, the lighter distillates are mainly produced from the thermal cracking and the effect of catalyst is to offer active hydrogen to the heavy component in order to controlling coking. That is to say, the hydrogen captured by the light component come directly from the heavy component (the large molecule to be hydrocracked).

In the kinetic model of hydrocracking developed by De Jong[5], the vapor-liquid equilibrium of the reaction mixture was considered. For fitting the experimental data, it was assumed that the cracking of molecules in the vapor phase is 25 times faster than for those present in the liquid phase. In other words it seems as if activated hydrogen in the liquid phase inhibit the radical cracking reaction, while the acceleration is apparent in the vapor phase. This assumption is in line with comments in the investigation of Sanhanen[6] and Shabtai[7]. The residuum hydrocracking made by Xu[8] showed that the conversion of catalytic hydrocracking is greater than that of non-catalytic hydrocracking, which is ascribed to the inhibition of a great number of active hydrogen on the polymerization and coking reactions involving the heavy components.

As a whole, the recognition for heavy oil catalytic hydrocracking has been being semi-theoretical and no consistent conclusion has been drawn about the reaction mechanism and the effect of catalyst and hydrogen. For instance, active hydrogen capturing the large molecular radical can inhibit coking reaction and will be of help for enhancing the distillate yields, but the cracking rate will be decreased and distillate yield declined when the small and medium radicals are captured. The final result would depend upon the concrete situations. In the present paper, hydrocracking characteristics of GDVR will be investigated and the reaction mechanism discussed.

EXPERIMENTAL

The Gudao vacuum residuum was hydrocracked in a 100mL autoclave with crushed ICR-130H Catalyst of 0.35mm average diameter at the initial hydrogen pressure 8.5 MPa, with agitation speed at 850rpm and in the temperature range of 390-420. After hydrocracking, gas, liquid and coke were separated and analyzed. The yield of gas, liquid and coke were determined and the simulated distillation data of feed and liquid product were obtained.

RESULTS AND DISCUSSION

Product Distribution of GDVR Hydrocracking

The yields of gasoline and diesel increase gradually with the reaction time. The increasing rate is slow at the initial period of reaction and become faster and faster toward the end of reaction. The yield of vacuum gas oil (VGO) increases firstly at a faster rate and then slackens gradually. It passes through a maximum at certain time and then declines slowly. The phenomena mentioned above shows that residuum hydrocracking has an obvious characteristic of series reaction. The gas yield increase gradually with time at constant temperature except in the case of 390°C. The coke yield increase quickly at the initial period and slowly with increasing reaction time .

The relationships of product yields and conversions are showed in figure 1. Gas, gasoline and diesel increases gradually with the conversion of >500°C portion, and the increasing rate is slow when the conversion is lower and becomes faster with the increase of conversion. This is because the heavy distillate must be cracked at first into middle distillate and the formation rate of light distillates becomes gradually faster with the increase of middle distillate. The middle distillate content increases at first and reaches to a maximum at a certain conversion, and then decreases gradually.

The relationship of coke yield and conversion for catalytic hydrocracking is obviously different from thermal cracking and non-catalytic hydrocracking[9-12]. For the latter two cases the coke yield increases slowly at the initial period and grows seriously when the conversion passes a critical value (about 55—65% for GDVR), which is similar as the relationship of gas yield

versus conversion in figure 1. For residuum hydrocracking, the coke yield increases quickly when the conversion is low, and the increasing rate slows down gradually with further conversion, which is consistent with the conclusion derived by most investigators on catalyst deactivation. For the present study, the initial quickly coking may be caused by the promotion of acid catalysis on the surface of catalyst, and the hydrogenation function becomes stronger relative the cracking function when the acid sites are gradually covered by the deposition of coke, which can inhibit greatly the coking reaction.

The product selectivity versus conversion of >500°C portion is illustrated in figure 2. The selectivity of gasoline and diesel increase gradually with the conversion. The selectivity of VGO reaches to a maximum at 30% conversion and then decrease gradually. The selectivities of gas and coke decrease seriously at a low conversion range and then tend to a constant. Therefore, residuum catalytic hydrocracking differs from thermal cracking and hydrocracking mainly in serious inhibition of coking and gas formation. The data points of selectivity of gas and coke versus conversion at different temperatures all fall on the corresponding curves respectively. This supports that the temperature has no effect on the selectivity of gas and coke at the conditions used in this study.

Simple kinetic model of GDVR hydrocracking

Whether the driving force of residuum catalytic hydrocracking is essentially the thermal activation can be checked by comparing the activation energy of catalytic cracking with that of thermal cracking. Residuum hydrocracking has ever been described successfully by simple first-order or second-order kinetics. The experimental results have been correlated in terms of the simple kinetic equations, with the plots of ln[1/(1-x)] and x/(1-x) (x is conversion) versus reaction time, t. It is found better to describe the catalytic hydrocracking of GDVR by first-order kinetics than second-order kinetics. But the second-order kinetics is feasible

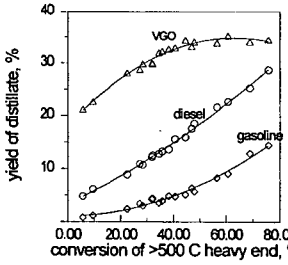

Fig.1A Yields of liquid products versus conversion

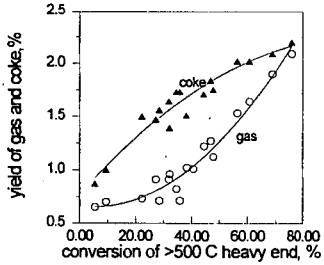

Fig.1B yield of coke and gas versus conversion

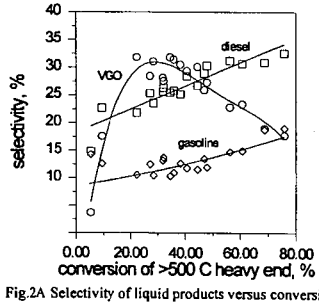

Fig.2A Selectivity of liquid products versus conversion

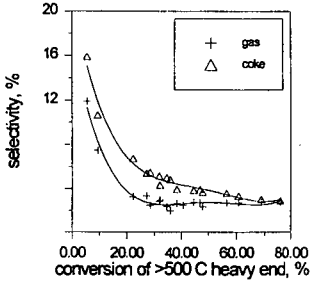

Fig.1B Selectivity of coke and gas versus conversion

when the conversion is not too high, especially for the hydroconversion of >350°C portion. It could be thought that the reaction order is affected by the lumping method when using power kinetic equations to describe hydrocracking. The rate constants (k) at different temperature were calculated according to the first-order kinetics, a linear relationship exists between ln(k) and 1/T (reciprocal of temperature) and the correlation coefficient is 0.9994. The activation energy of GDVR hydrocracking is listed in Table 1.

Table 1 Kinetic reactions of hydrocracking

Feed	Reaction	Catalyst	Temp(°C)	E (KJ/mol)	Reference
Maya VR	VR+H_2→Products	Dispersed Mo	397-438	~290	10
Athabasca asphaltene	Bitumen→ Products	No	370-538	130	13
Athabasca asphaltene	Bitumen→ Products	No	375-420	150	14
Huanxiling asphaltene	VR→ Products	No	385-430	260	15
Distillate	VGO+H_2→ Products	NiW/SiAl	300-430	88.2	16
Coal tar	Tar+H_2→ Products	NiW/SiAl	400-500	73.6	17
GDVR	VR+H_2→ Products	No	400-420	216	18
GDVR	GDVR+H_2→ Products	ICR130H	390-420	260-285	This work

Some kinetic results of heavy oil hydrocracking are summarized in table 1. From these results the activation energy of residuum hydrocracking in the presence of catalyst is very close to that for thermal cracking, whereas the activation energy of distillate catalytic hydrocracking is obviously smaller than that of residuum hydrocracking. This may be explained as the cracking active sites of catalyst play an important role in the distillate hydrocracking, while in the residuum catalytic hydrocracking thermal activation is predominating. The catalysts just create active hydrogen to inhibit coke deposition and simultaneously decrease the cracking rate to a certain extent.

CONCLUSION

From the present study a number of conclusions emerge.

(1) Series reaction model is consistent with the reaction process of residuum catalytic hydrocracking.

(2) The relationship of coke yield versus conversion is obviously different from thermal cracking and non-catalytic hydrocracking. Catalyst and hydrogen can significantly inhibit the coke deposition and simultaneously control the cracking reaction.

(3) The initiation and rate controlling step of residuum catalytic hydrocracking is thermal activation in essence.

(4) GDVR hydrocracking is described very well by the first-order kinetics and reaction order is affected by the lumping method.

REFERENCES

1. Le Page J F. Preprints, Div of Petrol Chem, ACS. 1987, 32(2):470
2. Le Page J F. Chemical and Physico-chemical Problems Involved in the Catalytic Hydroconverson of Heavy Feedstocks. Proceedings of International Conference on Petroleum Refining and Petrochemical Processing. Sept. 1991, Beijing, China. Volume 1, p185.
3. De Jong K P. Ind Eng Chem Res. 1994, 33:821
4. Translation proceedings on Heavy Oil Processing(Chinese), Sino-Petroleum Chem. Press 1990, P.47
5. De Jong K P. Ind Eng Chem Res. 1994, 33:3141
6. Sachanen A N. Conversion of Petroleum. Reinhold, Ney York. 1984, p390
7. Shabtai J, et al. Adv Chem Ser. 1979, 183:297
8. Xu chunmin, lin shixon. Petroleum Processin and Petrochemicals(Chinese), 1995, 26(9):52

9. Liu Chenguang. Hydrocracking of Gudao Residue using Dispersed phase catalysts. Doctoral thesis, University of Petroleum, China. 1991
10. Heck K H, et al. Preprints, Division of Petro.Chem., ACS. 1993, 38(2):417
11. Del Bianco A ,et al. Fuel, 1993, 72(1):75
12. Liu Chenguang, Que Guohe, et al. Petroleum Processing(Chinese). 1993,24(3):57
13. Barbour R V, et al. 172nd Nat Meeting, Am. Chem. Soc, San Francisco, 29 August-3 September, 1976, 21(6):278.
14. Köseoglu R ,Phillips C R. Fuel, 1987, 13(6):56.
15. Yang Jiamo, Liang Wenjie, et al. Journal. of university of Petroleum(Chinese), 1989, 13(6):56
16. Qader S A and Hill G R. IEC Proc Des .Dev. 1969, 8(1):98.
17. Qader S A and Hill G R. IEC Proc Des .Dev. 1969, 8(4):465.
18. Sun Bojun, Que Guohe, et al. Petroleum Processing(Chinese), 1991, 22(4):62

A LUMPING MODEL FOR KINETICS OF RESIDUUM HYDROCRACKING

Chaohe Yang, Chunming Xu, Feng Du, Shixiong Lin, State Key Laboratory of Heavy Oil Hydroprocessing, University of Petroleum, Dongying City, Shandong Province, China, 257062

Key words: residuum, hydrocracking, kinetic model

ABSTRACT

The Hydrocracking reaction kinetics of Gudao Vacuum Residuum was investigated in a 100 ml autoclave with crushed ICR-130H Catalyst in a temperature range of 390-420°C. A lumping model with five parameters for the prediction of the product distribution cure for residuum hydrocracking was proposed as modification of the narrow-boiling point lumping model developed originally for distillate hydrocracking by Stangeland. A major advantage to this kinetic model is that its establishment and application don't need the complete distillation data of residua and products. The results predicted by this model agree satisfactorily with the experimental observation.

INTRODUCTION

The hydrocracking of residuum is a very complex reaction system in which thousands of organic species participate in a highly coupled mode. For this reaction system, it is not possible to establish kinetic equation for every reaction species by the conventional method used in reaction kinetics studies. Such a complex reaction system must be simplified so that the kinetics characteristics of residuum hydrocracking could be elucidated with mathematical equation, that is to say, the lumping method would be used. Lumping method for reaction kinetics is to build a lumping kinetic model in which the innumerable chemical compounds in reaction system is classified as a number of lumps by means of the kinetic characteristics of molecule reaction. The strategy of modeling a given reaction system usually varies with the specific goal to be attained. For example, a large number of chemical compound could be lumped by the total content of a component or a kind of component, by the boiling point range(compounds having similar boiling point grouped into a lump), by the chemical structure(compound having similar chemical structure as a lump), or sometimes by the combination of boiling point range and the chemical structure similarity.

Considerable effort has been focused worldwide on investigating the hydrocracking kinetics of distillates[1] and a better narrow-boiling point lumping model has been proposed by Stangeland (1974) [2] which can be used to predict the product distribution for distillate hydrocracking. There are a few studies on the kinetic model of residuum hydrocracking, and most of them were product lumping models which is not flexible enough to cope with various operation conditions and product scheme, although some investigators have tried to apply such model to commercial operation. Once the product scheme is subject to change, the parameters of product lumping model should be recalculated so as to approach the new product scheme.

Most of studies on the narrow-boiling point lumping model are based on the Stangeland model developed for distillate hydrocracking which requires the complete distillation data of feed and product and characterizes each lump by its final boiling point. These models have not been applied successfully to residuum hydrocracking for lack of the complete distillation curve of heavy oil feed and product. The prediction results is greatly different from the experimental observation in high boiling point range, even if these model are applied to heavier distillate hydrocracking [3].

In the present study, based on the flexibility of the rate distribution and production distribution functions in the Stangeland narrow-boiling point lumping model, a lumping kinetic model suitable for residuum hydrocracking was proposed by combination of the correlation results on SFEF (Super Fluid Extraction Fractionation) fraction hydrocracking [1].

EXPERIMENTAL

The Gudao Vacuum residuum was hydrocracked in a 100mL autoclave with crushed ICR-130H Catalyst of 0.35mm average diameter at the initial hydrogen pressure 8.5 MPa, with agitation speed at 850rpm and in the temperature range of 390-420°C. After hydrocracking, gas, liquid and coke were separated and analyzed. The yield of gas, liquid and coke were determined and the simulated distillation data of feed and liquid product were obtained.

KINETIC MODEL

The kinetic model is based on the concept of pseudo-components (narrow fractions) and is similar to one proposed by Stangeland (1974). Assumptions in the present model are as follows:

(1)The feed and products are represented by a series of continuous mixture which are pseudo-components of boiling range of 28°C and could be characterized by its final boiling point. The lightest pseudo-component is gas lump of boiling point below 10°C. The residual part of boiling point above 537.8°C was treated as a lump, the heaviest pseudo-component, and characterized by a pseudo-boiling point (TBP_f).

(2)Each pseudo-component is assumed to undergo a first order irreversible reaction. Polymerization reaction is neglected and no coking reaction is supposed.

(3)The rate constant of hydrocracking of any lump is assumed to be relative to the heaviest lump in the model.

(4)A lump can be hydrocracked into any lighter lump, but no conversion occurs among the lightest four lumps.

The reaction kinetic model of residuum hydrocracking is given by the following differential equations:

$$\frac{dF_i}{dt} = -k_i F_i + \sum_{j=1}^{i-1} k_j p_{ij} F_j \qquad i=1,2,\ ,n$$

where k_i is the constant of lump i hydrocracking (hr^{-1}), t is reaction time (hr), and p_{ij} is the fraction of the cracked products from a heavier component, j, that become a lighter component i.

The calculation methods of k_i and p_{ij} have a great influence on the validity of the model. It is too difficult to derive a mathematical model if the number of model parameter is too great. But if the model parameters are not sufficient, the model would be lack of flexibility in application. Equations for calculating k_i was selected as follows:

$$k_i = k_0 \exp\left(-\frac{E}{RT_r}\right)\cdot\left[T_i + A\left(T_i^3 - T_i\right)\right] \qquad T_i = \frac{TBP_i}{TBP_f}$$

where R is the gas constant ($8.314 J \cdot K^{-1} \cdot mol^{-1}$), T_r is the temperature (K), T_i—is the temperature parameter of lump i, TBP_i is the final boiling point of lump i (°F) and TBP_f is the pseudo-boiling point of the heaviest component (°F). k_0 is frequency factor (hr^{-1}) and E represents the apparent activation energy. Li (1994) proved that the relative deviation of

$k_0 \exp\left(-\frac{E}{RT_r}\right)$ is not greater than 3% when k_0 and E vary in a reasonable range. So the apparent activation energy was set to a constant value (E=108KJ/mol) [4].

Because there is a strong decreases in cracking rate as the boiling point of hydrocarbon is less than 250°F and the heaviest lumping in residuum hydrocracking has a dominant amount, the rate constant k_i was modified in terms of the following relations:

$$k_i = \begin{cases} 0.0 & TBPi \le 250 \\ 0.33k_i & TBPi = 300 \\ 0.78k_i & TBPi = 350 \\ 3.0k_i & TBPi = TBP_f \end{cases}$$

and the product distribution function was represented by the equations as follows:

$$p_{ij} = \begin{cases} 0.0 & i \le j \\ C \cdot \exp\left[-0.00693 \cdot (TBP_j - 250)\right] & i = n, j \le i-1 \\ P(Y_{ij}) - P(Y_{i+1,j}) & i < n, j \le i-1 \end{cases} \qquad P(Y_{ij}) = \left[Y_{ij}^2 + B\left(Y_{ij}^3 - Y_{ij}^2\right)\right]\left(1 - p_{nj}\right)$$

$$Y_{ij} = \frac{TBP_i - 50}{TBP_j - 100}$$

So, kinetic parameters (k_i and p_{ij}) in residuum hydrocracking reaction can be represented by five model parameters (k_0, A, B, C, TBP_f). The distinction of this model and Stangeland model lies in:

(1) Suitable for the cases lacking complete TBP distillation data of feed and product.
(2) The pseudo-boiling point (TBP_f) is proposed to characterize the heaviest lump and the rate constant distribution function is modified.
(3) Any lump may be hydrocracked into any lighter lump. this is especially important when the heaviest lump accounts for a dominant amount.
(4) The pseudo-boiling point, TBP_f, was set by the correlation of SFEF fraction hydrocracking.

Estimation of model parameters is done by algorithm according to Herbest (1968) [5]. The objective function is defined as the sum of the squares of the differences between the observed and calculated composition of the pseudo-component.

DISCUSSION

Through the estimation of model parameters, TBP_f at different reaction temperature were found approximately the same value, 1100°F. It could be thought that the properties of feed at the zero reaction time are similar no matter what reaction temperature was set, although the cracking reaction may occur already to a certain extent. Thus, TBP_f was fixed invariably to be equal to 1100°F, the deviation due to this decision can be compensated by adjusting other parameters. The relations of other model parameters and reaction temperature are given as follows,

$$\left.\begin{aligned} A &= 11881.8 - 88.0901Tr + 0.217577Tr^2 - 0.000179023Tr^3 \\ B &= 2329.12 - 17.6345Tr + 0.0445643\ Tr^2 - 3.75908E-005\ Tr^3 \\ C &= 28180.1 - 210.262Tr + 0.522687\ Tr^2 - 0.000432817\ Tr \\ k_0 &= 11960.5 - 88.8419Tr + 0.219754\ Tr^2 - 0.000180983\ Tr^3 \end{aligned}\right\}$$

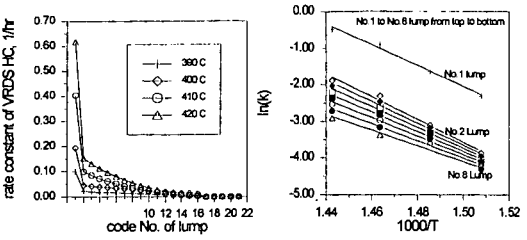

Fig. 1 Rate constant of each lump hydrocracking Fig 2 Rate constant of lumps *v.s.* temperature

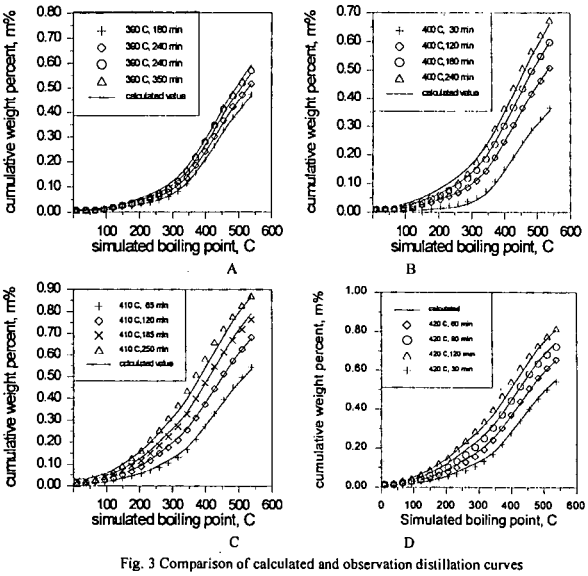

Fig. 3 Comparison of calculated and observation distillation curves

The rate constants of each lump hydrocracking were illustrated in Figure 1. The rate constant of the heaviest lump is far larger than those of any other lumps. At the same temperature, hydrocracking rate decreases gradually with the lowering of boiling point of lump component. The rate constant of the heaviest pseudo-component is 3.6~4.1 times as large as that of the next lump and 3~4 orders of magnitude larger than that of the lightest pseudo-component which is supposed to have been undergone hydrocracking. The methods chosen for calculating the cracking rate and product distribution of 1 to 8 lumps pave the way to the success of the model.

The cracking rate constants of the lump with higher boiling point are presented in Arrhenius plots in Figure 2. For each lump a straight line was obtained, especially for the heaviest four lumps. This suggests that the present model represents adequately the kinetic characteristics of GDVR hydrocracking.

The observed and calculated product yields at different reaction conditions are summarized in Table 1. The relative deviation between observed and predicted yields of the distillate products are not greater than 1.5% which is just the same as the permitted error of simulated distillation except for reaction condition at 410°C and 120 min.[6] As shown in figure 3, the predicted yields based upon those model parameters mentioned above are represented as solid lines and the discrete observed data as points of different form. In general, the agreement is quite good and

probably closed to experimental error, which shows that it is feasible to characterize residuum-hydrocracking reaction by this narrow-boiling point lumping model.

CONCLUSION

A lumping model suitable for residuum hydrocracking was proposed by modifying the Stangeland model, and the agreement of the calculated yields with the observed ones is quite good. But there is much work to be done in order to check the suitability of this model for different hydrocracking feedstocks and various reaction conditions.

Table 1 The observed and calculated distillate product yield at different reaction conditions (m%)

Temperature, Time	390°C, 180min			390°C, 240min			390°C, 300min		
	Obs.	Calcd.	Diff..	Obs.	Calcd.	Diff..	Obs.	Calcd.	Diff..
gas	0.73	0.43	0.30	0.71	0.59	0.12	0.82	0.76	0.06
38—204°C	2.34	2.64	-0.30	3.11	3.41	-0.30	3.73	4.13	-0.40
204—343°C	8.20	8.25	-0.05	9.85	9.69	-0.16	11.62	11.02	0.60
343—537°C	36.08	35.53	0.55	37.93	37.95	-0.02	40.74	40.08	0.66
>537°C	52.65	53.14	-0.49	48.40	48.36	0.04	43.09	44.0	-0.91
Temperature, Time	**390°C, 350min**			**400°C, 30min**			**400°C, 120min**		
	Obs.	Calcd.	Diff..	Obs.	Calcd.	Diff..	Obs.	Calcd.	Diff..
gas	0.71	0.90	-0.19	0.70	0.95	-0.25	0.91	0.66	0.25
38—204°C	4.04	4.71	-0.67	1.06	1.05	0.01	3.43	3.81	-0.38
204—343°C	12.11	12.05	0.06	5.49	5.05	0.34	9.91	9.79	0.12
343—537°C	40.90	41.66	-0.76	29.17	28.68	0.49	36.46	36.83	-0.37
>537°C	42.23	40.68	1.55	63.58	64.36	-0.78	49.29	48.91	0.38
Temperature, Time	**400°C, 120min**			**400°C, 240min**			**410°C, 65min**		
	Obs.	Calcd.	Diff..	Obs.	Calcd.	Diff..	Obs.	Calcd.	Diff..
gas	1.02	1.08	-0.06	1.12	1.46	-0.34	0.91	0.73	0.18
38—204°C	4.92	5.50	-0.58	5.48	6.76	-1.28	4.61	5.03	-0.42
204—343°C	12.52	12.60	-0.08	16.14	14.65	1.49	11.18	11.89	-0.71
343—537°C	41.25	40.70	0.55	44.76	43.21	1.55	37.66	35.85	1.84
>537°C	40.29	40.12	0.17	32.50	33.92	-1.42	45.64	46.53	-0.89
Temperature, Time	**410°C, 120min**			**410°C, 185min**			**410°C, 255min**		
	Obs.	Calcd.	Diff..	Obs.	Calcd.	Diff..	Obs.	Calcd.	Diff..
gas	1.22	1.35	-0.13	1.64	2.08	-0.44	2.09	2.86	-0.77
38—204°C	5.70	8.14	-2.44	9.92	10.91	-0.99	14.21	13.17	1.04
204—343°C	14.65	16.68	-2.03	21.21	20.76	0.45	27.31	25.87	1.44
343—537°C	43.57	41.41	2.16	44.56	45.48	-0.92	43.48	45.12	-1.64
>537°C	34.86	32.15	2.71	22.66	20.77	1.89	12.91	12.97	-0.06
Temperature, Time	**420°C, 35min**			**420°C, 60min**			**420°C, 120min**		
	Obs.	Calcd.	Diff..	Obs.	Calcd.	Diff..	Obs.	Calcd.	Diff..
gas	0.96	0.54	0.42	1.27	0.93	0.34	1.90	1.90	0.00
38—204°C	4.45	5.35	-0.90	6.55	7.19	-0.64	13.42	13.21	0.21
204—343°C	11.59	11.96	-0.37	16.42	16.72	-0.30	24.62	22.99	1.63
343—537°C	37.13	37.38	-0.25	41.17	40.54	0.30	41.81	43.23	-1.42
>537°C	45.87	44.74	1.10	34.59	34.61	-0.02	18.25	18.67	-0.42

REFERENCES

1. Yang, Chaohe. Characteristics and Kinetics of Heavy Oil Hydroconversion. Doctoral Thesis, University of Petroleum, Beijing, China, 1997
2. Stangeland, B. E., et al. IEC Pro. Des. Dev. 1974, 13(1):71.
3. Raychaudhuri, U., et al. Fuel Sci Techn Int'l, 1994, 12(2):315
4. Li dongsheng, Sun wei, Petroleum Processing and Petrochemicals, (Chinese)1994, 25(5):29.
5. Herbest, J. A., Fuerstenau, D. W. AIME Trans., 1968, 241:538.
6. ASTM Standard: D5307, Standard Test Method for Determination of Boiling Range Distribution of Crude Petroleum by Gas Chromatography, Annual Book of ASTM Standards. Vol.05.02, P564, 1993.

Pyrolysis Kinetics and Mechanism for Average Molecular Structures of Heavy Oil Crudes.

Iván Machín, Edgar Cotte
PDVSA-Intevep, Process Department, P.O. Box 76343, Caracas 1070A, VENEZUELA

Keywords: Heavy Crude Oils, Pyrolysis, Kynetics, Molecular Models

ABSTRACT

A molecular kinetic model named PYRO2, for pyrolysis of heavy crude oils, has been developed. This model uses average molecular structures (AMS) derived from experimental analytical data obtained from heavy crude oils. The PYRO2 model consists of about 50 reactions associated with homolytic C-C, C-S, C-N and C-H bond breaking over saturated chains, bridges and cycles bounded to condensed rings. This model was applied to average molecules of Athabasca and Boscan crude oils in order to reproduce thermal conversion and product distribution data. The dependence of conversions to volatile products and coke yields on temperature and time of reaction are reproduced within a 10 % deviation from the experimental results. Variations in the distribution of gas and liquid components of volatile products follow the same tendencies as experimental results; but they depart significantly from the absolute values. This may indicate that new reaction paths and/or additional corrections in the AMS's are necessary. Two such factors, one of each, were identified..

INTRODUCTION

In very complex systems, like crude oils, the reaction mechanism and associated kinetics are not directly accessible for individual molecular entities. Kinetic models are thus based on different representations of molecular aggregations or the key properties of interest. According to the methodology used, kinetic models can be divided in three categories: (a) Pseudokinetic Models, in which the reaction schemes are associated with transformations of pseudocomponents that represent the crude oil fraction. Due to the fitting parameters they contain, their predictive capacity is limited to the specific crude oil and/or the process to which they were defined [1]. (b) Kinetics of model compounds, which use simple molecules to simulate reactions associated with substructures of very complex systems. These models assume similar behavior in the substructures they intend to represent [2]. (c) Kinetic models of complex systems, in which it is given explicit molecular structure of reactants and intermediates used to represent the crude oil or its components. The reactants can be represented by a distribution of individual molecules, stochastically generated by a Monte Carlo methodology, or by an average molecule [3-5]. In this work the kinetic model PYRO2 uses average molecular representations of crude oil. They were obtained based on elemental analysis, proton NMR and VPO molecular weights using a methodology described in the literature [6-9].

MODEL DEVELOPMENT

In its most simple form, it is possible to associate the pyrolysis process with homolytic C-X (X=C, S, N, H) bond scissions in the molecules R-R' of crude oil to produce two free radicals:

$$R - R' \rightarrow R. + R'. \qquad (1)$$

To start with, we builded up our kinetic model with the minimum set of elemental reactions necessary to produce results comparable with experimental data from our own work or from the literature. In future work, complexity will be increased as necessary according to the results of this comparison. Therefore the PYRO2 model only considers neutral molecules and does not contain the evolution of radical fragments. Accordingly, we assumed stabilization of the free radicals in reaction (1) with hydrogen from any internal hydrogen transfer mechanism and use the generalized reaction:

$$2H + R - R' \rightarrow RH + R'H \qquad (2)$$

where each bond breaks in R-R´ according to the Arrhenius expression of kinetic rate constant (k):

$$\ln(k) = \ln(A') + Ea/RT \qquad (3)$$

The pre-exponential factor A' was obtained from Gavalas et al. [10]. The activation energy Ea was calculated based on the Bell-Evans-Polanyi principle (BEP) [11,12]. This principle associates the change of energy between the reactants and the transition state (Ea) with the reaction enthalpy for a given elemental step in the kinetic mechanism. In our case the rate determining step depends on the difference in energy between the bond breaking step BS(C-X) and the bond formation step for RH and R'H, represented by a constant c. We found a practical way to evaluate the Ea parameter of (3) for reaction (2) for any C-X bond scission according to the expression:

$$Ea \sim BS(C\text{-}X) - c \qquad (4)$$

where c=49.40; 44.97; 49.40 for X=C, S, H and BS(C-X) are the C-X bond strengths.

We found a linear correlation between the experimental BS parameter and the theoretical quantum parameter known as Diatomic Energy (DE) for a series of very different compounds:

$$BS(A\text{-}B) = a + b\, DE(A\text{-}B) \qquad (5)$$

This equation allowed us to evaluate the BS parameter for any other compound or structure of interest. Correlation (5) was obtained as follows:
We selected simple model molecules whose BS parameters were tabulated in the CRC Handbook [13] and evaluated the Diatomic Energy (DE). The linear regression parameters a and b were then obtained. The Diatomic Energies (DE) were calculated using an energy partitioning scheme presented by Kollmar [14] for the analysis of *ab initio* and semi-empirical SCF calculations. The resulting value can be associated with the bond strength Ruette and Sanchez[15] have proposed this parameter as a tool for bond analysis. Based on semi-empirical methods, the following expression was obtained:

$$DE(A-B) = \sum_{i,j \in A,B} p_{ij}(h_{ij} + f_{ij}) \qquad (6)$$

Where h_{ij}, p_{ij} and f_{ij} are the one electron matrix, bond order matrix and Fock matrix elements, as obtained from the INDO1 calculations [16]. DE(A-B) contains contributions of the resonance energy and of the electron exchange energy to the bond and does not contain electrostatic energy terms which are included by the one-center energy terms. The second purpose of using the DE parameter is to establish an increasing order for Energy Dissociation of bonds in the reactant AMS of interest. We associated each bond breaking in the molecule to an elemental step in our kinetic model, obtaining schemes like that depicted in Table 1. Afterwards, we compared the theoretical products distribution with the experimental distribution derived from the pyrolysis. This allowed us (a) to check the practical consistency of the kinetic model, and, (b) to check the molecular structure proposed as model for the fractions here considered. Table 1 shows the parameters obtained from the best linear fit of the calculated ED (in Hartrees) to the experimental dissociation energy BS for C-C, C-S and C-H bonds.

Afterwards we introduced the following conditions in the kinetic model:
a) Hydroaromatic rings generate aromatic rings. A model of this type of reaction is:

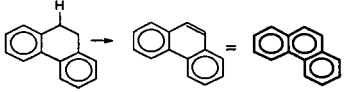

(7)

The activation energy (Kcal/Mol) was defined as:

$$Ea = BS(C\text{-}H) - 166.92 - 23.8\, n \qquad (8)$$

where n is the number of aromatic rings generated in the reaction; in this case, n = 1. b) The sequence of bond breakings in each molecular structure was organized by increasing C-X bond energies from quantum mechanical calculations. c) The aromatic C-C, C-S and C-N bonds are not broken.

3. RESULTS

We applied the PYRO2 kinetic model to the pyrolysis of the AMS depicted by Cotte [17] for Boscan asphaltenes (Fig. 1) and Sanford [18] for Athabasca residue (Fig.2). The differential equations associated to the rate laws of the elementary reactions proposed in this study were solved using a Fortran program developed by Braum and coworkers [19]. Boscan asphaltenes pyrolysis can be represented by the cracking of the aliphatic side chains (some could be bridges) and naphtenic cycles. This process leaves the peri-condensed aromatic rings system as coke, represented by a black circle in the compact representation of Fig. 1. This cracking progresses according to the increasing bond energy values. Aliphatic C-C bonds γ to the aromatic rings break first, followed by β bonds, naphtenic and possibly α aliphatic bonds, in all cases following the increasing bond strength. Branches from the opening of naphtenic rings, once formed, crack according to this sequence. The conversion to volatile products measured by weight yield and the coke yield in a thermogram (Fig. 3) and the light product yields (Fig. 4) can be predicted in a reasonable way from the model in this peri-condensed representation of Boscan asphaltenes AMS (Fig.1). However, for the open kata-condensed Athabasca molecular representation (Fig. 2), this trend did not work. The kinetic model invariably went to zero coke due to the complete fragmentation of the Fig. 2 molecule to volatile products. The calculation by quantum mechanical methods of bond energies indicated that the weakest bonds were not the γ or further away aliphatic bonds of aromatic side chains, but instead the C-H bonds in the hydroaromatic substructures to the right side of Fig. 2. When this bond rupture order was allowed, the very first process that occurred was the aromatization of the right side of the molecule in Fig. 2, according to the first six steps in Table 1. This aromatized part was represented by a black circle in Table 1. From this step on, this structure remains as a coke precursor not originally present. The left side totally cracked to produce gases and liquids, as depicted in Table 1 after step 6.

From this kinetic model results, we concluded that this very early aromatization, that introduces a coke precursor nucleus in the molecule, even before liquids and gases are formed, is a very important principle that governs the natural tendency to form coke in complex hydrocarbon systems. It could also explain the increased coke yield of heavy petroleum fractions pretreated by extended periods of time at low temperatures (below 300°C), as reported by Cotte et. al. [20]. Present tendency is toward the consideration of kata-condensed structures, like that of Fig. 2, as more representative of heavy petroleum fractions [18], than those peri-condensed as in Fig. 1. This principle indicates a likely path to coke formation in these open systems, and the expansion of the reaction network in pyrolysis to include it, together with other non-conventional reactions like the retrograde reactions proposed by Mc. Millen and Malhotra [21]. The reasonable agreement between the tendencies in products formation and the conversion and coke yields propose by Sanford for the AMS of Fig. 1 (Fig. 6), indicates the usefulness of the PYRO2 kinetic model and its predictive capability for gross results, in spite of the very simple assumptions it contains. The disagreement with gas and liquid yields, we believe, indicates mainly the failure of the AMS to contain certain reactivity information. This was particularly evident in the CO yield for Boscan asphaltenes. Experimentally, this is one of the first gas product to be formed at about 400 °C, before the bulk of gases peak [17], but the model indicated its formation at about 600 °C, after the bulk gases formation in Fig. 6 (does not appears due to the Y-scale). This disagreement indicates that although the AMS is consistent with the analytical data from which it was builded up, its reactivity is not consistent, and the position of the CO group should be modified accordingly. Improvements in reaction networks and in the AMS's can be made with the use of this model. This should give a deeper knowledge of the chemistry of heavy petroleum fractions, which was the main objective of the development of the PYRO2 model.

4. SUMMARY AND CONCLUSIONS

A kinetic model was developed to study the thermal reactivity of average molecular structures representative of heavy petroleum fractions. This model is based on the application of the Arrhenius equation to the rupture of C-X bonds, arranged by increasing activation energies estimated through quantum mechanical principles and correlations. Reasonable gross agreement was obtained with experimental data and with chemical intuition as applied to the pyrolysis of a crude residue and an asphaltene. This application indicated that:

-The reproduction of the experimental thermogram of the boscan asphaltenes, indicated that the theoretical considerations to obtain the activation energies associated with each step of kinetic model are in reasonable agreement with experimental data.

-The PYRO2 model did not reproduce the distribution of volatile products relieved from the thermogravimetric pyrolytic experiments of the fraction considered. This mismatch of some kinetic model results with experimental data indicated that further improvements or corrections are necessary in the average molecular structures representative of heavy petroleum fractions.

-Early aromatization of certain hydroaromatic moieties, during the thermal treatment of very complex kata-condensed hydrocarbon systems, appears to be an important factor in the natural tendency of heavy crude oil fractions to produce coke. This aromatization should be included as an important further reaction in the networks representative of hydrocarbon systems under pyrolysis conditions.

REFERENCES

[1] Trauth D., Yasar M., Neurock M., Nigam A., Klein M., Kukes S.; Fuel Sc. and Tech. Intl., **10**, 1161-1179 (1992).

[2] Savage P. E.; Am. Chem. Soc. (ACS), Div. Fuel Chem., 42, 13-17, 1997.

[3] Savage P. E., Klein M. T.; Chem. Eng. Sc., **44**, 393-404 (1989).

[4] Neurock M., Libanati C., Klein M, AlCheE Symposium Series, No. 273, **85**, 7 (1989).

[5] Scott M. S., Neurock M. and Klein M. T., Chem. Eng. Sc., **48**, 4081-4096 (1993).

[6] Dickinson E. N.; Fuel, 59, 290-294, 1980.

[7] Speight J. G.; Moschopedis S. E. Bunger J. W. and Li N. C. Ed.; Adv. Chem Ser. 195, 1-15, Washington D.C., 1981.

[8] Yen T. F.; Wu W. H.; Chilingarian G. V.; Energy Sources , 7(3),275-305, 1984.

[9] Leon V.; Fuel 66, 1445-1446, 1987

[10] Gavalas, G., Cheong, P., Jain, R., Ind. Eng. Chem., Fundam., 20, 113-122, 1981.

[11] Dewar M., Dougherty R.; "The PMO Theory of Organic Chmistry", Edit. Plenum Press, New York, (1975), 65-69, 212-220.

[12] Neurock M., Klein M. T.; Chemtech, 26-32, September (1993).

[13] CRC Handbook of Chemistry and Physics, 76th Edition (1995-1996) pag. 9-64.

[14] Kollmar H.; Theoret. Chim. Acta (Berl.). **50**, 253 (1992).

[15] Sánchez M., Ruette F.; J. Mol. Struct. (Theochem). **254**, 335 (1992).

[16] ZINDO Code Molecular Simulations, Inc.

[17] (a)Cotte E.; MSc Thesis; Venez. Inst. of Sc. Res. (IVIC). 1977.(b)Cotte E.,Calderón J. L.; Rev. Tec. Intevep, 1(2):109-117,1981.

[18] Sanford E.; Ind. Eng. Chem. Res., **33**, 109 (1994).

[19] Braum W., *Herron J., Kahaner K.; Int. J. Chem. Kinetics, 29, 51 (1988).*

[20] Cotte E., Ovalles C., Scaglioni G., Castro W.; Thermal Reactivity of Venezuelan Heavy Crude Fractions, 5th Chem. Cong. of Nth. Am. Cancun, Mexico, 11-15 Nov., 1997

[21] McMillen, D. F.; Malhotra, R.; Am. Chem. Soc. (ACS), Div. Fuel Chem., v.42, No.1, April 13-17, 1997.

Table 1. Pyrolysis scheme derived from the PYRO2 kinetic model for a cracked Athabasca residue Average Molecular Structure.

Step	Molecule	Ea Kcal/ Mol	Step	Molecule	Ea Kcal/ Mol	Step	Molecule	Ea Kcal/ Mol
0	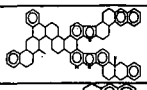	-	12	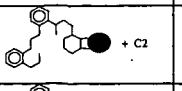	19	24	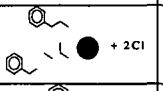	22
1	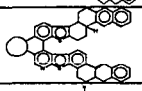	30	13	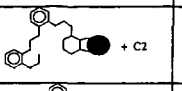	19	25	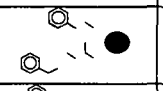	22
2	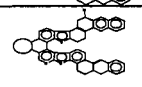	38	14	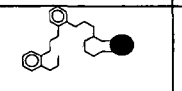	19	26	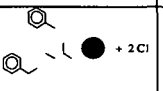	23
3	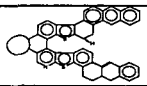	33	15	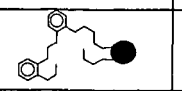	19	27	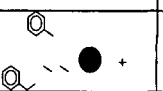	23
4	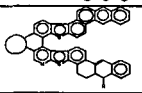	30	16	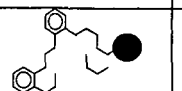	20	28	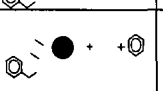	24
5	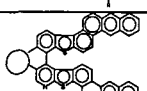	30	17	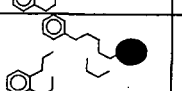	22	29	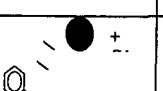	24
6	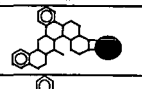	29	18	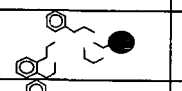	22	30	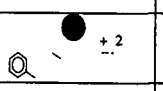	24
7	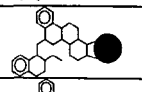	19	19	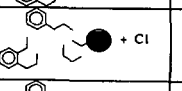	22	31	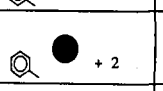	26
8	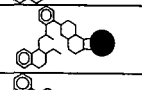	19	20	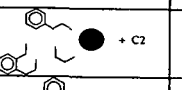	22	32	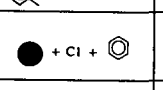	27
9	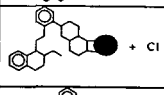	19	21	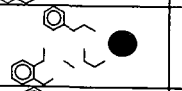	22	33	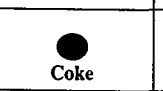	-
10	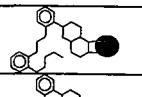	19	22	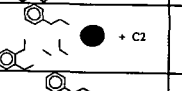	22			
11	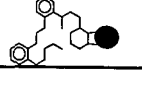	19	23		22			

Table 2. Fitting parameters, correlation factor r^2, and standard deviation s for the correlations: BS(A-B) = a + b DE(A-B)

Bond (A-B)	a (Kcal)	b (Kcal/Hartree)	r^2	s (Kcal)
C-C	-95.371	1339.273	0.95	16.8
C-S	-31.952	998.201	0.94	5.7
C-H	-414.488	4837.562	0.94	5.7

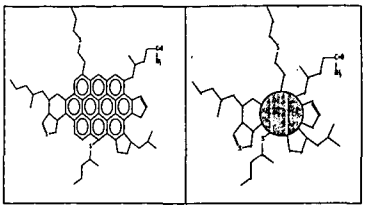

Fig.1. The Boscan Asphaltene Average Molecular Structure (from Ref. 17) and its Compact Representation

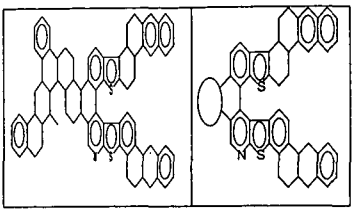

Fig.2. The Average Molecular Structure of an Athabasca Cracked Residue (from Ref.18) and its Compact Representation.

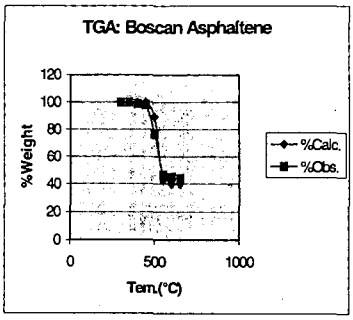

Fig.3. Calculated (from PYRO2 model) and Observed (form Ref. 17) TGA of Boscan Asphaltene.

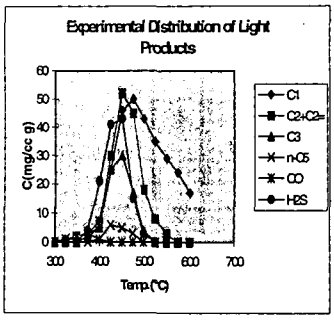

Fig.4. Experimental Distribution of Light Products from the pyrolysis of Boscan Asphaltenes. Data from Ref. 17

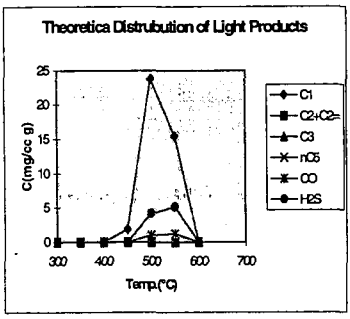

Fig.5. Theoretical Distribution of Light Products from the pyrolysis of Boscan Asphaltenes obtained from PYRO2 Model.

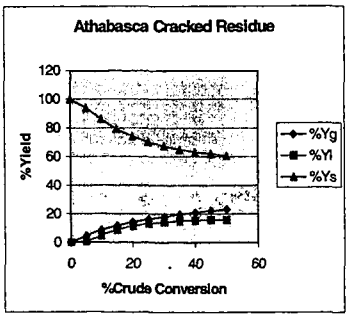

Fig.6. Gas (Yg), liquid (Yl) and residue plus solids (Ys) yields calculated from the PYRO2 kinetic model for the Athabasca Residue.

THE TWO PHASE, TWO PLUG REACTOR
THE SEPARATE PHASE RESIDENCE TIMES EFFECT

Colin McGreavy
The University of Leeds, Chem. Eng. Dept.
Leeds LS2 9JT, UK

Marcos Sugaya
Petrobras S.A., Cenpes
Rio de Janeiro 21910-900, Brazil

KEYWORDS: Delayed coking, visbreaking, pyrolysis

ABSTRACT

The two phase, two plug flow reactor (2TP-R) is a distinctive example which highlights the problems in modeling complex multiphase flows where the different phases can have well-defined and independent residence times which need to be taken into account. As a case study, the pyrolysis of distillation residues in a 2TP-R scheme is examined to illustrate some of the issues in characterizing such systems which include practical applications such as visbreaking and delayed coking furnaces and other residue upgrading processes. Kinetic parameters for the lumped pseudocomponents system have been derived from isothermal pilot plant runs. Operating parameters and geometric considerations have been examined aiming at maximization of the light derivatives in the pyrolysis of residues. It is important to balance the conversion between the furnace and the soaking drums downstream to optimize the yield of products and the overall operation.

INTRODUCTION

Delayed coking furnaces are designed to postpone chemical transformations in the feed to the soaking drums downstream so as to avoid deposition of coke in the furnace tubes which would limit the campaign time. High velocities, moderate heat fluxes and large surface/diameter ratios are necessary to accomplish this.

Generally, a box geometry with two radiant sections connected to a single convection section is used. The tubes are horizontal and, in the radiant section, they are often located adjacent to the walls but separated on a large pitch in order to improve the distribution of heat. More recently the distribution of heat has been enhanced by placing the tubes in a double fired zone at the center of the radiant boxes with the feed flowing downwards in a direction opposite to the flow of combustion gases. This has the advantage of reducing the maximum wall temperatures.

Not all of the tube length is used for heat exchange. Dead end sections are usually connected by 'mule-ear' heads to one side of the furnace with 'U' sections at the opposite side. These configurations give rise to significant pressure drops while adding to the soaking volume. A variety of tube lengths, diameters and pitches is also used.

Kinetic constants for chain initiation reactions in the liquid and vapor phases are related by the equation

$$K_{liq} = k_{vap} \cdot \exp\left(\frac{\Delta S^{\otimes}}{R} - \frac{\Delta H^{\otimes}}{RT}\right) \qquad \text{Equation 1}$$

where $\Delta S^{\otimes}$ and $\Delta H^{\otimes}$ are the differences in the entropy and enthalpy of the activated complex and reactants in the liquid and vapor phases (1). Since $\Delta H^{\otimes}$ is negative, reactions in the vapor phase can be neglected at the low temperatures used in delayed coking, visbreaking and similar processes.

The generation of vapor in the process influences the residence time of the liquid phase because it effectively reduces the volume. Steam can be used to reduce the partial pressure of the hydrocarbons in the vapor phase and hence increase the vaporization which enables the residence times to be controlled. This arrangement results in increased flexibility for a particular geometry. When estimating residence times, it is therefore important to consider a distinction between the liquid holdup in the coil and the vapor/liquid ratio which is determined by phase equilibrium.

APPROACH

The model uses lumped kinetic parameters derived from pilot plant experiments. The liquid phase holdup can be estimated using the method due to Hughmark (2). As the hydrocarbon vaporizes, the flow regime along the tubes changes. Baker's map (3) can be used to follow the changes. Phase equilibrium is based on the Redlich-Kwong equation as modified by Soave (4). The physical properties have been estimated using the method due to Dean-Stiel (vapor viscosity), Twu (liquid viscosity), Mallan *et al.* (liquid conductivity), Stiel-Thodos (vapor conductivity) and Gunn-Yamada-Rackett (liquid density). The temperature dependence of liquid viscosities is obtained from the ASTM procedure modified by Wright (5), using appropriate mixing rules. Single phase pressure drop is calculated using the equation due to Chen (6). For two phase flow, the method of Dukler (7) and a proprietary correlation (8) have been used.

A mass balance is given by

$$\frac{dc_{i,T}}{dx} = -\frac{h_L A_T \rho_L}{W_T} k_i c_{i,L} \qquad \text{Equation 2}$$

where c_i stands for the concentration of species i, h the holdup, A the cross-sectional area, W the mass flow rate, ρ the density, k the kinetic constant and the subscripts L and T denote the liquid phase and the total stream respectively.

Enthalpies are calculated based on the Lee-Kesler equations and the heat of reaction is taken as 800 J/kg for products boiling below 204 C (ASTM D-86). Wall temperatures are estimated from the heat flux and adopting the definition of heat transfer coefficients and the methodology described in API RP-530 (1988).

The 2TP model used here has been extended to take account of the transfer line between the furnace and the coking drums with pipe fittings accounted for by using appropriate equivalent lengths.

Change in the static head is based based on the following equation

$$\left(\frac{dP}{dx}\right)_d = \left(h_L \rho_L + h_V \rho_V\right) \sin\theta \qquad \text{Equation 3}$$

where P is the pressure and θ is the inclination to the vertical. The flow regime is taken from the zones defined by Griffith and Wallis (9).

RESULTS AND DISCUSSION

The furnaces at Petrobras Gabriel Passos Unit 52 have two radiation chambers connected to a single convection section with the feed being split into four passes per furnace. Tubes in the radiation boxes are in two horizontal lines near the walls fired from the center and each furnace feeds a pair of coke drums. Geometric data are presented in Table 1, operating conditions in Table 2. Table 3 contains a geometric description of the transfer line.

Table 4 compares the simulation results with process data. Furnace B generates more coke than A, as indicated by the measured pressure drop, which is 30 % higher. The campaign time is not reported, although furnace A has recently been decoked. The calculated pressure drop in B needs to be increased by 23% to reproduce this effect. Correspondingly, A needs to be reduced by 31% to match the plant pressure drop. This means that the pressure drop correlation is conservative as far as design is concerned.

The heat duty and fuel gas consumption matches the plant data very well (Table 4). In Figures 1-2 the temperature of the tubes predicted by the model compare well with the plant and the agreement between the model output and the process data is generally good.

In Figure 3, the composition profile in furnace A is represented by the fraction of products boiling below 350 C. As can be seen, reaction is significant only in the final third of the tubes, where the temperature is above 400 C. No significant reaction occurs in the convection zone. Higher coke drum temperatures favor condensation reactions at the expense of cracking, because of the different activation energies. However this also increases the vaporization in the drums causing in a net decrease in coke production.

The choice of appropriate operating conditions is crucial in seeking to increase the production of liquids and needs to be anticipated at the design stage because more options are available at this time. In particular, a low operating pressure is very desirable since it decreases the production of coke.

Table 5 shows that an important fraction of the conversion and pressure drop arise in the transfer line between the furnace and the coking drums. In fact, most of the conversion and pressure drop takes place at the last third of the coil in the furnace. Clearly, efforts to reduce the

system pressure should be directed to these sections in particular by minimizing the length of the transfer lines and the number of pipe fittings, which depend on plant layout.

CONCLUSIONS

Good delayed coking furnace performance is generally seen as meeting the specified outlet temperatures for the lowest possible conversion since this would mean that the campaign time is maximized. However, the energy required for the endothermic chemical reactions and vaporization of products in the coke drums is supplied by the furnace. If the conversion upstream the drums is low, the temperature needs to be increased to ensure that a similar yield of liquids is obtained. In practice this increases the tendency of coking in the furnace tubes, since higher wall temperatures have to be expected. It can also result in shot coke formation (10).

The goal should not be to minimize conversion in the furnace but to reduce the pressure drop. This vaporizes products at the lowest possible temperature, transferring energy to the drums as latent rather than sensible heat. Tube coking is minimized by using high velocities while not reducing residence times, e.g., by using small diameters and longer coil lengths.

The scope for gaining maximum benefit using this approach is obviously increased if the process models can be further developed. This requires a good representation of the angular distribution of heat in the tubes.

REFERENCES

1. Bozzano G. Tesi di Dottorato in Ingegneria Chimica 1994, Politecnico di Milano.
2. Hughmark G. A. Chemical Engineering Progress 1962, 62.
3. Baker O. Oil & Gas Journal 1954, July 26, 185.
4. Soave G., Chemical Engineering Science 1972, 27, 1197.
5. Wright W. A. Journal of Materials 1969, 4, 1, 19.
6. Chen N. H. Ind. Eng. Chem. Fund. 1979, 18, 296.
7. Dukler A. E.; Wicks M.; Cleveland R. G. AIChE Journal 1964, 44.
8. Sugaya M. F.; Maciel R. Petrobras Internal Report 1994.
9. Griffith P.; Wallis G. B. Journal of Heat Transfer 1961, Aug., 307.
10. Ellis P. J.; Bacha J. D. Light Metals 1996, 477.
11. Dean D. E.; Stiel L.I. AIChE Journal 1965, 526.
12. Gunn R. D.; Yamada T. AIChE Journal 1971, 17, 1341.
13. Mallan G. M.; Michaelian M. S.; Lockhart F. J. J. Chem. Eng. Data 1972, 17, 412.
14. Stiel L. I., Thodos G., AIChE Journal 1964, Jan., 26.

Table 1 Geometric data for tubes in furnaces 52-F-1 A/B. Dead ends are 2 x 225 mm.

Section	Part	L_{eff} (m)	d_i (mm)	d_o (in)	Avg. pitch (mm)	Tubes (per pass)
Convection	1-4	10.364	74	89	189	38
Radiation	1	10.364	65	83	199	34

Table 2 Operating data for furnaces 52-F-1 (including a 10 % heavy gasoil recycle).

Furnace	Pass	Combined feed (m^3/d)	Water (m^3/d)
A	1	320	3.5
	2	316	3.5
	3	318	3.4
	4	313	3.4
B	1	315	3.5
	2	316	3.5
	3	315	3.5
	4	316	3.5
total		2530	27.8

Table 3 Transfer line geometry up to the switch valve.

Part	Type	d_{in} (in)	d_{out} (in)	Length (m)	Inclination (degrees)	Passes
1	nozzle	3	3	-	-	4
2	expansion	3	4	-	-	4
3	line	4	4	2.2	0	4
4	cross	4	4	-	-	4
5	line	4	4	1.2	0	4
6	expansion	4	6	-	-	4
7	cross	6	6	-	-	2
8	line	6	6	1.0	90	2
9	cross	6	6	-	-	2
10	line	6	6	2.0	0	2
11	expansion	6	8	-	-	2
12	cross	8	8	-	-	1
13	line	8	8	11.7	0	1
14	cross	8	8	-	-	1
15	line	8	8	7.7	90	1
16	cross	8	8	-		1
17	line	8	8	2.3	0	1

Table 4 Results of the model in comparison with industrial data. Pressures in bars, temperatures in C, duties in 10^6 kcal/h and fuel gas consumption in Nm^3/d.

	52-F-1 A	Model	52-F-1 B	Model
$T_{in,\ convection}$	238	238	238	238
$T_{out,\ convection}$	396	396	372	372
$Duty_{convection}$	n.a.	6.2	n.a.	5.2
$T_{out,\ radiation}$	502	502	502	503
$Duty_{radiation}$	n.a.	5.7	n.a.	6.5
$Duty_{furnace}$	11.1	11.9	11.5	11.7
Fuel gas	1380	1470	1420	1450
$T_{switch\ valve}$	n.a.	490	n.a.	490
$P_{in,\ furnace}$	16.2	16.2	19.9	19.9
$P_{in,\ convection}$	14.7	14.7	18.4	18.4
$P_{out,\ convection}$	n.a.	13.6	n.a.	16.8
$\Delta P_{,\ convection}$	n.a.	1.1	n.a.	1.6
$P_{in,\ radiation}$	n.a.	13.6	n.a.	16.8
$P_{out,\ radiation}$	n.a.	8.5	n.a.	10.1
$\Delta P_{radiation}$	n.a.	5.1	n.a.	6.7
$\Delta P_{furnace}$	n.a.	7.7	n.a.	9.8
$P_{switch\ valve}$	4.0	4.1	4.3	4.2
$\Delta P_{transfer\ line}$	n.a.	4.4	n.a.	5.9
$\Delta P_{furnace+tr.ln.}$	12.2	12.1	15.6	15.7

Table 5 Distribution of conversion and pressure drop in the system.

	52-F-1 A	52-F-1 B
conversion in furnace	83 %	81 %
conversion in transfer line	17 %	19 %
$\Delta P_{furnace}$	64 %	62 %
$\Delta P_{transfer\ line}$	36 %	38 %

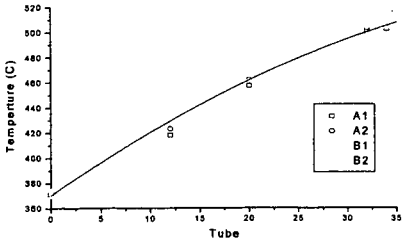

Figure 1 Fluid temperatures in the radiation zones A/B of F-1 A.

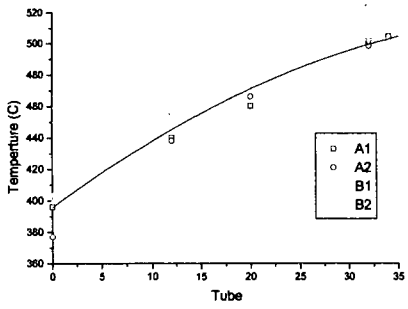

Figure 2 Fluid temperatures in the radiation zones A/B of F-1 B.

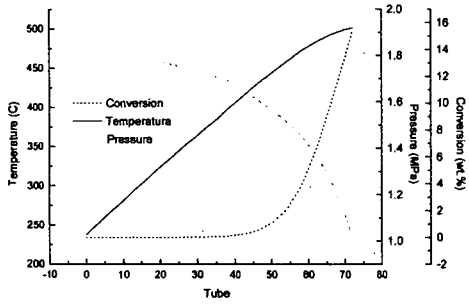

Figure 3 Conversion in F-1 A. The radiation section starts after tube 34.

HETEROGENEOUS MODELING OF AN ADIABATIC PACKED BED REACTOR WITH CATALYST DECAY. INTRAPARTICLE DIFFUSION EFFECTS

M. Chocrón[1,2], N. E. Amadeo[2], and M. A. Laborde[2]
1. Unidad de Actividad Química, Centro Atómico Constituyentes, Comisión Nacional de Energía Atómica. Av. del Libertador 8250 (1429),Buenos Aires, Argentina.
2. Depto. de Ingeniería Química, Facultad de Ingeniería, Universidad de Buenos Aires Pabellón de Industrias, (1428) Ciudad Universitaria, Buenos Aires, Argentina. e-mail: miguel@di.fcen.uba.edu.ar (Address to which correspondence should be submitted).

KEYWORDS : Fixed bed reactor, heterogeneous modeling, catalyst deactivation.

INTRODUCTION

Reactor models for catalytic reactions overlaid with transport restrictions and with catalyst deactivation are still not completely developed. The interrelation between internal diffusion and deactivation in a catalytic pellet was previously examined [1,2].
In the present work, an algorithm for simulation of an adiabatic fixed bed reactor subjected to catalyst deactivation by poisoning is developed applying the heterogeneous model. An irreversible first order reaction is considered for modeling purposes. The integral packed bed reactor is nodalized by N state equations corresponding to the N differential continuous stirred tank reactors into which the whole reactor is divided. For each differential reactor the energy and mass balances are solved and the concentration value at the center of the catalyst pellet is found using the shooting technique.

MATHEMATICAL MODEL

For an adiabatic fixed bed reactor and considering the one dimensional heterogeneous model nodalized as a series of differential CSTR's, the dimensionless mass balances for the main reactant and poison at the jth reactor are:

$$(C_{ij} - C_{oj}) = N_j \, av \frac{V_j}{Q} \tag{1}$$

$$(Cp_{ij} - Cp_{oj}) = Np_j \, av \frac{V_j}{Q} \tag{2}$$

and the dimensionless energy balance is:

$$T_{oj} = T_{ij} + \beta (C_{ij} - C_{oj}) \tag{3}$$

In equation (3) it was assumed that the only contribution to the temperature rise is given by the main reaction, since the poison is highly diluted in the feed.
On the other hand, for an isothermal, cylindrical catalyst pellet with constant properties and ignoring the external diffusional effects, the mass conservation equations for the reactant and poison are:

$$\frac{1}{r}\frac{d}{dr}\left(r\frac{d\xi}{dr}\right) = \phi^2 a_P(r,t) \exp\left[\gamma_1 \frac{(T-1)}{T}\right] \xi \tag{4}$$

$$\frac{1}{r}\frac{d}{dr}\left(r\frac{d\xi_P}{dr}\right) = \phi_P^2 a_P(r,t) \exp\left[\gamma_{P2} \frac{(T-1)}{T}\right] \xi_P \tag{5}$$

An irreversible first order reaction is assumed for the main reaction, like :

$$r_m = k_0 \exp\left[-\frac{\gamma_1}{T}\right] \xi \, a_P(r,t) = k \, \xi(r,t) \, a_p(r,t) \tag{6}$$

while a kinetic expression such as:

$$r_p = k_{20} \exp\left[-\frac{\gamma_{P2}}{T} \right] \xi_P \, a_P(r,t) = k_2 \, \xi_p(r,t) \, a_p(r,t) \qquad (7)$$

is considered for the poison.

The boundary conditions for equations (4) and (5) are:

$$\text{at } r=0 \;,\; d\xi / dr = 0 \qquad \text{and} \qquad d\xi p / dr = 0 \qquad (8)$$

at r=1 :

$$(C_{ij} - C_{oj}) = \frac{Deff \; av \; V_j}{Rp \; Q} \left(\frac{\partial \xi}{\partial \tau} \right) \qquad (9)$$

$$(Cp_{ij} - Cp_{oj}) = \frac{Dpeff \; av \; V_j}{Rp \; Q} \left(\frac{\partial \xi_P}{\partial \tau} \right) \qquad (10)$$

where:

$$N_j = \frac{Deff}{Rp} \left(\frac{\partial \xi}{\partial \tau} \right) \qquad (11)$$

$$Np_j = \frac{Dpeff}{Rp} \left(\frac{\partial \xi_P}{\partial \tau} \right) \qquad (12)$$

The deactivation rate into the pellet is given by:

$$\frac{da_P(r,t)}{dt} = -k_{10} \exp\left[-\frac{\gamma_{P1}}{T} \right] \xi_P \, a_P(r,t) = -k_1 \, \xi_P \, a_P(r,t) \qquad (13)$$

The system of equations (1)-(13) is solved assuming a quasi-steady state for the reactant and poison profiles into the pellet because the deactivation rate is relatively slow.
Beginning from t=0 and j=1 (the first CSTR), the reactant and poison profiles into the pellet are found using the shooting technique. The pellet is deactivated a given period of time and the procedure is repeated until the final operating time of the reactor is achieved. The same method is applied to the other differential reactors.

RESULTS

The plots shown in Figures 1 to 6 were obtained for the following reactor inlet conditions: T^0 = 503 K, C^0 = 8.5 mol / m^3, C^0_p = 8.3 10^{-9} mol / m^3. Feed rate, reactor volume and specific area of the bed are Q = 1.13 m^3 / sec, V = 14 m^3 and av = 950 m^2 / m^3 respectively. The reaction enthalpy is ΔH = -41190 J / mol. The specific heat and density of the feed mixture are, Cpg = 2576 J / Kg °C and ρ_g = 8.46 Kg / m^3.
The parameters of the pellet are: R_p = 0.0022 m ; Deff = 4.3 10^{-7} m^2 / sec; Dpeff = 6 10^{-6} m^2 / sec.

In figures 1 to 3 the evolution of the profiles of reactant, poison and activity into the pellet is presented for poison and reactant Thiele modulus values such that strong diffusional effects exist. It can be seen that, at t = 0 , the reactant and poison profiles are pronounced and became flatter along the time. Consequently, at short operating time the activity is almost nulle in the pellet surface and remain high toward the center.
The evolution of the poison and activity profiles along the fixed bed reactor is shown in figures 4 and 5. It is observed that, in agreement with the highly diffusional effects achieved into the pellet, the reactor is deactivated as a plug flow. This effect is frequently observed in industrial reactors; for instance in the case of CO converters [4].
Finally, reactant profiles along the reactor for two different poison Thiele modulus are presented in figure 6. It can be appreciated that as higher the poison Thiele modulus, higher is the fixed bed life.

CONCLUSIONS

The simulation of a fixed bed undergoing catalyst deactivation by poisoning was presented by means of the heterogeneous one-dimensional model. The parameter values of the model and the operating conditions were chosen such that relatively high diffusional effects appeared into the pellet for the poison as well as for the main reactant.
Activity and concentration profiles into the pellet and along the reactor and their evolution with the operating time are presented. The effect of the reaction rate of the poison is examined. It is proved that the performance of the reactor and the life of the catalyst improve when diffusional resistance for the poison increases.

ACKNOWLEDGMENTS

Support of this work provided by the Consejo Nacional de Investigaciones Científicas y Técnicas (CONICET) , Universidad de Buenos Aires and the Comisión Nacional de Energía Atómica (C.N.E.A.) is gratefully acknowleged.

NOTATION

a_P : activity by poison.
av : specific area of the catalytic bed
C : dimensionless reactant concentration (bed)
C_P : dimensionless poison concentration (bed)
Cpg : specific heat of the mixture
Deff : effective diffusion of the reactant.
Dpeff : effective diffusion of the poison
k : kinetic coeff. of the main reaction
k_1 : kinetic coeff. of the deactivation rate
k_2 : kinetic coeff. of the poison reaction
N : reactive flux toward the pellet
Np : poison flux toward the pellet
Q : volumetric flow rate
r_m : main reaction velocity
r : dimensionless radial position into the pellet
r_P : poison reaction velocity
R_p : Pellet radius
T : dimensionless temperature
t : time
V : reactor volume
z : dimensionless axial position

Greek Symbols

$\phi_P^2 : R^2 r_P^S / Dpeff \xi_P^S$
$\phi^2 : R^2 r_m^S / Deff \xi^S$
γ_{P1} : dimensionless activation energy, eq.(13)
γ_1 : dimensionless activation energy, eq. (6)
γ_{P2} : dimensionless activation energy, eq. (7)
ξ : dimensionless reactant concentration into the pellet
ξ_P : dimensionless poison concentration into the pellet
ΔH : enthalpy of reaction
ρ_g : feed density
$\beta : (-\Delta H) C^0 / \rho_g Cpg T^0$

Superscripts

S : pellet surface value
0 : conditions at the bed entrance

Subscripts

i : differential reactor inlet value
j : differential reactor number
o : differential reactor outlet value

REFERENCES

[1] M. Chocrón, Ma. del C. Raffo Calderón, N. Amadeo, M. Laborde. "Effect of intraparticle diffusion on catalyst decay". Chem. Eng. Sci., **51**, (1996),pp. 683.

[2] M. Chocrón, N. Amadeo, M. Laborde. "Catalyst decay by simultaneous sintering and poisoning. Effect of intraparticle and interfacial gradients". Catalyst Deactivation 1997. Studies in Surface Science and Catalysis, Vol. 111, pp. 311. Elsevier.

[3] Froment G., Bishoff K., "Chemical Reactor Analysis and Design", J. Wiley & Sons, 1979.

[4] González Velasco J., Gutiérrez Ortiz M., González Marcos J., Amadeo N., Laborde M.A., Paz M., "Optimal inlet temperature trajectories for adiabatic packed beds reactors with catalyst decay". Chem. Eng. Sci., **47**,(1992).pp.1945.

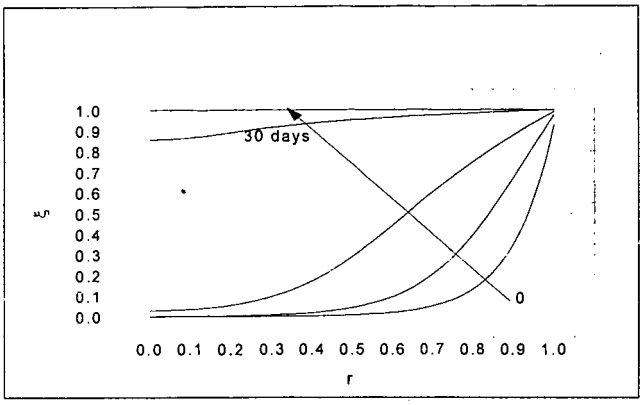

Figure 1 : Main reactant profile into the catalyst. First CSTR, $\phi = 10$, $\phi_P = 6$, $k_1 = 0.2$ 1 / h

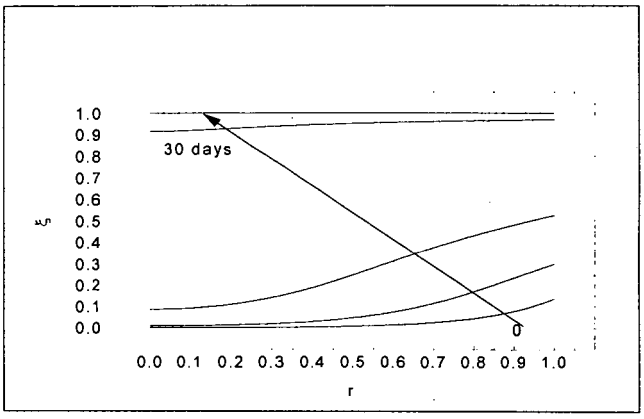

Figure 2: Poison profile into the catalyst. First CSTR, $\phi = 10$, $\phi_P = 6$, $k_1 = 0.2$ 1 / h

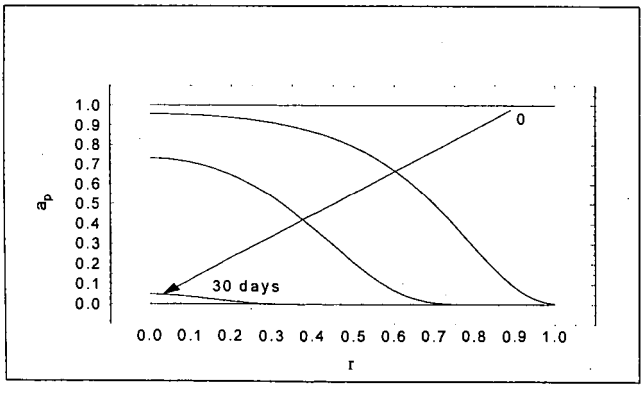

Figure 3 : Activity by poison into the catalyst. First CSRT, $\phi = 10$, $\phi_P = 6$, $k_1 = 0.2$ 1 / h

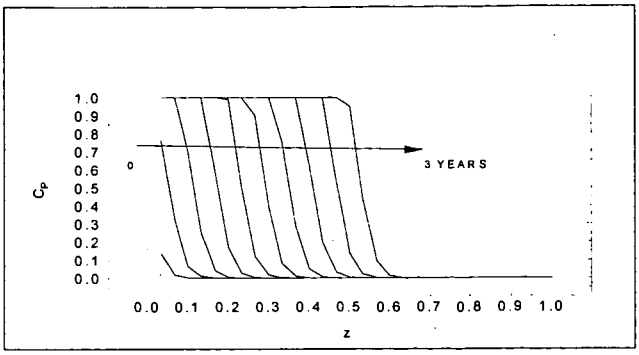

Figure 4: Dimensionless poison concentration vs. axial position. $\phi_P = 6$, $k_1 = 0.2$ 1 / h

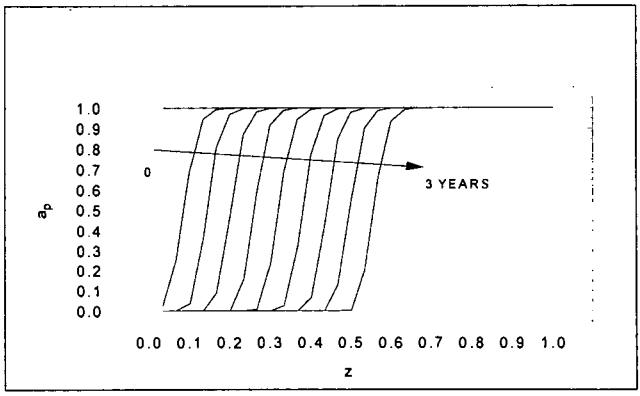

Figure 5: Activity by poison vs. axial position. $\phi_P = 6$, $k_1 = 0.2$ 1 / h

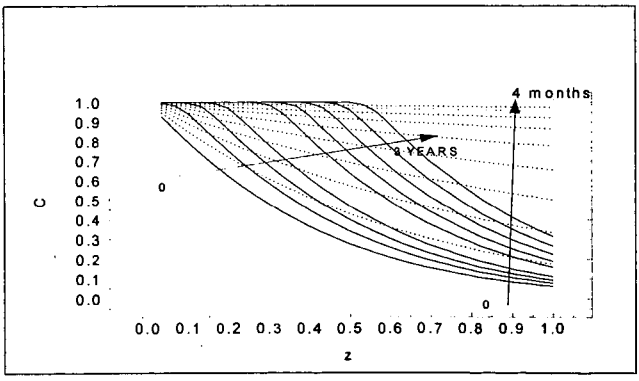

Figure 6: Main reactant profile vs. axial position. Solid line: $\phi = 10$, $\phi_P = 6$; Dots line: $\phi = 10$, $\phi_P = 3\ 10^{-2}$.